Taming Crystallization with Light

Korede, V.B.

DOI
10.4233/uuid:7c197383-2adc-49d6-9b28-cfd93114142b

Publication date
2024

Document Version
Final published version

Citation (APA)
Korede, V. B. (2024). *Taming Crystallization with Light*. [Dissertation (TU Delft), Delft University of Technology]. https://doi.org/10.4233/uuid:7c197383-2adc-49d6-9b28-cfd93114142b

TAMING CRYSTALLIZATION WITH LIGHT

TAMING CRYSTALLIZATION WITH LIGHT

Proefschrift

ter verkrijging van de graad van doctor
aan de Technische Universiteit Delft,
op gezag van de Rector Magnificus prof. dr. ir. T.H.J.J. van der Hagen,
voorzitter van het College voor Promoties,
in het openbaar te verdedigen op maandag 7 Oktober 2024 om 12:30 uur

door

Vikram Bharadwaj KOREDE

Master of Science in Chemical Engineering,
Technische Universiteit Delft, Nederland,
geboren te Hyderabad, India.

Dit proefschrift is goedgekeurd door de

Samenstelling promotiecommissie:

Rector Magnificus,	voorzitter
Dr. H.B. Eral,	Delft University of Technology, promotor
Prof. dr. J.T. Padding,	Delft University of Technology, promotor
Onafhankelijke leden:	
Dr. A. Spasojevic-de Biré	CentraleSupélec
Prof. dr. ir. J. van der Gucht	Wageningen University & Research
Dr. T. van Gerven	Katholieke Universiteit Leuven
Prof. dr. K. Hooman	Delft University of Technology
Dr. ir. V. van Steijn	Delft University of Technology
Prof. dr. ir. W. de Jong	Delft University of Technology, reservelid

This work was funded by LightX project under NWO Open Technology Programme (project number 16714).

Keywords: Crystallization, NPLIN, Laser, Irradiation, Supersaturation

Printed by: Proefschriftspecialist

Front & Back: Cover art by Art2learn.

ISBN 978-94-6366-924-5

An electronic version of this dissertation is available at
http://repository.tudelft.nl/.

CONTENTS

LIST OF FIGURES

LIST OF TABLES

SUMMARY

Crystallization is one of the most widely used purification and separation processes applied in a multitude of industries such as pharmaceuticals, food & beverages, agriculture, and fine chemicals. However, the initial step of the crystallization process, nucleation, is still poorly understood and highly stochastic. As a result, most crystallization processes lack proper control over the properties of the crystals produced. Among many techniques for achieving better control over the nucleation process, the application of non-photochemical laser induced nucleation (NPLIN) has gathered significant interest. This is because of its potential to improve product quality in crystallization processes by directly controlling the nucleation rate, both spatially and temporally. Additionally, NPLIN can induce crystallization in solutions that would otherwise take a long time to nucleate, offering a unique advantage over traditional methods. However, despite its promising capabilities, NPLIN is not widely used in practice yet. The fundamental mechanism behind NPLIN is not fully understood, making it unclear how it should be applied effectively in practice and for which systems NPLIN could be beneficial.

This Ph.D. project aims to delve into the fundamental mechanisms of NPLIN, by examining how specific laser and solution parameters influence nucleation kinetics, leveraging innovative experimental setups. Laser parameters being studied include laser-exposed volume, laser irradiation position, laser intensity and laser wavelength, and solution parameters include supersaturation levels, solution filtration, and the presence of impurities or dopants, particularly nanoparticles.

The thesis begins with a comprehensive review of the experimental and computational literature on NPLIN. It then presents a detailed study on the effect of the laser-exposed volume and laser irradiation position on the nucleation probability within partly illuminated supersaturated aqueous potassium chloride solutions. An increase in the laser-exposed volume resulted in a higher nucleation probability and a higher number of crystals per nucleated sample. Furthermore, laser irradiation, particularly through the air/solution interface, not only enhances nucleation probability but also influences the formation of different crystal morphologies. These observations are partly explained by the Nanoparticle Heating mechanism and the Dielectric Polarization model (Chapter 2).

The research then transitions to a microfluidic platform, which allows for high-throughput and crystallization detection using the deep learning method. This innovative approach addresses the need for large data sets in NPLIN research, which has been a significant challenge due to

the manual nature of traditional experiments. The study examines the effects of laser intensity, wavelength, supersaturation, solution filtration, and intentional doping on nucleation probability in supersaturated potassium chloride solutions. Higher laser intensities and increased supersaturation significantly enhance nucleation probabilities. The laser wavelength effect was only observed for 355 nm at higher laser intensities. Solution filtration suppresses the NPLIN effect, whereas the addition of nanoparticles as dopants into the solution not only increases the NPLIN probabilities but also affects the crystal morphology. The results highlight the importance of impurities in the solution and support the hypothesis that nanoparticle or impurity heating could be the key mechanism in understanding NPLIN (Chapter 3).

The study finally investigated the effects of solution filtration, laser intensity, and nanoparticle properties including nanoparticle concentration and material on NPLIN probability in supersaturated aqueous urea solutions. The study highlights the significant role of impurities in NPLIN, demonstrating that doping with different nanoparticle materials leads to varied nucleation probabilities. In particular, gold nanoparticles were found to enhance nucleation more effectively than silica nanoparticles. Additionally, it was observed that NPLIN probabilities followed a poisson distribution to changes in nanoparticle concentration and laser intensity respectively. The findings in this chapter enhance our understanding of the critical role of impurities in comprehending the NPLIN mechanism (Chapter 4).

SAMENVATTING

Kristallisatie is een van de meest gebruikte zuiverings- en scheidingsprocessen die wordt toegepast in een groot aantal industrieën, zoals de farmaceutische industrie, voedingsmiddelen, dranken, landbouw en fijnchemicaliën. De eerste stap van het kristallisatieproces, kiemvorming, is echter nog steeds slecht begrepen en zeer stochastisch. Als gevolg hiervan missen de meeste kristallisatieprocessen een goede controle over de eigenschappen van de geproduceerde kristallen. Van de vele technieken om een betere controle over het kiemvormingsproces te bereiken, heeft de toepassing van niet-fotochemische lasergeïnduceerde kiemvorming (NPLIN) aanzienlijke belangstelling gekregen. Dit komt door het potentieel om de productkwaliteit in kristallisatieprocessen te verbeteren door de kiemvormingssnelheid rechtstreeks te controleren, zowel ruimtelijk als tijdelijk. Bovendien kan NPLIN kristallisatie induceren in oplossingen waarvan het anders lang zou duren om te kiemen, wat een uniek voordeel biedt ten opzichte van traditionele methoden. Ondanks de veelbelovende mogelijkheden wordt NPLIN in de praktijk echter nog niet veel gebruikt. Het fundamentele mechanisme achter NPLIN wordt niet volledig begrepen, waardoor het onduidelijk is hoe het in de praktijk effectief moet worden toegepast en voor welke systemen NPLIN nuttig zou kunnen zijn.

Deze Ph.D. Het project heeft tot doel zich te verdiepen in de fundamentele mechanismen van NPLIN, door te onderzoeken hoe specifieke laser- en oplossingsparameters de nucleatiekinetiek beïnvloeden, waarbij gebruik wordt gemaakt van innovatieve experimentele opstellingen. Laserparameters die worden bestudeerd omvatten aan de laser blootgesteld volume, laserbestralingspositie, laserintensiteit en lasergolflengte, en oplossingsparameters omvatten oververzadigingsniveaus, oplossingsfiltratie en de aanwezigheid van onzuiverheden of doteermiddelen, met name nanodeeltjes.

Het proefschrift begint met een uitgebreid overzicht van de experimentele en computationele literatuur over NPLIN. Vervolgens presenteert het een gedetailleerd onderzoek naar het effect van het aan de laser blootgestelde volume en de laserbestralingspositie op de kans op kiemvorming in gedeeltelijk verlichte oververzadigde waterige kaliumchlorideoplossingen. Een toename van het aan de laser blootgestelde volume resulteerde in een hogere kiemvormingswaarschijnlijkheid en een groter aantal kristallen per kernhoudend monster. Bovendien vergroot laserbestraling, vooral via het grensvlak lucht/oplossing, niet alleen de waarschijnlijkheid van kiemvorming, maar beïnvloedt ook de vorming

van verschillende kristalmorfologieën. Deze waarnemingen worden gedeeltelijk verklaard door het nanodeeltjesverwarmingsmechanisme en het diëlektrische polarisatiemodel (hoofdstuk 2).

Het onderzoek gaat vervolgens over naar een microfluïdisch platform, dat high-throughput- en kristallisatiedetectie mogelijk maakt met behulp van de deep learning-methode. Deze innovatieve aanpak komt tegemoet aan de behoefte aan grote datasets in NPLIN-onderzoek, wat een aanzienlijke uitdaging is geweest vanwege het handmatige karakter van traditionele experimenten. De studie onderzoekt de effecten van laserintensiteit, golflengte, oververzadiging, oplossingsfiltratie en opzettelijke doping op de kans op kiemvorming in oververzadigde kaliumchlorideoplossingen. Hogere laserintensiteiten en verhoogde oververzadiging vergroten de kans op kiemvorming aanzienlijk. Het lasergolflengte-effect werd alleen waargenomen voor 355 nm bij hogere laserintensiteiten. Oplossingsfiltratie onderdrukt het NPLIN-effect, terwijl de toevoeging van nanodeeltjes als doteermiddelen aan de oplossing niet alleen de NPLIN-kansen vergroot, maar ook de kristalmorfologie beïnvloedt. De resultaten benadrukken het belang van onzuiverheden in de oplossing en ondersteunen de hypothese dat het verwarmen van nanodeeltjes of onzuiverheden het sleutelmechanisme zou kunnen zijn bij het begrijpen van NPLIN (Hoofdstuk 3).

De studie onderzocht uiteindelijk de effecten van oplossingsfiltratie, laserintensiteit en eigenschappen van nanodeeltjes, waaronder de concentratie en het materiaal van nanodeeltjes, op de NPLIN-waarschijnlijkheid in oververzadigde waterige ureumoplossingen. De studie benadrukt de belangrijke rol van onzuiverheden in NPLIN, wat aantoont dat doping met verschillende nanodeeltjesmaterialen tot uiteenlopende kiemvormingskansen leidt. In het bijzonder bleken gouden nanodeeltjes de kiemvorming effectiever te bevorderen dan nanodeeltjes van silica. Bovendien werd waargenomen dat de NPLIN-kansen een poissonverdeling volgden op veranderingen in respectievelijk de concentratie van nanodeeltjes en de laserintensiteit. De bevindingen in dit hoofdstuk vergroten ons begrip van de cruciale rol van onzuiverheden bij het begrijpen van het NPLIN-mechanisme (hoofdstuk 4).

1

INTRODUCTION

Crystallization - how loosely correlated atoms in a solvent arrange themselves to flawless ordered structures - has long captivated scientists and engineers alike. It is ubiquitous in nature and industrial practice, from the production of nanostructured materials, catalysts, organic electronics, pharmaceuticals, to the formation of teeth and bones [1–4]. Given its ability to separate a compound from a mixture in a single step while achieving high purity, crystallization is a preferred method in various industries.

Crystallization consists of two primary phenomena: nucleation and growth and a number of secondary phenomena including secondary nucleation, agglomeration and attrition.

1.1. NUCLEATION

Nucleation, also referred to as primary nucleation is the emergence of an ordered solid structure of solute molecules in the solution[5]. This phenomenon, termed primary nucleation, occurs without the influence of pre-existing material. In contrast, secondary nucleation relies on the presence of existing crystals to initiate further crystal formation. Primary nucleation can be further classified into two distinct categories: homogeneous and heterogeneous. Homogeneous nucleation refers to the spontaneous formation of a crystal nucleus within the bulk of the solution, entirely independent of external stimuli. Meanwhile, heterogeneous nucleation occurs in in the vicinity of foreign particles such as walls of the container, agitator, dust, and impurities, which act as catalysts for crystal formation [6]. The elimination of such interfaces is practically unfeasible, thus achieving purely homogeneous nuclei is only possible at high levels of supersaturation[5].

A part of this chapter is based on Vikram Korede, Nagaraj Nagalingam, Frederico Marques Penha, Johan Padding, Remco Hartkamp and Hüseyin Burak Eral, Crystal Growth & Design 2023 23(5), 3873–3916

The driving force for nucleation is the supersaturation ratio of the solution and is derived fundamentally from the difference in chemical potential between the solution and the crystalline phase, state 1 and state 2, respectively [6].

$$\Delta\mu = \mu_2 - \mu_1 \tag{1.1}$$

The chemical potential, μ, is a function of temperature, T, and depends on the standard potential, μ_0, the activity, a, and the Boltzmann constant, k_B:

$$\mu = \mu_0 + k_B T \ln a \tag{1.2}$$

and hence, the driving force of crystallization in dimensionless form can be written as

$$\frac{\Delta\mu}{k_B T} = \ln \frac{a}{a^*} = \ln S \tag{1.3}$$

where a^* is the activity of a saturated solution and S is the supersaturation ratio [6]. Assuming an ideal solution, supersaturation can be directly defined in terms of solute concentration as

$$S(T) = \frac{c}{c_s(T)} \tag{1.4}$$

Here, c denotes the solute concentration, and $c_s(T)$ signifies the saturation concentration at a given temperature, both measured in g solute/g solvent, respectively.

To rationalize the primary nucleation process, two models are proposed. Classical nucleation theory (CNT) and two-step nucleation theory (TSN) [3, 7]

Classical nucleation theory, widely used due to its analytical simplicity, explains nucleation as a balance between the tendency to form a new phase and the energy cost associated with forming a new surface. In more formal terms, it describes nucleation as a one-step stochastic process dictated by the Gibbs free energy change for the phase transformation and the free energy change for the formation of a surface. Since the free energy change of surface formation and the free energy change of phase transformation depend differently on the cluster radius, the total free energy change of cluster formation passes through a maximum [6]. Nucleation occurs when the pre-nucleated cluster grows to a critical radius, and surpasses the critical free energy change of cluster formation, known as the nucleation barrier. The nucleation rate, a measure of the quantity of stable nuclei generated per unit volume and unit time, is typically represented by the Arrhenius reaction rate given by equation 1.5, incorporating pre-exponential factor and activation energy term.

$$J = A \exp\left(-\frac{16\pi\gamma v^3}{3k_B T \ln(S)}\right) \tag{1.5}$$

Here, J represents the nucleation rate as a function of supersaturation (S), interfacial tension (γ), molecular volume (v), Boltzmann's constant (k_B), Temperature (T), and the pre-exponential factor (A).

The pre-exponential term (A) represents the frequency at which nuclei form without energy barriers. It accounts for both the frequency of molecular collisions that lead to the formation of stable nuclei and the availability of suitable sites for nucleation. The exponential term represents the probability of overcoming the energy barrier for nucleation at a given temperature. This emphasizes the probabilistic nature of nucleation, illustrating that not all collisions result in successful nucleation due to energy considerations. Additionally, the nucleation rate in Equation 1.5 depends on the operating conditions such as the temperature, supersaturation and therefore in order to control nucleation, a precise control over the operating conditions is necessary.

Recently, there has been a shift in the prevailing perspective towards classical nucleation theory (CNT) as the most acceptable mechanism for nucleation. Shortcomings of CNT in explaining observations, particularly in protein crystallization experiments, led to the proposal of the two-step nucleation model (TSN). TSN assumes that the clusters of solute molecules have to overcome two barriers one associated with the density increase of solute molecules between solution and solid phases, and another arising from the formation of an ordered crystalline structure necessary for stable nucleus formation[8–11]. The nucleation rate becomes dependent on the rate-limiting step under such a multi-step mechanism. Despite these proposed mechanisms, further development is needed, and a gap remains in the fundamental understanding of nucleation.

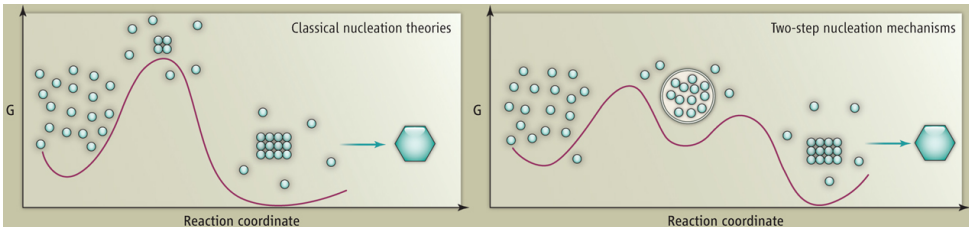

Figure 1.1.: Free energy diagrams of the proposed pathways for the Classical Nucleation Theory (left) and Two-step nucleation theory (right) [12].

1.1.1. CRYSTAL GROWTH, ATTRITION AND AGGLOMERATION

Thus, crystal growth fundamentally involves the incorporation of solute molecules from the supersaturated solution into the crystal lattice. The growth of a crystal is often described by the linear growth rate, which is defined as a change in length of a certain dimension over time. Various theories have been proposed to elucidate the process of crystal growth. It is important to control the supersaturation in the suspension because high levels of supersaturation can result in rough crystals with surface imperfections and impurity inclusion in the crystal lattice[6, 13, 14]. In addition, due to the turbulent conditions in a crystallization process, crystals collide with each other, with the walls of the crystallizer, and with the impeller. These collisions will cause attrition, where the breakage of the crystals into smaller crystals gives rise to new nuclei. The new nuclei can potentially serve as nucleation sites, and will compete for the available supersaturation to grow into larger crystals[6]. Agglomeration on the other hand, occurs when multiple crystals stick together and form a single, larger crystal. Agglomeration is generally undesirable, as it can detrimentally alter the properties of the crystal product and often contain impurities due to enclosed mother liquor. [6].

In industrial practice, nucleation and growth often occur in turbulent conditions in well-stirred vessels. These two fundamental phenomena are always followed by secondary crystallization phenomena such as attrition, aggregation, and secondary nucleation - unless the process is specially designed to suppress these secondary phenomena[15]. Nucleation, growth, and these secondary physical phenomena collectively dictate the crystal quality parameters: crystal size distribution, purity, polymorphism and morphology, also referred to as the four pillars of industrial crystallization [1, 2, 15–17]. Controlling these physical properties is crucial, as characteristics such as solubility and flowability depend on the attributes of the crystal products. Inadequate control over crystal size and shape not only compromises the quality but also impacts downstream processes such as filtration and drying, potentially leading to significant product loss[18].

1.1.2. NUCLEATION CONTROL : CHALLENGES & ADVANCEMENTS

Primary nucleation is the critical step to control in the crystallization process for the formation of a crystalline product with desired properties. It is important to control both the rate of nucleation and the type of polymorph, as both are strongly dependent on the level of supersaturation. This control is crucial to avoid an excessive number of nuclei, as it can lead to broad, undesired size distributions, impurity inclusions, growth artifacts, or even undesired form of the crystals[1, 6]. However, the process of nucleation is strongly stochastic i.e. it is very hard to predict when and where the nucleation will happen

inside the solution volume during the crystallization process. Accurately determining the nucleation rate poses a challenge. This often relies on detectable crystals under the assumption that all initiated nuclei will eventually grow into larger crystals. Furthermore, classical nucleation theory predicts a homogeneous nucleation rate; however, real-world observations typically reveal a heterogeneous nucleation rate influenced by the presence of surfaces and impurities[6].

The inaccessibility of the nucleation time and spatial scales and the steep dependence of the nucleation rate on supersaturation have made the control of primary nucleation difficult. Although significant advances in understanding the mechanism of nucleation from solution have been made[11, 19–22], many aspects of the nucleation process, such as the mechanism of polymorph selection and on-demand spatial-temporal control, are far from being completely understood. This makes the deterministic design and scale up of industrial crystallization processes challenging. To improve and optimize the industrial crystallization process, a better understanding of the crystallization process on both a fundamental and molecular level is necessary. Such an understanding would enable control over the crystal product properties.

A variety of tools and techniques, including molecular simulations, high-throughput microdevices, spectroscopic methods, aid in understanding and characterizing nucleation processes. Molecular simulations such as Molecular Dynamics (MD) and Monte Carlo (MC) simulations offer atomic or molecular level insights, predicting nucleation rates and elucidating factors influencing nucleation[23]. High-throughput microdevices, particularly microfluidic platforms, facilitate the rapid screening of nucleation conditions across thousands of micro-environments to optimize crystallization parameters[24–26]. Spectroscopic techniques like Raman spectroscopy, FTIR, and NMR provide real-time molecular structure and composition monitoring, crucial for observing the early stages of nucleation[27, 28]. These approaches provide valuable insights into the nucleation mechanisms and contribute to the development of strategies for enhancing nucleation control in crystallization processes.

Research on nucleation control aims to improve the prediction and manipulation of nucleation rates. Seeding, in particular, has obtained significant attention as a promising alternative method for primary nucleation. This technique involves introducing pre-existing crystals into a supersaturated solution, serving as nucleation sites to initiate crystal growth. Addition of seed crystals under the proper conditions can result in desired crystal forms with enhanced uniformity and purity[29–32]. Although seeding is used to avoid primary nucleation completely, it is not without its drawbacks. For seeding to be effective, the seed crystal must have a purity and structure that matches the desired end product. Finding or producing such a seed can be difficult, particularly for complex or new compounds. Moreover, any impurities present in the

seed can lead to defective growth or unwanted inclusions in the final crystal. Additionally, the timing of seed addition is critical and must be carefully controlled to coincide with optimal supersaturation levels in the crystallizer, avoiding excessive secondary nucleation and promoting desired crystal growth[30].

Innovative methods like attrition based nucleation control, sono-crystallization, laser induced nucleation are being explored to enhance primary nucleation control. Attrition based nucleation control involves the deliberate agitation or abrasion of materials to initiate nucleation. By subjecting the solution to controlled mechanical forces, such as stirring or milling, nucleation can be triggered at specific sites. The effectiveness of attrition-based nucleation control lies in its ability to create localized regions of high supersaturation or to directly generate physical imperfections that serve as nucleation sites. For example, during high-energy ball milling, particles are fractured and broken down, creating new surfaces and defects that can act as favorable sites for nucleation. Similarly, vigorous stirring can introduce shear forces that disrupt the solution's equilibrium, leading to enhanced supersaturation and the formation of micro environments conducive to nucleation[1, 6].

Sono-crystallization utilizes ultrasound waves to induce nucleation events within the solution. The application of ultrasound energy generates localized cavitation, where alternating compression and rarefaction of sound waves lead to the formation and collapse of bubbles. Although the exact mechanism remains unclear, these cavitation bubbles act as nucleation sites, facilitating the formation of nuclei and influencing subsequent crystal growth. This process not only initiates nucleation but also aids in creating new particles by disrupting existing crystals through a process known as sonofragmentation[33–35]. However, it is important to acknowledge that both attrition-based nucleation control and sono-crystallization share a significant drawback: the processes can lead to the breakage and disruption of larger crystals, which can detrimentally affect the overall crystal quality[1, 33–35].

In contrast, laser-induced nucleation presents an intriguing method for controlling nucleation under low supersaturation conditions with precise spatial and temporal control. Significantly reducing nucleation induction times in slightly supersaturated solutions, laser-induced nucleation offers the advantage of being a non-contact method, minimizing the risk of contamination from equipment surfaces. Moreover, by understanding and controlling nucleation both temporally and spatially, industrial crystallization can be revolutionized, by moving from equipment-based methods to those based on predictive physicochemical design. However, at this stage, the mechanism behind laser-induced nucleation is not fully understood[36], thereby presenting an opportunity for research that could redefine our approach to crystallization processes.

Moving forward, this chapter delves into a more detailed discussion of

laser-induced nucleation.

1.1.3. LASER INDUCED CRYSTALLIZATION

The light-material interaction experiments which we collectively refer to as laser-induced crystallization (LIC) have often, but not always, been conducted by exposing a solution carrying a solute dissolved in a solvent to a light source of a given wavelength, intensity, exposure time, and pulse width. The exact experimental details including experimental geometry (e.g., container geometry, how the beam interacts with confining surfaces and solution), laser characteristics (intensity, wavelength, polarization, continuous or pulsed laser, pulse width), exposure time (ranging between femtoseconds to hours) and solution characteristics vary considerably across the literature. Moreover, distinct mechanisms based on molecular effects as well as continuum approaches have been proposed depending on these experimental details.

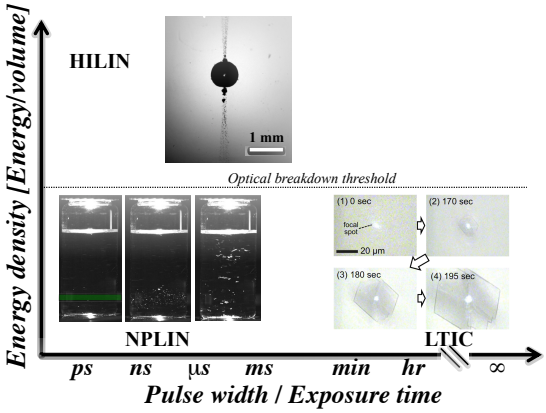

Figure 1.2.: Laser induced crystallization phenomena. Classification of non-photochemical laser-induced nucleation (NPLIN), high-intensity laser-induced nucleation (HILIN), and laser-trapping-induced crystallization with optical tweezers (LTIC) based on energy density and laser pulse width or exposure time in case of continuous lasers used in LTIC.

In the literature, three different methods leveraging light-material interactions for LIC have evolved as semi-independent research fields. These methods are namely non-photochemical laser-induced nucleation (NPLIN), high-intensity laser-induced nucleation (HILIN), and laser-trapping-induced crystallization with optical tweezers (LTIC-OT), each varying in energy density and pulse width. Figure 1.2 illustrates efforts to classify existing LIC literature based on the energy of the light

irradiation and pulse width or exposure time when continuous lasers are concerned.

In this thesis, we will limit our classification to methods that are non-photochemical in nature. The term 'non-photochemical' implies that the laser beam does not induce any photochemical reaction[37] and the solution does not absorb light at the irradiated wavelength. NPLIN involves the use of a nanosecond laser pulse to induce immediate crystallization in supersaturated solutions. Ordinarily, these solutions would take several weeks to nucleate without any external intervention [38].

Non-photochemical Laser Induced Nucleation (NPLIN) represents a paradigm shift in our approach to crystallization. Unlike traditional mechanisms that rely on supersaturation, NPLIN acts directly on the nucleation energy landscape at the molecular level, offering a new avenue for precise nucleation control. This process has shown promise in a wide range of compounds, from simple salts to small proteins, suggesting a broad applicability [25, 39–43].

1.2. NON-PHOTOCHEMICAL LASER-INDUCED NUCLEATION (NPLIN)

1.2.1. PHENOMENOLOGY

In 1996, while attempting to observe second-harmonic generation in supersaturated aqueous urea solutions, Garetz *et al.*[39] noticed unexpected instantaneous crystallization upon light irradiation in solutions that would otherwise take several weeks to crystallize spontaneously. In this study, Garetz and co-workers exposed milliliter size vials as shown in Figure 1.3, using a series of linearly polarized, unfocused (50-250 $MW\,cm^{-2}$), nanosecond light pulses with 1064 nm wavelength.

Garetz *et al.*[39] referred to this observed light-induced phenomenon as non-photochemical laser-induced nucleation, NPLIN. This phenomenon was considered as non-photochemical since: (i) neither the solute nor the solvent has strong absorption bands at irradiated wavelengths and (ii) the applied laser intensity ($\sim MW\,cm^{-2}$) is considered too low to trigger photochemical reactions through non-linear optical effects. They reported the formation of needle-like urea crystals aligned with the polarization plane of the laser, suggesting an electric-field-induced origin of the underlying mechanism. Over the following decades, various groups have reported enhanced nucleation probabilities upon laser irradiation, quantified by counting the fraction of vials nucleated after a given time, compared to spontaneous nucleation in a broad range of solute/solvent systems with comparable experimental parameters reported by Garetz *et al.*[39] (one or more unfocused laser pulses of ∼ns

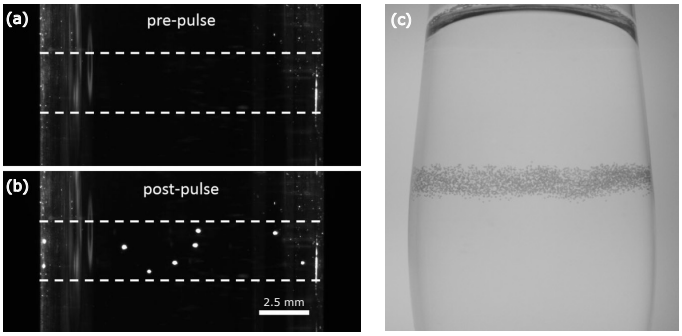

Figure 1.3.: NPLIN in action (a,b) Solution of NH_4Cl before and approximately 1.6 s after irradiating by a single laser pulse[44]. The path of the laser beam through the solution is indicated by the dashed white lines, with the start of nucleation visible as white dots between the lines. (c) Nucleation of carbon dioxide bubbles within carbonated solution caused by the passage of the laser pulse from left to right[45].

duration and 532 nm/1064 nm wavelength). Moreover, NPLIN has also been reported to offer control over the polymorphic form nucleating from solution[46, 47]. Thus, the observations of locally enhanced nucleation probability at the laser irradiation position, and the potential to control the polymorphic form, point out that NPLIN may be a promising primary nucleation control method (Figure 1.3). A solid understanding of the underlying NPLIN mechanism-a discussion that has yet to be settled in the literature-has the key to fulfilling its potential as a broadly applied nucleation control method. In this section, common observations in NPLIN experiments reported in the literature will be summarized, along with the proposed mechanisms, Particularly, a critical discussion on to what extent the proposed mechanisms hold to explain the observations. Finally, future directions will be highlighted in the summary section.

The experimental observations and observed trends in NPLIN experiments may shed light on the underlying mechanism. To this end, we present an extensive list of observations compiled from the literature.

1. A broad range of compounds under NPLIN: NPLIN has been reported for a range of systems (predominantly in aqueous media), including small organics [47–49], metal halides[50], single component systems [51, 52], dissolved gases[45, 53] and a macromolecule - lysozyme[54].

2. Not all solutions undergo NPLIN: Ward *et al.*[44] reported that acetamide (CH_3CONH_2), an organic molecule with relatively high solubility and molecular structure similar to urea (CH_4N_2O), does not exhibit NPLIN. In the unpublished work of Barber[55], aqueous sodium chlorate was also reported to not undergo NPLIN.

3. The NPLIN probability depends on laser peak intensity and supersaturation: the fraction of samples nucleated under NPLIN was reported to increase with both laser peak intensity and solution supersaturation[39, 56].

4. Laser pulse duration matters: For similar peak intensities (j_{peak} $\approx$ 30 MWcm^{-2} per pulse), aqueous solutions of CO_2, KCl, NH_4Cl and CH_4N_2O exposed to unfocused femtosecond-laser pulses ($\approx$ 110 fs) did not nucleate while exposure to nanosecond ($\approx$ 5 ns) pulses triggered nucleation[44]. Although both femtosecond and nanosecond pulses had the same peak intensity, the total energy per pulse (Jcm^{-2}) is 5 orders of magnitude higher with the nanosecond pulse due to its longer pulse duration. Yet beyond nanoseconds, further increase in pulse width (6 ns to 200 ns) was reported to not alter the crystallization probability[57].

5. Laser wavelength dependence: Kacker *et al.* [56] reported that nucleation probability of supersaturated aqueous KCl exposed to a single pulse of 355, 532 and 1064 nm is not strongly dependent on the laser wavelengths. Yet, shorter wavelengths, namely 355/532 nm, led to slightly higher nucleation probability for KCl[50, 56], KBr[50] and urea[48].

6. Dependence of the number of crystals/bubbles on laser peak intensity: with an increase in the laser peak intensity, a linear increase in the number of crystals for KCl[58, 59] and glycine[60], and a quadratic increase in the number of CO_2 bubbles[45] was observed.

7. Polarization switching: Laser polarization is reported to influence the polymorphic form of several simple organic molecules such as glycine[49], L-histidine[47], carbamazepine[61] and sulfathiazole[62]. However, this observation could not be reproduced for glycine by Liu *et al.*[63], nor later by Irimia *et al.*[64], indicating a subtle effect in the experimental conditions is at play.

8. Laser intensity threshold: Several authors report a threshold laser intensity below which laser irradiation does not trigger nucleation[39, 48, 63]. Moreover, this laser intensity threshold is observed to be dependent on the solute, the wavelength of the laser light, and the temperature[48, 50]. Between solutes, small organics[48, 49] such as urea and glycine are observed to have a higher laser peak-intensity threshold (>50 MW cm^{-2}) compared to metal halides[50] (>3 MW cm^{-2}) such as KCl and KBr.

9. Dependence on solution aging: several authors[46, 60] report that aging of glycine aqueous solutions improved the nucleation

probability under NPLIN. However, the nucleation probability of metal halides was found to be invariant to aging[65].

10. Effect of filtration and nanoparticle doping: Ward *et al.*[44] studied how the filtration and intentional addition of impurities, namely Fe_3O_4 nanoparticles, alter NPLIN probability. Filtration decreased the NPLIN probability while the addition of nanoparticles increased the NPLIN probability reported at a fixed observation time.

11. Product crystal alignment: In the experiments performed in aqueous urea by Garetz *et al.*[39], the direction of the needled-shaped crystals of urea were reported to be aligned with the polarization plane of the laser. However, Liu *et al.*[66], in their experiments using aqueous urea, observed the angle between crystal alignment and laser polarization to be random.

12. Irradiation pathway matters: When compared to laser intensity threshold values reported in the literature, Clair *et al.* [67] observed a lower value in experiments when passing the laser light via an air-liquid interface (from the vial top) through a supersaturated aqueous glycine solution. Unfortunately, in the same experiments, no trials were performed to pass the laser through the glass-liquid interface for comparison.

13. Direct solution-laser interaction matters: Kacker *et al.*[56], in their experiments with aqueous KCl, measured the pressure signal after a laser pulse at a fixed distance from the laser path within the vial. Even though the samples where laser light was masked with a black tape recorded higher radiation pressure compared to the samples which allowed the laser to pass through the solution, the former was not observed to undergo NPLIN.

In conclusion, while the observations from published experiments provide valuable insights into the NPLIN phenomenon, addressing the uncertainty surrounding its underlying mechanism is critical for realizing its full potential in industrial practice. Hence, the subsequent section will provide an overview of the proposed mechanisms for NPLIN.

1.2.2. PROPOSED MECHANISMS

In this section, we critically discuss the proposed NPLIN mechanisms and to what extent these mechanisms explain the experimental observation listed above.

OPTICAL KERR EFFECT (OKE)

The first hypothesized mechanism was based on the optical Kerr effect. This hypothesis states that the laser produces a weak torque that aligns

all anisotropically polarizable molecules (or clusters of molecules) with their most polarizable axis parallel to the direction of polarization of the incident light (Figure 1.4a). For instance, the observed alignment of urea crystals to the laser direction by Garetz *et al.*[39] was argued based on the urea molecule's ability to align their C_2 axes parallel to an applied laser's electric field. Consequently, it was proposed that the electric-field-induced alignment reduces the free energy barrier for nucleation. Later, a similar approach was used by the same authors and Sun *et al.*[49] to explain the polarization switching of both glycine and L-histidine polymorphs. It was shown that repeated units of α- and γ-polymorphs of glycine (or orthorhombic A and monoclinic B polymorphs of L-histidine) contain disc-like and rod-like polarizabilities, respectivily. Subsequently, they argued that circular polarized light would preferentially align disc-like structures, while linearly polarized light would align rod-like entities, and therefore different polarized light results in a change in polymorphic form. The effect of the laser's polarization on the polymorph of the product crystal has also been observed for several other simple organic molecules such as carbamazepine, and sulfathiazole [61, 62].

The plausibility of the OKE being responsible for the NPLIN effect was tested when Monte Carlo simulations of a Potts lattice gas model cast doubt on the amount of energy needed to properly align molecules in precritical solute clusters [68]. The field strength needed to lower the nucleation barrier by a sufficient amount to match NPLIN observations was found to be orders of magnitude higher than the field strengths employed in the experiment [68].

Although the Kerr effect hypothesis supports the observed correlation between the urea crystal and laser polarization by Garetz *et al.*, Liu *et al.*[66] reported the crystal orientation angle to be quite random under similar experimental conditions (observation 11). Sun *et al.*[49] in their experiments with glycine, observed a narrow window of temperature and supersaturation within which the circularly polarized light favored α-glycine while linearly polarized light favored γ-glycine (observation 7). This reported influence of laser polarization on glycine polymorphism by Sun *et al.* contradicts the results from Irimia *et al.*[64]. When using a single laser pulse in aqueous glycine solutions, Irimia *et al.* did not observe any effect of laser polarization on the type of polymorph formed in the experiment. Upon comparing the results of Irimia *et al.* with those of Sun *et al.*, who employed hundreds of laser pulses, one might suggest that the interaction of laser light with microscopic crystals after nucleation can trigger polymorphic transitions through polarization-dependent ablation and secondary nucleation. Interestingly, the experiments of Irimia et al., when employing multiple pulses of 1064 nm, showed an increase in the solution temperature. However, the effect of temperature rise on polymorph control is yet to be quantified.

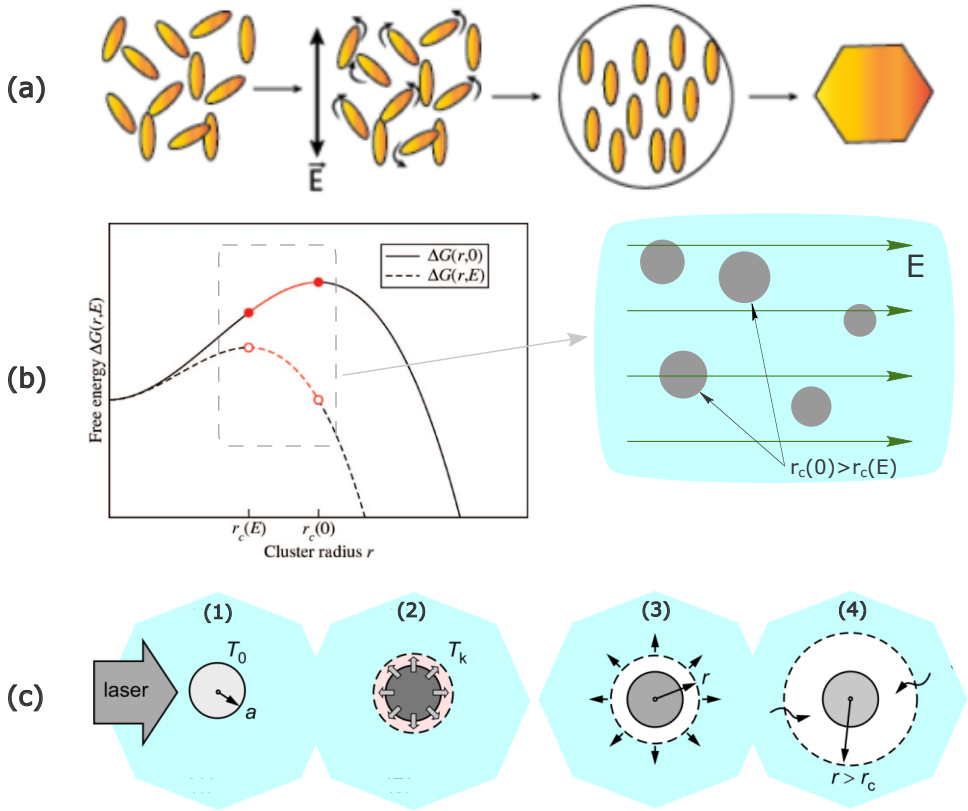

Figure 1.4.: **Plausible mechanisms for NPLIN.** (**a**) Field-induced alignment of molecules - optical Kerr effect. (**b**) Stabilization of otherwise subcritical clusters under electric field[45] - dielectric polarization (where $r_c(0)$ and $r_c(E)$ are the critical cluster radius in the absence and presence of laser light, respectively). (**c**) Evaporation of solvent surrounding a nanoparticle due to local heating.

In addition, the Kerr effect hypothesis fails to explain the reported laser peak-intensity threshold and the weak wavelength dependence on the nucleation probability. The whole basis of the Kerr effect lies in the ability of laser light to polarize a solute molecule, yet the NPLIN of solutes without anisotropic polarizability, such as metal halides, lacks explanation. Thus below we present the dielectric polarization hypothesis that attempts to explain the observed NPLIN of potassium halides such as KCl[65] and KBr[50].

DIELECTRIC POLARIZATION (DP)

The dielectric polarization mechanism suggests that isotropic polarization of pre-nucleating clusters by an electric field modifies the cluster's free energy by which it becomes stable. This means that a dielectrically homogeneous cluster smaller than the critical size, r_c, can be stabilized by an electric field if its dielectric constant exceeds that of the surrounding medium (Figure 1.4b). Unlike OKE which works on induced polarization of solutes under laser light, DP stems from differences in the dielectric permittivity of solutes compared to solvents. Including this effect in classical nucleation theory (CNT), the free energy of a cluster of radius r in the presence of an electric field E is given by[65]

$$\Delta G(r,E) = 4\pi r^2\gamma - \frac{4}{3}\pi r^3(A\ln S + \alpha E^2), \tag{1.6}$$

where γ is the solution-crystal interfacial tension, $A = \rho RT/M$, in which ρ is the mass density, R is the gas constant, M is the molar mass of the solid and S is the supersaturation ratio. The coefficient α defines an effective dielectric constant

$$\alpha = \frac{3\epsilon_0\epsilon_s}{2}\left(\frac{\epsilon_p - \epsilon_s}{\epsilon_p + 2\epsilon_s}\right). \tag{1.7}$$

For a particle with dielectric constant ϵ_p immersed in a medium of dielectric constant ϵ_s, the free energy is lowered in the presence of an electric field provided that ϵ_p is greater than ϵ_s - a critical criterion for DP to work. Assuming a Poisson distribution, the probability of obtaining at least one nucleus is calculated using

$$p(n \geq 1) = 1 - e^{-mj_{peak}} \tag{1.8}$$

where mj_{peak} is equal to the mean number of nuclei produced by a given laser peak-intensity j_{peak} and m is the lability. For lower peak intensities, using a truncated Taylor series for the exponential term in the above equation, a linear relation between probability and j_{peak} can be achieved[65]. From CNT, the probability of a cluster of size r within the solution is expressed using the Boltzmann distribution, $e^{-\Delta G(r,E)/(k_BT)}$. In the presence of laser light, under the conditions where the change in a cluster's bulk energy due to the light's electric field is significantly small ($\alpha E^2 \ll A\ln S$), we can analytically calculate the lability as[50]

$$m = \frac{3N_{\text{molecules}}\gamma\alpha}{2\pi\rho^3(k_BT\ln S)^2} \times \frac{e^{-\Delta G(r_c,0)/(k_BT)}}{\int_0^{r_c(0)} r^3 e^{-\Delta G(r,0)/(k_BT)}dr} \tag{1.9}$$

where $r_c(0)$ is the critical radius in the absence of an electric field. $N_{\text{molecules}}$ is the number of ion pairs within the volume illuminated by the laser, indicating an increase in the nucleation probability with an increase in the irradiated volume.

The dielectric polarization model successfully predicts the linear relation of the nucleation probability to low laser peak intensity for KCl[50] (Equation (1.8)). By doing so, it also hypothesizes a mechanism under which ionic solutes such as KCl and KBr[50], that have no preferred orientation under laser, can nucleate under NPLIN. Yet, it cannot explain the experimentally observed intensity threshold, j_0 (observation 8). Therefore, phenomenological models use a corrected value for the number of nuclei produced, $m(j_{peak} - j_0)$, to replicate the observed zero probabilities below j_0. Together with the laser peak-intensity threshold, the dielectric polarization model fails to answer the observed probability dependence on laser pulse duration, wavelength, and the polymorph selectivity under different laser polarizations[47, 49, 69] (observations 4, 5, and 7). Moreover, NPLIN of dissolved gases shown in Figure 1.3c in which the dissolved gas phase has a lower dielectric constant than water cannot be explained by the dielectric polarization hypothesis (observation 6). To explain the observed NPLIN of dissolved gases and the effect of impurities on NPLIN probabilities of NH_4Cl[44], we present below the impurity heating hypothesis, which attempts to explain NPLIN as a function of inherent impurities rather than the solute-laser interaction.

IMPURITY HEATING (IH)

The impurity heating hypothesis suggests that the interaction of the laser irradiation with impurities plays a significant role in NPLIN. This hypothesis emerged from the inability of the OKE and DP mechanisms to explain certain observations common in NPLIN experiments, particularly the existence of a threshold below which no nucleation is observed and the pronounced effect of filtration on NPLIN (observation 10). In a nutshell, this hypothesis assumes a scenario where insoluble impurities such as nanoparticles absorb laser energy at the wavelength of irradiation and rapidly heat and evaporate the surrounding solution. This phenomenon is expected to trigger nucleation by locally enhancing the supersaturation.

In order to test this, Ward *et al.*[44] studied how the intentional addition of impurities, namely Fe_3O_4 nanoparticles and a surfactant (polyethylene glycol, $M_r = 8000$), alter the NPLIN probability and number of crystals nucleating in supersaturated aqueous NH_4Cl solutions. First, they compared filtered and non-filtered aqueous NH_4Cl solutions. The filtration was carried out using a 0.2 µm pore-size membrane with freshly prepared samples at high temperatures to justify that only the impurities were filtered out as opposed to the solute clusters. A strong

difference in nucleation probability and the number of crystals was observed between filtered and unfiltered samples. The filtered samples showed a lower nucleation probability and a lower number of crystals. In the same work, a similar effect due to filtration was observed in other systems, such as in aqueous urea and glycine. Furthermore, supporting the role of impurities, the addition of both nanoparticles and surfactant showed an increase in the NPLIN probability. While the impurities due to nanoparticles and surfactant would serve as active sites for the local increase in supersaturation, the surfactant was also expected to stabilize the dispersion of impurities - promoting more viable nucleation sites.

Javid *et al.*[70] performed NPLIN experiments with glycine for both filtered and unfiltered samples. Irrespective of whether the solutions were irradiated or not, filtration of glycine solutions across all supersaturations resulted only in an α-polymorph under the influence of the laser. The unfiltered samples at higher supersaturations (1.5 and 1.6) showed a significant presence of a γ-polymorph (40%) when irradiated, while non-irradiated solutions nucleated almost exclusively the α-polymorph at all supersaturations.

Ward *et al.*[44] reported that for systems with CO_2, KCl, NH_4Cl and CH_4N_2O, NPLIN was not observed using unfocused femtosecond laser pulses (∼110 fs, j_{peak} = 30 MW cm^{-2}), while nanosecond pulses (∼5 ns, j_{peak} = 12 MW cm^{-2}) induced nucleation. The total energy per pulse, ∼ j_{peak} × pulse duration, limits the energy available for a nanoparticle to absorb. This absorbed energy is hypothesized to evaporate the solvent surrounding the nanoparticle and form a local vapor-filled cavity (Figure 1.4c). Consequently, a region of high solute concentration at the vapor-liquid interface is expected to emerge, due to the solvent that evaporated. This increased solute concentration at the vapor-liquid interface is expected to contribute to a higher local supersaturation and therefore trigger nucleation. The observed differences in nucleation probabilities between the aforementioned pulse durations were argued based on the energy available for the local cavity formation surrounding the nanoparticle (observation 4). This supports the hypothesis that heating solid nanoparticle impurities, which are intrinsically present within a solution, act as active sites to nucleation.

The nanoparticle heating hypothesis explains the observed laser intensity threshold because enough energy must be supplied to induce cavitation around a nanoparticle. The nanoparticle heating hypothesis however fails to explain two sets of reported experimental results, namely the alignment of urea crystals[39] and the influence of laser polarization on polymorphic form[49] (observation 7). Interestingly, Liu *et al.*[66] failed to reproduce this alignment effect in aqueous urea upon exposure to linearly polarized nanosecond pulses. One possible explanation for this observed alignment of crystals might be due to

hydrodynamic interactions between the crystal and the surrounding fluid. The Marangoni flow induced by local heating of the solution could apply torque and align the crystals. At the current time, this explanation is merely our speculation without quantification of the flow fields and the local sample heating under studied experimental conditions. Irimia *et al.*[64] quantified the temperature increase of aqueous glycine solutions when subjected to one or more pulses of 532 and 1064 nm. Both Alexander *et al.* and Irimia *et al.* observed that laser polarization does not influence the polymorph formed. A possible explanation for the difference in the observations made could rely on the nature of the impurity rather than the solute. Moreover, the ability of nanoparticles to have a difference in absorption, based on the ellipticity of laser polarization (circular or linear), is left unexplored. This difference in laser absorption could dictate the magnitude of the local supersaturation and thus the polymorph formed.

1.3. RESEARCH GAPS

The proposed mechanisms for NPLIN, including the Optical Kerr effect (OKE), Dielectric polarization (DP), and Impurity heating (IH), offer intriguing explanations for part of the observed phenomena discussed in section 1.2 . However, none of these mechanisms alone can fully account for all experimental observations. Hence, more efforts are required to extend our understanding of NPLIN from both experimental and theoretical perspectives. Furthermore, a thorough literature review on NPLIN reveals several additional research gaps:

- A significant research gap exists in the methodology employed for studying NPLIN, particularly concerning the manual nature of traditional experiments within mL vials. In literature these methods are frequently criticized for their limited statistical accuracy and reproducibility. Additionally, the influence of various laser characteristics, such as intensity, wavelength, and duration, on nucleation kinetics has not been studied in a continuous setup for micro-litre solution volumes.
- While extensive research has focused on specific laser parameters such as laser intensity, laser pulse duration and laser wavelength on NPLIN kinetics, others like laser exposed volume and irradiation position relative to air/solution interface within glass vial remain largely unexplored.
- Although the nanoparticle heating mechanism could explain the majority of the experimental observations listed in section 1.2, a notable research gap exists in understanding the nanoparticle heating mechanism, particularly concerning the nature and origin

of impurities. Furthermore, there is a lack of comprehensive understanding of how laser pulses interact with impurity nanoparticles and how factors such as their size, material, and concentration affect NPLIN kinetics.

- Despite numerous experimental observations related to NPLIN, there remains a gap in integrating these observations with mechanistic models. Bridging this gap is crucial for validating and refining existing theories, as well as for guiding future experimental design to advance our understanding of NPLIN mechanisms.

1.4. RESEARCH QUESTIONS AND OBJECTIVES

Having identified critical research gaps in NPLIN literature, the overarching aim of this Ph.D. project is to address some of these questions to attain a better understanding of the fundamental mechanism behind NPLIN. Innovative experimental setups spanning solution volumes from microliters to milliliters were designed and implemented to facilitate this investigation

The primary research questions that guide this project are the following:

- **Chapter 2:** How do laser parameters, such as the laser exposed volume and the laser irradiation position, influence the NPLIN kinetics of supersaturated potassium chloride solutions? Furthermore, what can the results and analysis of these experiments tell us about the mechanism behind NPLIN?
- **Chapter 3:** How can we leverage a droplet-based microfluidic platform to quantify the effects of various laser and solution parameters on NPLIN kinetics? And how do these results compare with traditional vial-based methods, especially in relation to the proposed mechanisms in the NPLIN literature?
- **Chapter 4:** How do nanoparticle properties, such as material and concentration, affect NPLIN kinetics in supersaturated urea solutions, within the context of the proposed nanoparticle heating mechanism?

In Chapter 2, the effects of laser-exposed volume and laser irradiation position on nucleation probability within milliliter-scale volumes of supersaturated aqueous potassium chloride are investigated. These results are then analyzed within the context of the dielectric polarization mechanism and nanoparticle heating mechanism.

Chapter 3 introduces a transition from traditional vial-based NPLIN investigation to a droplet-based microfluidic platform, enhanced by deep learning for automated crystallization detection. The microfluidic

setup was used to explore how laser intensity, laser wavelength, supersaturation, solution filtration and intentional doping influences nucleation probability in supersaturated KCl solutions. Furthermore, the results are analyzed within the context of the nanoparticle heating mechanism, emphasizing the potential role of nanoimpurities through these experiments.

In Chapter 4, a traditional vial based method was used to investigate the impact of solution filtration, as well as variations in nanoparticle concentration and material type on the NPLIN probability of supersaturated urea solutions. Furthermore, the findings were discussed in the perspective of nanoparticle heating mechanism.

Chapter 5 describes conclusions and recommendations related to this research.

BIBLIOGRAPHY

[1] A. S. Myerson. Second Edition. Woburn: Butterworth-Heinemann, 2002. isbn: 978-0-7506-7012-8. url: https://www.sciencedirect.com/science/article/pii/B9780750670128500008.

[2] A. Lewis, M. Seckler, and H. Kramer. Vol. 1. Cambridge University Press., 2015. isbn: 978-1-107-.

[3] D. Kashchiev. Vol. 1. Butterworth-Heinman, 2000. isbn: 0-7506-4682-9.

[4] M. Jehannin, A. Rao, and H. Cölfen. "New Horizons of Nonclassical Crystallization". In: *Journal of the American Chemical Society* 141.26 (2019). PMID: 31173682, pp. 10120–10136. doi: 10.1021/jacs.9b01883. eprint: https://doi.org/10.1021/jacs.9b01883. url: https://doi.org/10.1021/jacs.9b01883.

[5] H. J. M. Kramer and G. M. Van Rosmalen. ""Crystallization"". In: *Encyclopedia of Separation Science* 1 (2000), pp. 64–84. doi: https://doi.org/10.1016/B0-12-226770-2/00031-4.

[6] J. W. Mullin. *Crystallization*. Butterworth-Heinemann, 2004.

[7] D. Kashchiev. "Classical nucleation theory approach to two-step nucleation of crystals". In: *Journal of Crystal Growth* 530 (2020), p. 125300. issn: 0022-0248. doi: https://doi.org/10.1016/j.jcrysgro.2019.125300. url: http://www.sciencedirect.com/science/article/pii/S0022024819305159.

[8] D. Erdemir, A. Y. Lee, and A. S. Myerson. "Nucleation of Crystals from Solution: Classical and Two-Step Models". In: *Accounts of Chemical Research* 42.5 (2009). PMID: 19402623, pp. 621–629. doi: 10.1021/ar800217x. eprint: https://doi.org/10.1021/ar800217x. url: https://doi.org/10.1021/ar800217x.

[9] P. G. Vekilov. "Nucleation". In: *Crystal Growth $&Design* 10.12 (2010). PMID: 21132117, pp. 5007–5019. doi: 10.1021/cg1011633. eprint: https://doi.org/10.1021/cg1011633. url: https://doi.org/10.1021/cg1011633.

[10] S. Karthika, T. K. Radhakrishnan, and P. Kalaichelvi. “A Review of Classical and Nonclassical Nucleation Theories”. In: *Crystal Growth & Design* 16.11 (Oct. 2016), pp. 6663–6681. issn: 1528-7505. doi: 10.1021/acs.cgd.6b00794.

[11] D. Erdemir, A. Y. Lee, and A. S. Myerson. “Nucleation of Crystals from Solution: Classical and Two-Step Models”. In: *Accounts of Chemical Research* 42.5 (Apr. 2009), pp. 621–629. doi: 10.1021/ar800217x.

[12] A. S. Myerson and B. L. Trout. “Nucleation from Solution”. In: *Science* 341.6148 (2013), pp. 855–856. doi: https://doi.org/10.1126/science.1243022.

[13] J. W. Cahn. “Theory of crystal growth and interface motion in crystalline materials”. In: *Acta Metallurgica* 8.8 (Aug. 1960), pp. 554–562. issn: 0001-6160. doi: 10.1016/0001-6160(60)90110-3.

[14] W. B. Hillig and D. Turnbull. “Theory of Crystal Growth in Undercooled Pure Liquids”. In: *The Journal of Chemical Physics* 24.4 (Apr. 1956), pp. 914–914. issn: 1089-7690. doi: 10.1063/1.1742646.

[15] H. B. Eral, M. O’Mahony, R. Shaw, B. L. Trout, A. S. Myerson, and P. S. Doyle. “Composite Hydrogels Laden with Crystalline Active Pharmaceutical Ingredients of Controlled Size and Loading”. In: *Chemistry of Materials* 26.21 (2014), pp. 6213–6220. doi: 10.1021/cm502834h. eprint: https://doi.org/10.1021/cm502834h. url: https://doi.org/10.1021/cm502834h.

[16] J. H. ter Horst, C. Schmidt, and J. Ulrich. In: *Handbook of Crystal Growth (Second Edition)*. Second Edition. Handbook of Crystal Growth. Boston: Elsevier, 2015, pp. 1317–1349. isbn: 978-0-444-63303-3. url: https://www.sciencedirect.com/science/article/pii/B9780444633033000328.

[17] H. B. Eral, V. López-Mejías, M. O’Mahony, B. L. Trout, A. S. Myerson, and P. S. Doyle. “Biocompatible Alginate Microgel Particles as Heteronucleants and Encapsulating Vehicles for Hydrophilic and Hydrophobic Drugs”. In: *Crystal Growth $&Design* 14.4 (2014), pp. 2073–2082. doi: 10.1021/cg500250e. eprint: https://doi.org/10.1021/cg500250e. url: https://doi.org/10.1021/cg500250e.

[18] A. Lewis, M. Seckler, H. Kramer, and G. van Rosmalen. *Industrial Crystallization: Fundamentals and Applications*. 2015.

[19] D. Chakraborty and G. N. Patey. “How crystals nucleate and grow in aqueous NaCl solution”. In: *Journal of Physical Chemistry Letters* 4.4 (2013), pp. 573–578. issn: 1948-7185. doi: 10.1021/jz302065w. url: https://doi.org/10.1021/jz302065w.

[20] J. F. Lutsko and J. Lam. “Classical density functional theory, unconstrained crystallization, and polymorphic behavior”. In: *Physical Review E* 98.1 (2018). issn: 24700053. doi: 10.1103/PhysRevE.98.012604. arXiv: 1805.05673.

[21] P. G. Vekilov. “Nucleation of protein crystals”. In: *Progress in Crystal Growth and Characterization of Materials* 62.2 (June 2016), pp. 136–154. issn: 0960-8974. doi: 10.1016/J.PCRYSGROW.2016.04.007. url: https://www.sciencedirect.com/science/article/pii/S0960897416300109.

[22] T. Nakamuro, M. Sakakibara, H. Nada, K. Harano, and E. Nakamura. “Capturing the Moment of Emergence of Crystal Nucleus from Disorder”. In: *Journal of the American Chemical Society* 143.4 (2021), pp. 1763–1767. issn: 15205126. doi: 10.1021/jacs.0c12100.

[23] A. R. Finney and M. Salvalaglio. “Molecular simulation approaches to study crystal nucleation from solutions: Theoretical considerations and computational challenges”. In: *WIREs Computational Molecular Science* 14.1 (Nov. 2023). issn: 1759-0884. doi: 10.1002/wcms.1697.

[24] Š. Selimović, Y. Jia, and S. Fraden. “Measuring the Nucleation Rate of Lysozyme using Microfluidics”. In: *Crystal Growth & Design* 9.4 (Feb. 2009), pp. 1806–1810. issn: 1528-7505. doi: 10.1021/cg800990k.

[25] I. S. Lee, K. T. Kim, A. Y. Lee, and A. S. Myerson. “Concomitant Crystallization of Glycine on Patterned Substrates: The Effect of pH on the Polymorphic Outcome”. In: *Crystal Growth & Design* 8.1 (Jan. 2008), pp. 108–113. issn: 1528-7505. doi: 10.1021/cg700890m.

[26] D. Knezic, J. Zaccaro, and A. S. Myerson. “Nucleation Induction Time in Levitated Droplets”. In: *The Journal of Physical Chemistry B* 108.30 (June 2004), pp. 10672–10677. issn: 1520-5207. doi: 10.1021/jp049586s.

[27] K. D. Harris, C. E. Hughes, and P. A. Williams. “Monitoring the evolution of crystallization processes by in-situ solid-state NMR spectroscopy”. In: *Solid State Nuclear Magnetic Resonance* 65 (Feb. 2015), pp. 107–113. issn: 0926-2040. doi: 10.1016/j.ssnmr.2014.11.004.

[28] S. Kulkarni. “Crystal Nucleation and Polymorph Control”. PhD thesis. 2014. doi: 10.4233/UUID:321CB48F-9B80-4AA6-9298-223F4250F7C9.

[29] R. J. P. Eder, E. K. Schmitt, J. Grill, S. Radl, H. Gruber-Woelfler, and J. G. Khinast. “Seed loading effects on the mean crystal size of acetylsalicylic acid in a continuous-flow crystallization device”. In: *Crystal Research and Technology* 46.3 (Feb. 2011), pp. 227–237. issn: 1521-4079. doi: 10.1002/crat.201000634.

[30] A. N. Kalbasenka, L. C. P. Spierings, A. E. M. Huesman, and H. J. M. Kramer. “Application of Seeding as a Process Actuator in a Model Predictive Control Framework for Fed-Batch Crystallization of Ammonium Sulphate”. In: *Particle & Particle Systems Characterization* 24.1 (May 2007), pp. 40–48. issn: 1521-4117. doi: 10.1002/ppsc.200601053.

[31] S. H. Chung, D. L. Ma, and R. D. Braatz. “Optimal seeding in batch crystallization”. In: *The Canadian Journal of Chemical Engineering* 77.3 (June 1999), pp. 590–596. issn: 1939-019X. doi: 10.1002/cjce.5450770322.

[32] J. D. Ward, D. A. Mellichamp, and M. F. Doherty. “Choosing an operating policy for seeded batch crystallization”. In: *AIChE Journal* 52.6 (Mar. 2006), pp. 2046–2054. issn: 1547-5905. doi: 10.1002/aic.10808.

[33] L. d. l. S. Castillo-Peinado and M. D. Luque de Castro. “The role of ultrasound in pharmaceutical production: sonocrystallization”. In: *Journal of Pharmacy and Pharmacology* 68.10 (July 2016), pp. 1249–1267. issn: 0022-3573. doi: 10.1111/jphp.12614.

[34] M. Luque de Castro and F. Priego-Capote. “Ultrasound-assisted crystallization (sonocrystallization)”. In: *Ultrasonics Sonochemistry* 14.6 (Sept. 2007), pp. 717–724. issn: 1350-4177. doi: 10.1016/j.ultsonch.2006.12.004.

[35] S. Kaur Bhangu, M. Ashokkumar, and J. Lee. “Ultrasound Assisted Crystallization of Paracetamol: Crystal Size Distribution and Polymorph Control”. In: *Crystal Growth & Design* 16.4 (Mar. 2016), pp. 1934–1941. issn: 1528-7505. doi: 10.1021/acs.cgd.5b01470.

[36] J. Zaccaro, J. Matic, A. S. Myerson, and B. A. Garetz. “Non-photochemical, laser-induced nucleation of supersaturated aqueous glycine produces unexpected γ-polymorph”. In: *Crystal Growth and Design* 1.1 (2001), pp. 5–8. issn: 15287483. doi: 10.1021/cg0055171.

[37] A. J. Alexander and P. J. Camp. “Non-photochemical laser-induced nucleation”. In: *The Journal of Chemical Physics* 150.4 (2019), pp. 040901–99. doi: https://doi.org/10.1063/1.5079328.

[38] B. A. Garetz, J. E. Aber, N. L. Goddard, R. G. Young, and A. S. Myerson. “Nonphotochemical, Polarization-Dependent, Laser-Induced Nucleation in Supersaturated Aqueous Urea Solutions”. In: *Physical Review Letters* 77.16 (1996), pp. 3475–3476. url: https://link.aps.org/doi/10.1103/PhysRevLett.77.3475.

[39] B. A. Garetz, J. E. Aber, N. L. Goddard, R. G. Young, and A. S. Myerson. “Nonphotochemical, polarization-dependent, laser-induced nucleation in supersaturated aqueous urea solutions”. In: *Physical Review Letters* 77.16 (1996), pp. 3475–3476. issn: 10797114. doi: 10.1103/PhysRevLett.77.3475.

[40] A. J. Alexander and P. J. Camp. “Single Pulse, Single Crystal Laser-Induced Nucleation of Potassium Chloride”. In: *Crystal Growth & Design* 9.2 (2009), pp. 958–963. doi: https://doi.org/10.1021/cg8007415.

[41] M. R. Ward, A. M. Mackenzie, and A. J. Alexander. “Role of Impurity Nanoparticles in Laser-Induced Nucleation of Ammonium Chloride”. In: *Crystal Growth & Design* 16.12 (Dec. 2016), pp. 6790–6796. issn: 1528-7483. doi: 10.1021/acs.cgd.6b00882. url: https://doi.org/10.1021/acs.cgd.6b00882.

[42] A. Ikni, B. Clair, P. Scouflaire, S. Veesler, J.-M. Gillet, N. El Hassan, F. Dumas, and A. Spasojević-de Biré. “Experimental Demonstration of the Carbamazepine Crystallization from Non-photochemical Laser-Induced Nucleation in Acetonitrile and Methanol”. In: *Crystal Growth & Design* 14.7 (2014), pp. 3286–3299. issn: 1528-7483. doi: 10.1021/cg500163c. url: http://dx.doi.org/10.1021/cg500163c.

[43] T. Okutsu, K. Furuta, M. Terao, H. Hiratsuka, A. Yamano, N. Ferté, and S. Veesler. “Light-Induced Nucleation of Metastable Hen Egg-White Lysozyme Solutions”. In: *Crystal Growth & Design* 5.4 (July 2005), pp. 1393–1398. doi: 10.1021/cg049604v.

[44] M. R. Ward, A. M. Mackenzie, and A. J. Alexander. “Role of Impurity Nanoparticles in Laser-Induced Nucleation of Ammonium Chloride”. In: *Crystal Growth $&Design* 16.12 (2016), pp. 6790–6796. issn: 15287505. doi: 10.1021/acs.cgd.6b00882.

[45] M. R. Ward, W. J. Jamieson, C. A. Leckey, and A. J. Alexander. “Laser-induced nucleation of carbon dioxide bubbles”. In: *Journal of Chemical Physics* 142.14 (2015), p. 144501. issn: 00219606.

doi: 10.1063/1.4917022. url: http://dx.doi.org/10.1063/1.4917022.

[46] J. Zaccaro, J. Matic, A. S. Myerson, and B. A. Garetz. “Nonphotochemical, Laser-Induced Nucleation of Supersaturated Aqueous Glycine Produces Unexpected gamma-Polymorph”. In: *Crystal Growth $&Design* 1.1 (2001), pp. 5–8. doi: 10.1021/cg0055171. eprint: https://doi.org/10.1021/cg0055171. url: https://doi.org/10.1021/cg0055171.

[47] X. Sun, B. A. Garetz, and A. S. Myerson. “Polarization switching of crystal structure in the nonphotochemical laser-induced nucleation of supersaturated aqueous L-histidine”. In: *Crystal Growth and Design* 8.5 (2008), pp. 1720–1722. issn: 15287483. doi: 10.1021/cg800028v.

[48] J. Matic, X. Sun, B. A. Garetz, and A. S. Myerson. “Intensity, Wavelength, and Polarization Dependence of Nonphotochemical Laser-Induced Nucleation in Supersaturated Aqueous Urea Solutions”. In: *Crystal Growth & Design* 5.4 (June 2005), pp. 1565–1567. doi: 10.1021/cg050041c.

[49] A. Sun, B. A. Garetz, and A. S. Myerson. “Supersaturation and Polarization Dependence of Polymorph Control in the Nonphotochemical Laser-Induced Nucleation (NPLIN) of Aqueous Glycine Solutions”. In: *Crystal Growth & Design* 6.3 (2006), pp. 684–689. doi: https://doi.org/10.1021/cg050460+.

[50] M. R. Ward and A. J. Alexander. “Nonphotochemical laser-induced nucleation of potassium halides: Effects of wavelength and temperature”. In: *Crystal Growth and Design* 12.9 (2012), pp. 4554–4561. issn: 15287483. doi: 10.1021/cg300750c.

[51] X. Sun, B. A. Garetz, M. F. Moreira, and P. Palffy-Muhoray. “Nonphotochemical laser-induced nucleation of nematic phase and alignment of nematic director from a supercooled thermotropic liquid crystal”. In: *Physical Review E - Statistical, Nonlinear, and Soft Matter Physics* 79.2 (2009), pp. 1–6. issn: 15393755. doi: 10.1103/PhysRevE.79.021701.

[52] M. R. Ward, S. McHugh, and A. J. Alexander. “Non-photochemical laser-induced nucleation of supercooled glacial acetic acid”. In: *Physical Chemistry Chemical Physics* 14.1 (2012), pp. 90–93. issn: 14639076. doi: 10.1039/c1cp22774b.

[53] B. C. Knott, J. L. Larue, A. M. Wodtke, M. F. Doherty, and B. Peters. “Communication: Bubbles, crystals, and laser-induced nucleation”. In: *Journal of Chemical Physics* 134.17 (2011), p. 171102. issn: 00219606. doi: 10.1063/1.3582897.

[54] I. S. Lee, J. M. Evans, D. Erdemir, A. Y. Lee, B. A. Garetz, and A. S. Myerson. “Nonphotochemical laser induced nucleation of hen egg white lysozyme crystal”. In: *Crystal Growth and Design* 8.12 (2008), pp. 4255–4261. issn: 15287483. doi: 10.1021/cg800696u.

[55] E. R. Barber. Chemistry thesis and dissertation collection, 2021.

[56] R. Kacker, S. Dhingra, D. Irimia, M. K. Ghatkesar, A. Stankiewicz, H. J. Kramer, and H. B. Eral. “Multiparameter Investigation of Laser-Induced Nucleation of Supersaturated Aqueous KCl Solutions”. In: *Crystal Growth $&Design* 18.1 (2018), pp. 312–317. doi: 10.1021/acs.cgd.7b01277.

[57] M. R. Ward, I. Ballingall, M. L. Costen, K. G. McKendrick, and A. J. Alexander. “Nanosecond pulse width dependence of nonphotochemical laser-induced nucleation of potassium chloride”. In: *Chemical Physics Letters* 481.1-3 (2009), pp. 25–28. doi: 10.1016/j.cplett.2009.09.049. url: http://dx.doi.org/10.1016/j.cplett.2009.09.049.

[58] C. Duffus, P. J. Camp, and A. J. Alexander. “Spatial control of crystal nucleation in agarose gel”. In: *Journal of the American Chemical Society* 131.33 (2009), pp. 11676–11677. issn: 00027863. doi: 10.1021/ja905232m.

[59] T. Hua, O. Gowayed, D. Grey-Stewart, B. A. Garetz, and R. L. Hartman. “Microfluidic Laser-Induced Nucleation of Supersaturated Aqueous KCl Solutions”. In: *Crystal Growth $&Design* 19.6 (2019), pp. 3491–3497. doi: 10.1021/acs.cgd.9b00362.

[60] T. Hua, C. Valentin-Valentin, O. Gowayed, S. Lee, B. A. Garetz, and R. L. Hartman. “Microfluidic Laser-Induced Nucleation of Supersaturated Aqueous Glycine Solutions”. In: *Crystal Growth & Design* 20.10 (2020), pp. 6502–6509. doi: https://doi.org/10.1021/acs.cgd.0c00669.

[61] A. Ikni, B. Clair, P. Scouflaire, S. Veesler, J. M. Gillet, N. El Hassan, F. Dumas, and A. Spasojević-De Biré. “Experimental demonstration of the carbamazepine crystallization from non-photochemical laser-induced nucleation in acetonitrile and methanol”. In: *Crystal Growth $&Design* 14.7 (2014), pp. 3286–3299. issn: 15287505. doi: 10.1021/cg500163c.

[62] W. Li, A. Ikni, P. Scouflaire, X. Shi, N. El Hassan, P. Gémeiner, J. M. Gillet, and A. Spasojević-De Biré. “Non-Photochemical Laser-Induced Nucleation of Sulfathiazole in a Water/Ethanol Mixture”. In: *Crystal Growth $&Design* 16.5 (2016), pp. 2514–2526. issn: 15287505. doi: 10.1021/acs.cgd.5b01526.

[63] Y. Liu, M. H. Van Den Berg, and A. J. Alexander. “Supersaturation dependence of glycine polymorphism using laser-induced nucleation, sonocrystallization and nucleation by mechanical shock”. In: *Physical Chemistry Chemical Physics* 19.29 (2017), pp. 19386–19392. issn: 14639076. doi: 10.1039/c7cp03146g.

[64] D. Irimia, J. Jose Shirley, A. S. Garg, D. P. Nijland, A. E. D. M. van der Heijden, H. J. M. Kramer, and H. B. Eral. “Influence of Laser Parameters and Experimental Conditions on Nonphotochemical Laser-Induced Nucleation of Glycine Polymorphs”. In: *Crystal Growth $&Design* 21.1 (2021), pp. 631–641. doi: 10.1021/acs.cgd.0c01415. url: https://doi.org/10.1021/acs.cgd.0c01415.

[65] A. J. Alexander and P. J. Camp. “Single pulse, single crystal laser-induced nucleation of potassium chloride”. In: *Crystal Growth $&Design* 9.2 (2009), pp. 958–963. issn: 15287505. doi: 10.1021/cg8007415.

[66] Y. Liu, M. R. Ward, and A. J. Alexander. “Polarization independence of laser-induced nucleation in supersaturated aqueous urea solutions”. In: *Physical Chemistry Chemical Physics* 19.5 (2017), pp. 3464–3467. issn: 14639076. doi: 10.1039/c6cp07997k.

[67] B. Clair, A. Ikni, W. Li, P. Scouflaire, V. Quemener, and A. Spasojevic-de Bire. “A new experimental setup for high-throughput controlled non-photochemical laser-induced nucleation: application to glycine crystallization”. In: *Journal of Applied Crystallography* 47 (2014), pp. 1252–1260. doi: https://doi.org/10.1107/S160057671401098X.

[68] B. C. Knott, M. F. Doherty, and B. Peters. “A simulation test of the optical Kerr mechanism for laser-induced nucleation”. In: *The Journal of chemical physics* 134.15 (2011), p. 154501. issn: 0021-9606. doi: 10.1063/1.3574010.

[69] B. A. Garetz, J. Matic, and A. S. Myerson. “Polarization Switching of Crystal Structure in the Nonphotochemical Light-Induced Nucleation of Supersaturated Aqueous Glycine Solutions”. In: *Physical Review Letters* 89.17 (2002), pp. 1–4. issn: 10797114. doi: 10.1103/PhysRevLett.89.175501.

[70] N. Javid, T. Kendall, I. S. Burns, and J. Sefcik. “Filtration suppresses laser-induced nucleation of glycine in aqueous solutions”. In: *Crystal Growth $&Design* 16.8 (2016), pp. 4196–4202. issn: 15287505. doi: 10.1021/acs.cgd.6b00046.

2

EFFECT OF LASER EXPOSED VOLUME AND IRRADIATION POSITION ON NON-PHOTOCHEMICAL LASER-INDUCED NUCLEATION OF POTASSIUM CHLORIDE SOLUTIONS

The influence of the laser exposed volume and the irradiation position on non-photochemical laser induced nucleation (NPLIN) of supersaturated potassium chloride solutions is studied in water. The effect of exposed volume on NPLIN probability is examined by exposing distinct volumes of aqueous potassium chloride solutions in vials of millilitre volume at two different supersaturations (1.034 and 1.050) and laser intensities (10 and 23 MW/cm^2). Higher NPLIN probabilities were observed with increasing laser-exposed volume as well as with increasing supersaturation and laser intensity. The measured NPLIN probabilities at different exposed volumes are questioned in the context of dielectric polarization mechanism and classic nucleation theory. No significant change in NPLIN probability was observed when samples were irradiated from the bottom, top or middle of the vial. However, a significant increase in nucleation probability was observed upon irradiation through the solution meniscus. We discuss these results in terms of mechanism proposed for NPLIN.

This chapter is based on Vikram Korede, Mias Veldhuis, Frederico Marques Penha, Nagaraj Nagalingam, PingPing Cui, Antoine E.D.M. Van der Heijden, Herman J.M. Kramer, and Hüseyin Burak Eral, Crystal Growth & Design 2023 23(11), 8163-8172

2.1. INTRODUCTION

Controlling nucleation in a crystallization process has direct implications on production of crystals we encounter in products ranging from pharmaceuticals to explosives[1–6]. Alternative crystallization methods, including Non-Photochemical Laser Induced Nucleation (NPLIN), have been extensively studied over the past decades, to provide spatio-temporal control over crystal nucleation. In NPLIN, a supersaturated solution is exposed to an intense laser pulse that induces nucleation in a drastically reduced induction time without absorbing any light at the irradiated wavelength[5, 7].

Ever since its discovery, NPLIN has been observed in many systems: small inorganic compounds [8–10], small to large organics [11–16], proteins [17, 18], liquid crystals [19], supercooled liquids [10] and even gas bubbles [20, 21]. Subsequently, the NPLIN effect with key experimental observations can be summarized as: (i) Nucleation probabilities appears to be independent of the tested laser wavelengths and are a function of supersaturation and peak intensity of the laser [13, 17, 22, 23]; (ii) There exists a threshold peak intensity below which nucleation is not induced [8, 10, 13, 23, 24]; (iii) Whilst not a requirement for NPLIN, aging of samples has shown to have an influence on the nucleation probabilities upon laser irradiation [11, 23, 25]; (iv) The presence of added nanoparticles acting as impurities enhances the nucleation probability of NPLIN[26, 27].These observations are summarized and discussed at length in a recent review article [5, 7].

Several mechanisms have been proposed to explain the aforementioned experimental observations. The first proposed mechanism is based on the Optical Kerr Effect (OKE), where the molecules in precritical clusters may align with the direction of the laser electric field facilitating the nucleation [28]. This mechanism corroborates observations that some polymorphs could be favoured, depending on laser characteristics (intensity, wavelength, polarization). However, Monte Carlo simulations of a Potts lattice gas model cast doubt on the amount of energy needed to properly align molecules in precritical solute clusters, as the field strength needed to lower the nucleation barrier to match NPLIN observations was found to be orders of magnitude higher than the field strengths employed in the experiments[21]. In addition, later studies on aqueous potassium chloride systems showed that NPLIN of small inorganic compounds without a preferential polarization axis was also possible, ruling out OKE mechanism in KCl[23].

Alexander et al.[23] proposed the Dielectric Polarization (DP) model to quantitatively describe the influence of a laser beam incident on aqueous potassium chloride solutions. The model exploits the difference in the dielectric constant of a cluster of solute molecules, ϵ_p, and the dielectric constant of the surrounding medium, ϵ_S. In the presence of an electric field and under the constraint that the $\epsilon_p > \epsilon_S$, the

free energy change of cluster formation (ΔG) is lowered by a number proportional to $-v(\epsilon_p - \epsilon_S)E^2$, where v is the volume of the cluster and E is the electric field strength[5]. In the presence of electric field, the critical radius, $r_c(I)$, and the height of the nucleation barrier, $\Delta G_c(I)$, are calculated using the Classical Nucleation Theory approach. As a result of the decreased nucleation barrier, any existing precritical clusters become critical following exposure to the laser, inducing nucleation. According to Alexander et al., the number of precritical clusters to become viable crystals ($N_{crystals}$) is a function of the lability constant m and the peak laser intensity I so that $N_{crystals} = mI$, where m is a function of the solute/solvent characteristics and the number of solute molecules present in the volume irradiated by the laser. However, studies investigating the NPLIN effect on carbon dioxide bubbles showed that NPLIN is also possible when $\epsilon_p > \epsilon_S$ is not satisfied [20, 29], casting doubt on the applicability of the DP model.

The third potential mechanism proposed is based on the heating of nanoparticle impurities inherently present in the system as soluble molecular impurities (intrinsic) and/or dust particles (extrinsic) when exposed to the laser beam. The heating of the nanoparticle results in vaporizing a volume of liquid surrounding them, leading to the formation of a vapor cavity, following which a region of increased solute concentration may form near the vapor/liquid interface upon which the solute molecules are more likely to cluster and nucleate. A consensus on which model accounts for all observations was still not reached. While the Optical Kerr Effect and the Dielectric Polarization model can explain several observations in NPLIN experiments, they fail to explain the nucleation of carbon dioxide bubbles, the lowering in nucleation probability by filtration of the solution, or the increase in nucleation probability by intentionally doping with nanoparticles [20, 21, 26, 27].

Among the many studies published in NPLIN literature, various parameters including supersaturation, laser intensity, and polarization [8, 10, 13, 14, 30], sample filtration [26], and intentional doping with impurities [27] have been shown to influence measured nucleation probabilities. Despite the broad literature on NPLIN, a comparison between different reports is challenging due to variation of many crucial experimental parameters such as geometry (e.g. container geometry, impurity content, how the beam interacts with confining surfaces and solution), laser characteristics (intensity, wavelength, polarization, type of laser: continuous or pulsed and pulse width), the time scale of exposure (ranging between femtoseconds in case of single pulse to series of pulses repeatedly exposing solutions as long as one hour[27]) and solution characteristics.

Interestingly, the effect of the solution volume exposed to the laser beam, a critical experimental parameter for industrial implementation of NPLIN, has been previously explored to a certain extent. Fang *et*

al. reported a significant volume dependence when comparing the nucleation rate of aqueous KCl in a test tube to that in a levitated microdroplet, where the ratio of irradiated volumes is as dramatic as 40 million times[31]. In addition, a study by Hua *et al.*[32] provides insights into a microfluidic laser-induced nucleation of supersaturated KCl solutions. This work outlines a continuous flow system for NPLIN where each volume element of the solution is subjected to laser pulses. The system allows for a varied irradiated volume by changing the flow time, and it has been shown that the number of crystals formed, was directly proportional to the laser intensity. In light of these studies, our current investigation builds on the existing knowledge to provide a comprehensive understanding of how varying the laser-exposed volume impacts the nucleation probability in millilitre scale volumes of supersaturated aqueous potassium chloride. The results were than analysed with dielectric polarization mechanism and classic nucleation theory. The effect of supersaturation and intensity have also been studied to determine their influence on the laser exposed volume dependency. Secondly, the position of laser irradiation with respect to air-solution interface (near the bottom of a cylindrical vial, in the bulk of the solution and near the air/liquid interface and directly at air/solution interface as illustrated in Figure 2.1) was studied to quantify how laser positioning alters nucleation probability.

2.2. EXPERIMENTAL

2.2.1. LASER EXPOSED VOLUME EXPERIMENTS

SOLUTION PREPARATION

Stock solutions were prepared by adding weighed amounts of ultrapure water (ELGA Purelab, UK, 18.2 MΩ cm) to potassium chloride (Sigma-Aldrich, molecular biology ≥ 99.0 % purity, CAS: 7447-40-7) in a flask corresponding to concentrations of 0.370 and 0.375 g_{KCl}/g_{H_2O}, which yielded solutions with supersaturations of 1.034 and 1.050 at a temperature of 24°C, respectively. The supersaturated solution was placed in an oven at 50°C overnight to ensure complete dissolution of the potassium chloride crystals. The solution flask was then transferred to a hot plate and stirred (50°C and 400 rpm) to be distributed to over one hundred 8 mL borosilicate HPLC vials (BGB, dimensions 61 × 16.6 mm). Each vial was filled with 7 mL solution using a bottle-top dispenser. All sample vials were stored in the oven operating at 50°C for at least one night before use. Before conducting the laser experiment, the hundred sample vials were than transferred from the oven to a thermostatic bath (Lauda Eco RE620) operating at 50°C and then subsequently cooled down overnight to 24°C. Furthermore, for every experiment, the samples were aged in a thermostatic bath set

to 24°C for a duration of 6 hours. It should be noted that the 6 hour ageing period commenced only once the bath temperature stabilized at 24°C, and this duration does not include any cooling time from higher temperatures.

LASER SETUP AND SAMPLE HANDLING

A schematic of the setup used in the laser exposed volume experiments is shown in Figure 2.1A.A Q-switched Nd:YAG laser (Continuum, Powerlite DLS8000) was used to generate 7 ns pulses of linearly polarized light at a wavelength of 532 nm and a frequency of 10 Hz. The direction of the generated light was changed by use of a mirror (NB1-K13, Thorlabs) or a beamsplitter (BSN10, Thorlabs) depending on the intensity requirements of the laser. The fundamental beam of 9 mm diameter was then passed through a Galilean telescope with lens configurations of different focal lengths to reduce or increase the laser beam diameter in order to enable the variation of laser exposed volume. An iris adjusted to a slightly bigger size than the beam diameter served as a filter for any artefacts produced by the laser. An overview of the mirrors, lenses and resulting beam diameters is given in Table 1.

Table 2.1.: Mirrors and lens configurations used in the laser exposed volume experiments. Laser exposed volume of vial containing aqueous potassium chloride solutions with $S = 1.034$ at 24 °C[a] . Position of lenses interchanged[b].

Mirror reflectance, [%]	Focal length plano-convex, f_a, $[mm]$	Focal length plano-concave, f_b, $[mm]$	Resulting beam diameter, $[mm]$	Resulting laser exposed volume[a], V_{laser}, $[cm^3]$
10	200	-50	2.3	0.047
10 or 100	150	-75	4.5	0.179
100	N/A	N/A	9.0	0.705
100	100	-75	12.0[b]	1.230
100	150	-100	13.5[b]	1.538

Prior to irradiating the samples, the average pulse energy of the laser beam was recorded by taking the average over 20 pulses using an energy meter (QE25LP-H-MB-QED-D0, Gentec EO). For experiments focussing on effect of exposed volume, the position of the light incident on the sample vial was chosen to be in the middle with respect to the bottom of the vial and the meniscus of the solution.

Care was taken to not induce nucleation by any mechanical shock and to keep the vials vertical at all times while transferring the solutions from the thermostatic bath to the setup during the experiment. One by one, the samples were moved from the bath, carefully dried with a fabric cloth and subsequently checked for crystal formation. If at this point, crystals were observed, the sample was omitted from the data set. If not, vials were exposed to a single laser pulse by varying the laser beam diameters (2.3 mm, 4.5 mm, 9 mm, 12 mm and 13.5 mm) at different laser intensities (10 MW/cm^2, 23 MW/cm^2). After laser irradiation, the

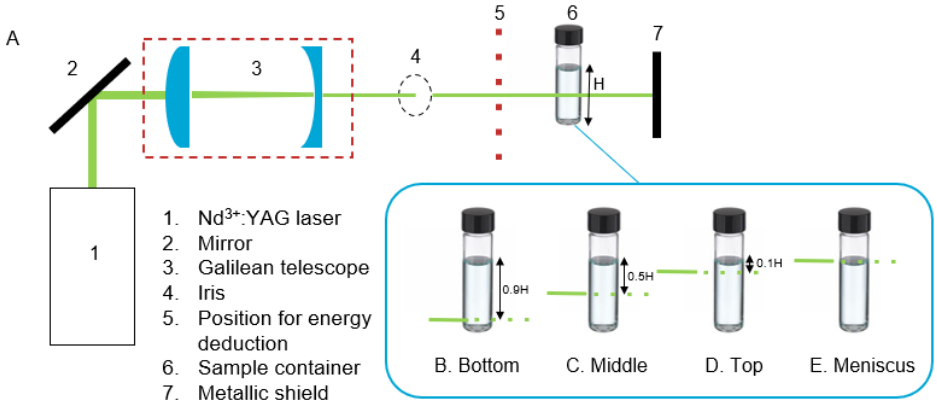

Figure 2.1.: Panel (A) shows the experimental setup used throughout the laser exposed volume experiments. The exposed volume is controlled by the Galilean telescope. The height of liquid in vial from air/solution interface to bottom of the vial is denoted as H. Panels (B) to (E) illustrate the different the irradiation locations, the location of exposed volume with respect to air-solution interface, at fixed laser intensity and supersaturation. The laser beam is illustrated as a green line.

sample was immediately moved back to the bath operating at 24°C. Vials were checked for crystals after 80 minutes. The observation time of 80 minutes were chosen considering previous literature[8], where a detection time of 60 minutes is reported to be sufficient for crystals to be detected by eye. The vials were carefully analysed and the number of nucleated samples was counted and the fraction of nucleated samples to the total number of samples irradiated was described as the nucleation probability $P(t_{obs} = 80\ \text{min})$.

2.2.2. LASER PULSE POSITION

A similar experimental approach was used to study the effect of the irradiation position on the nucleation probability of aqueous potassium chloride solutions. 100 vials of potassium chloride solutions (S = 1.034, 24 °C) were prepared as previously described. The position in which the laser pulse would reach the sample vials was adjusted by changing the height of the sample holder to four different positions with respect to distance from air/solution interface as illustrated in Figure 2.1b-e: (1) slightly above the glass/solution interface at the bottom of the vial. The distance from the air-solution interface is 0.9H where H is the height of liquid column ; (2) at the middle of the vial with respect to the air/solution interface (0.5H) ; (3) slightly below the air/solution

interface at the top of the vial (0.1H), and (4) through the meniscus of the solution. All samples were irradiated with a single pulse of the fundamental beam with a maximum peak intensity of 10 MW/cm^2, following the sample handling procedure.

2.3. RESULTS & DISCUSSIONS

2.3.1. EXPERIMENTAL REPEATABILITY & STATISTICAL ANALYSIS

In order to check the repeatability of the NPLIN experiments, the entire experimental procedure, from sample preparation to sample checking has been performed in triplicate. Samples containing aqueous potassium chloride solution with a supersaturation of S = 1.034 were irradiated in the middle of the vial with a maximum peak intensity of 10 MW/cm^2 and a beam diameter of 9 mm.

Figure 2.2 shows a bar plot containing the results in terms of nucleation probability per experiment. In total 39, 56 and 48 samples nucleated out of a set of 95, 99 and 97, respectively. This led to nucleation probabilities of 0.41, 0.57 and 0.49. The arithmetic mean of the three nucleation probabilities was calculated to be 0.49 with a standard deviation of 0.06, shown in Figure 2.2 with a black error bar.

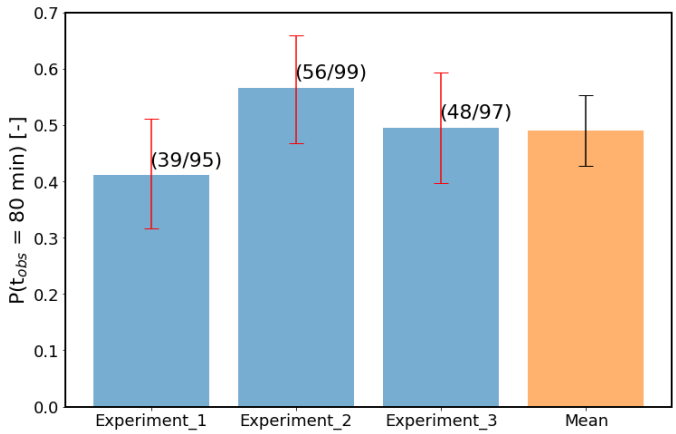

Figure 2.2.: Nucleation probability in three consecutive NPLIN experiments under identical laser parameters at fixed supersaturation of 1.034. The arithmetic mean of the three experiments is shown in orange. The number of nucleated samples and total number of samples are given next to error bars in parenthesis.

In light of the laborious nature of the current experimental procedure, performing every experiment in triplicate is very time consuming. Hence, throughout the rest of this study, the experimental error in NPLIN

experiments is approximated by calculating statistical (95%) confidence intervals using the Wilson's score method. Applying the Wilson's score method on the data obtained for the repeated experiments, it is found that the widths of the confidence intervals are 0.19, 0.19 and 0.20 for Experiment 1, 2 and 3, respectively (shown in Figure 2.2 as red error bars). Thus, the statistical error calculated from a single set of observations is found to be significantly larger than the experimental error computed from the outcome of repeated experiments (0.12, two times the standard deviation). Judging solely from the size of the errors computed by Wilson's score method, the nucleation probabilities observed in the repeated experiments in Figure 2.2 are statistically identical.

2.3.2. LASER EXPOSED VOLUME DEPENDENCY OF THE NUCLEATION PROBABILITY

The effect of laser exposed volume of the solution is studied by varying the laser beam diameter using a homemade Galilean telescope illustrated in Figure 2.1. Theoretical beam diameters have been obtained using the lens configurations given in Table 2.1. Using these values, the laser-exposed volume of the solution for each experiment has been derived assuming a refractive index of the sample[33] (see Appendix A section A.2[34]). The effects of changing the supersaturation at a constant maximum peak intensity of 10 MW/cm^2 is shown in Figure 2.3A. The effects of changing the maximum peak intensity at a constant supersaturation of 1.034 are shown in Figure 2.3B.

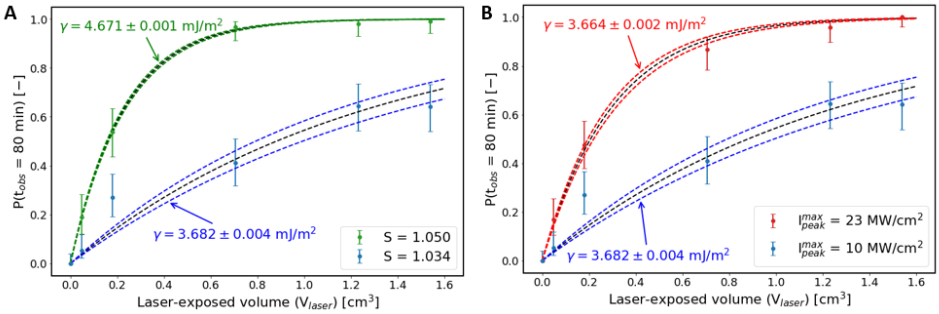

Figure 2.3.: The effect of laser exposed volume on the nucleation probability at (*A*) constant maximum peak intensity of 10 MW/cm^2 at two distinct supersaturation values, and at (B) constant supersaturation of 1.034 for two distinct peak intensities, respectively. Error bars are computed using the Wilson's score method. Fits have been constructed following the Dielectric Polarization model.

Several observations can be made from the data shown in Figure

2.3. First and foremost, by increasing the laser-exposed volume of the solution, an increase in nucleation probability is observed. To the best of our knowledge, this is the first report in literature identifying the exposed volume as an experimental parameter influencing NPLIN probability. Second, the extent to which the nucleation probability increases as an effect of the increasing laser exposed volume is influenced by both the degree of supersaturation of the solution and the magnitude of the maximum peak intensity of the laser.

To better understand these experimental observations, a mathematical basis was constructed using a modified Dielectric Polarization model. Under the constraints of constant intensity and supersaturation, the average number of crystals produced, $N_{crystal}$, is predicted to be proportional to the volume of the laser beam (V_{laser}), $N_{crystal} = m(I,S)V_{laser}$, where $m(I,S)$ serves as a intensity and supersaturation dependent lability constant given by

$$m(I,S) = \frac{3\rho_l W}{4\pi\rho_s} \times \frac{\int_{r_c(I)}^{r_c(0)} \exp\left[-\Delta G(r,0)/k_B T\right] dr}{\int_0^{r_c(0)} r^3 \exp\left[-\Delta G(r,0)/k_B T\right] dr} \tag{2.1}$$

where ρ_l is the density of the surrounding medium, W is the solute mass fraction, ρ_s is the density of the solute molecule, k_B is the Boltzmann constant, T is the temperature of the solution, S is the supersaturation ratio of the solution, $\Delta G_c(r,I)$ is the free energy barrier to form a cluster of radius r at laser intensity I, $r_c(0)$ is the critical cluster radius at zero laser intensity and $r_c(I)$ is the critical cluster radius at laser intensity I. The critical cluster radius $r_c(I)$ and free energy barrier $\Delta G_c(r,I)$ under the influence of an electric field is given by

$$r_c(I) = \frac{2\gamma}{\rho k_B T \ln S + aI} \tag{2.2}$$

$$\Delta G_c(I) = \frac{16\pi\gamma^3}{3(\rho k_B T \ln S + aI)^2} \tag{2.3}$$

where γ is the interfacial tension between the cluster and surrounding solution and the constant a contains the dielectric contrast between solute cluster and the surrounding medium [29] given by

$$a = \frac{3\epsilon_s(\epsilon_p - \epsilon_s)}{c(\epsilon_p + 2\epsilon_s)} \tag{2.4}$$

The NPLIN nucleation probability can then be computed as a function of lability constant (m) and laser exposed volume (V_{laser}) assuming a

Poisson distribution and is given by the equation 2.5.[23]. This model can be used to fit experimental data without having to correct for an experimental intensity threshold. The curves shown in Figure 2.3 are constructed by fitting the parameter $m(I,S)$ in equation 2.5 using non-linear least squares regression. The only parameter that is not estimated in this analysis is the interfacial tension between the cluster surface and the surrounding medium or γ, which is present as a function of r_c in the limits of the integrals in equation 2.1. Hence, by numerically solving equation 2.1, a phenomenological value for the interfacial tension can be derived. An overview of the physical parameters used for the calculations is shown in Table 2.2. The values for the dielectric constant of a cluster of solute molecules, ϵ_p, and of the surrounding medium, ϵ_s, have been computed by squaring the refractive indices of solid potassium chloride (n_{KCl} = 1.4940 [35]) and the sample solution, respectively [36]. The complete derivation of the laser exposed volume dependency on nucleation probability using modified DP model is shown in the Appendix A section A.1[34]

$$P(t_{obs}) = 1 - \exp[-m(I,S)V_{laser}] \tag{2.5}$$

Table 2.2.: Physical parameters used to derive the phenomenological value of the interfacial tension. Parameters are assumed to be properly estimated at a temperature of 24 °C.

Supersaturation, S, [-]	Solute mass fraction, W, [-]	Solid density, ρ_s, [kg/m^3]	Solution density, ρ_l, [kg/m^3]	Solution refractive index, n_3, [-]	Rel. permittivity solid, ϵ_p, [-]	Rel. permittivity solution, ϵ_s, [-]	Molar mass, M, [g/mol]
1.034	0.2698	1984	1184	1.3758	2.232	1.893	74.55
1.050	0.2729	1984	1184	1.3763	2.232	1.894	74.55

Table 2.3 shows an overview of the parameters derived from the Dielectric Polarization model and the numerical values computed by applying the best-fit value for the interfacial tension to the Classic Nucleation Theory. Observing both plots in Figure 2.3, it was found that in case of increasing supersaturation or higher maximum peak intensity, the samples become more labile to nucleation hence shows a higher lability constant.

From the fitted lability constants, phenomenological values for the interfacial tension are computed. Asymmetrical errors are calculated due to the non-linear relation between the lability constant and the interfacial tension. The absolute values of the interfacial tension observed are of the same order of magnitude compared to values derived from previous intensity-dependent NPLIN experiments conducted on similar aqueous potassium chloride systems by Alexander *et al.* [23] (γ = 2.19 mJ/m^2), Ward *et al.* [37] (γ = 5.283 mJ/m^2) and Fang *et al.* [38] (γ = 3.16 mJ/m^2).

Even though the Dielectric Polarization model can be employed to yield quantitative information from the current NPLIN experiments, using

Table 2.3.: Derived parameters using the Dielectric Polarization model. In addition the parameters computed by applying the value for the interfacial tension to the Classical Nucleation Theory are also shown.

Supersaturation, S, [-]	Max. peak intensity, I^{max}_{peak}, $[MW/cm^2]$	Lability constant, $m(I,S)$, $[cm^{-3}]$	Interfacial tension, γ, $[mJ/m^2]$	Nucleation barrier height, $\Delta G_c(0)/k_bT$, [-]	Critical radius, $r_c(0)$, $[nm]$	Dielectric free energy, $\Delta G_{EF}/k_BT$, [-]	Difference in critical radii, $r_c(0)-r_c(I)$, $[nm]$
1.034	10	0.787 (± 0.088)	3.674 (+ 0.004) (- 0.003)	41.9	3.34	$-4.07\cdot10^{-3}$	$1.62\cdot10^{-4}$
1.034	23	3.352 (± 0.202)	3.656 (+ 0.002) (- 0.002)	41.2	3.33	$-9.22\cdot10^{-3}$	$3.71\cdot10^{-4}$
1.050	10	4.367 (± 0.114)	4.660 (+ 0.001) (- 0.001)	40.2	2.91	$-2.66\cdot10^{-3}$	$0.96\cdot10^{-4}$

the fitted value of the interfacial tension to compute absolute values of nucleation barrier height and critical radius from the Classical Nucleation Theory reveals ambiguous results. For all the conducted experiments, a classical nucleation barrier of $\Delta G_c(0)$ = 40 - 42 k_BT with a critical radius of r_c = 2.91 - 3.34 nm has been calculated. According to these calculations, in combination with the electric field strength of the laser, the classical nucleation barrier is only lowered by a minuscule amount (ΔG_{EF} = $-9.22\cdot10^{-3}$ k_BT to $-2.66\cdot10^{-3}$ k_BT). Hence, the resulting decrease in critical radius is of the order 10^{-4} nm for all three experiments. These results indicate that while the Dielectric Polarization model in other NPLIN experiments provided useful information [8, 10], the effect of the laser electric field on the nucleation process is relatively small.

If the nucleation rate, J, is expressed in the form of an Arrhenius equation [39],

$$J = A \exp[-\Delta G_c / k_B T] \tag{2.6}$$

where A is the pre-exponential factor assumed to be constant for spontaneous and laser-induced nucleation experiments, then the nucleation rate from laser-induced experiments, J_{laser}, should relate to the spontaneous nucleation rate, $J_{spontaneous}$, by

$$\begin{aligned} \frac{J_{spontaneous}}{J_{laser}} &= \frac{\exp[-\Delta G_c(0)/k_BT]}{\exp[-(\Delta G_c(I))/k_BT]} \\ &= \exp[-\Delta G_{EF}/k_BT] \end{aligned} \tag{2.7}$$

where ΔG_{EF} is the change in free energy due to the introduction of an electric field ($\Delta G_{EF} = v\alpha I$). Here v is the volume of the precritical cluster. Hence, by substituting the values for (ΔG_{EF} = $-9.22\cdot10^{-3}$ k_BT to $-2.66\cdot10^{-3}$ k_BT) found in this study, the laser-induced nucleation rate should increase by a factor of 1.003 to 1.009 compared to the spontaneous nucleation rate.

However according to Classical Nucleation theory[39], the nucleation rate (J) is inversely proportional to the induction time (t_{ind})[39]. Thus, laser-induced nucleation should increase at least a hundred-fold compared to spontaneous nucleation under similar experimental

conditions. Consistent with this theory, spontaneous nucleation of aqueous potassium chloride solutions typically takes 1-2 weeks under such conditions. However, Kacker *et al.*[40] have shown that nucleation can occur within 80 minutes in laser-induced experiments, indicating a significant increase in the nucleation rate. Unless laser irradiation of the samples plays a significant role in the value of the pre-exponential factor, the massive decrease in nucleation time can not be explained quantitatively in the context of the Dielectric Polarization model and thus highlights the limitations of the current approach. Ward *et al.* [37] explained similar ambiguous results by introducing the Two-Step Nucleation model. It was argued that the low electric field strength might play a significant role in structurally reorganizing the amorphous liquid-like clusters, lowering the second nucleation barrier and hence accounting for the observations made from NPLIN experiments [37]. However, quantitative evidence to substantiate such a claim proved challenging to obtain. We acknowledge that the proposed two-step nucleation explanation may also be valid for our observations. However, providing supporting experimental evidence is beyond the scope of the current work.

Alternatively, the experimental findings could be explained qualitatively through the nanoparticle heating mechanism. By increasing the laser beam diameter, a larger volume of the solution is irradiated. If it is assumed that the nanoparticles are homogeneously suspended throughout the sample volume, it inevitably means that the number of nanoparticles irradiated increases with increasing beam diameters. This, in turn, would lead to an increased number of vapour cavities and more locally increased supersaturations, from which an increase in the nucleation probability would be expected. The increase in supersaturation of the solution would lead to higher locally supersaturated regions upon laser irradiation with similar conditions, resulting in a higher nucleation probability. Likewise, increased intensity is expected to create larger vapour cavities due to more extensive heating of the nanoparticles. This, again, would result in higher locally supersaturated regions and subsequently increase the probability of nucleation. Although the nanoparticle heating mechanism provides the basic qualitative explanation for the current experimental observations, further research in the direction of various nano-impurity size distributions and impurity compositions could provide a more in-depth understanding of this mechanism through experiments.

2.3.3. CRYSTAL MORPHOLOGY AND NUMBER OF CRYSTALS PER NUCLEATED SAMPLE

In addition to studying the number of samples nucleated in an effort to relate the nucleation probability to the laser exposed volume of the

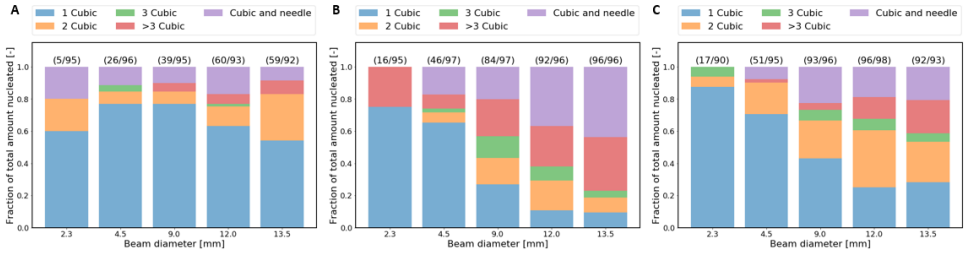

Figure 2.4.: Bar plots showing the relative number of crystals per nucleated sample in experiments on aqueous potassium chloride solutions under distinct supersaturation,S, and maximum laser peak intensity,I_{peak}^{max}. Panel (*A*) S = 1.034 and I_{peak}^{max} = 10 MW/cm^2, Panel (*B*) S = 1.050 and I_{peak}^{max} = 10 MW/cm^2, and Panel (*C*) S = 1.034 and I_{peak}^{max} = 23 MW/cm^2. The number of samples nucleated and the total number of samples irradiated per experiment are shown in parentheses above the corresponding bar.

solution, the number of crystals and type of crystal morphology per experiment is reported in this study. Figure 2.4 shows the distribution of the number of crystals and crystal geometries per nucleated sample for each laser exposed volume experiment.

In general, the following observations can be made from the Figure 2.4. The combination of a low supersaturation (S = 1.034) and a low maximum peak intensity (I_{peak}^{max} = 10 MW/cm^2) resulted in predominantly single cubic crystals for each of the beam diameters (see Figure 2.4A). Some accounts of two cubic crystals per nucleated sample have been observed as well as the combination of cubic and needle-like crystals. However, no clear relationship between amount of crystals per sample and the laser beam diameter is found. Increasing the supersaturation of the aqueous potassium chloride solutions revealed a general increase in multiple crystals nucleated per irradiated/nucleated sample the more the beam diameter is increased (see Figure 2.4B). The same effect is observed by increasing the maximum peak intensity (see Figure 2.4C), in accordance with previous reported experiments on aqueous potassium chloride solutions under similar conditions [23, 37, 40]. Apart from observing a relation between number of crystals per nucleated sample by increasing the maximum peak intensity of the laser, the use of large beam diameters in combination with high maximum peak intensities clearly favors the formation of large number of cubic crystals (≥3 cubic) or mixtures of cubic and needle shaped crystals.

Increasing the laser beam diameter and maximum peak intensity or bulk supersaturation can lead to the formation of more nucleation sites as a larger area of the solution is exposed to the laser beam. This

can result in the formation of multiple cubes or a mixture of cubes and needles due to the increased number of nucleation sites and less solute available for each nucleus[41].

2.3.4. EFFECT OF IRRADIATION POSITION ON NPLIN PROBABILITY

The experimental configuration in experiments addressing the effect of irradiation position is shown in Figure 2.5B-E. No significant change in nucleation probability is observed when the unfocused incident laser beam passed through close to the bottom, top, or through the middle of the cylindrical vial, respectively. In contrast, laser irradiation through the meniscus of the solution yielded an increase in nucleation probability by approximately 40 - 50%.

At the bottom, middle, and top positions, there is no change in the solution's refractive index or change in the geometry of the sample container. Hence, the laser beam is expected to act identically on the solution volume. By assuming a homogeneous distribution of precritical clusters and considering that the laser-exposed volume is the same for the bottom, middle, and top positions, no significant change in nucleation probability is expected according to the Dielectric Polarization model. The observations of the position-dependent experiments can also be explained similarly in the context of the Nanoparticle Heating mechanism. Again, taking into account that the laser acts identically on the solution volume for the bottom, middle and top positions, and by assuming a homogeneous distribution of nanoparticles/nanoimpurities throughout the sample volume, no change in nucleation probability is expected.

In an attempt to better understand the nucleation probability results and the laser focusing effect at the meniscus, a ray tracing simulation using Zemax optic studio (v.23.2.01) was used, since analytical estimates proved challenging. Geometries were created with dimensions identical to those of an HPLC vial (BGB, dimensions 61 $\times$ 16.6 mm) using the CAD functionality tool. Glass, aqueous KCl solution, and air, with individual refractive indices of 1.5, 1.4940 and 1 respectively, were assigned as materials within the vial to carry out the simulation. To understand how light rays operate when interacting with the meniscus in our system, the concept of total internal reflection becomes important. Governed by Snell's law, the total internal reflection occurs when a light ray, traversing a medium of a higher refractive index, meets a boundary of a medium with a lower refractive index at an angle greater than the critical one, resulting in the ray reflecting back. In this context, the critical angle is approximately 42°, derived from ϕ = arcsin (1/1.494), as light rays travel from the solution medium to the air medium at the meniscus. Given the concave nature of the meniscus and the collimated nature of the incident laser beam imply that most rays reach the

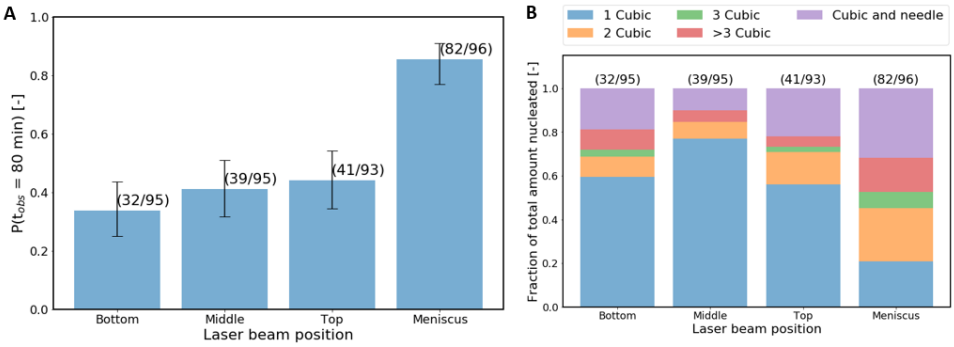

Figure 2.5.: Bar plots showing the nucleation probability for different positions of the laser beam with respect to the interfaces within the glass vials. Experiments are performed on aqueous potassium chloride (S = 1.034) using a maximum peak intensity of 10 MW/cm^2. Error bars are computed using the Wilson's score method. The number of samples nucleated and the total number of samples irradiated per experiment are shown in parentheses above the corresponding bar.

air/solution boundary at an angle larger than this critical value, resulting in downward reflection (total internal reflection) of the light rays as can be seen in the Appendix A Figures SVA (side view) & SVB (top view). As the Gaussian laser beam (9 mm diameter) with a peak intensity of 5 MW/cm^2 irradiates the supersaturated solution horizontally, the HPLC vial acts analogously to a cylindrical lens, focusing the beam behind it. Meanwhile the concave meniscus of the solution and the rear wall of the vial reflect the incoming light rays into solution medium following total internal reflection. The overlap of these two optical phenomena leads to a significant accumulation of laser peak intensity just below the meniscus. At this stage, to acquire a comprehensive understanding of the laser intensity distribution beneath the meniscus in simulations, a volume detector was placed directly below it with bottom region of the meniscus encompassed (orange color rectangle) within the detecting volume. The volume detector was positioned based on the location of crystal formation observed experimentally on the meniscus following the laser shot. The intensity distribution was than visualized using 2D slices from the 3D volumetric detector. Specific visual representations across the XY and YZ planes, along with the associated laser peak intensity at one such particular coordinate as an example, are detailed in the Appendix A Figures SVC & SVD.

Possible scenarios that could explain the increased nucleation probability at the meniscus, within the context of the Dielectric Polarization model, include (1) preferential adsorption of the solute onto the air-solution surface, suggesting a higher number of critical clusters at

the interface, and (2) the observed intricate refraction of the laser beam due to the complex vial geometry and meniscus curvature creating areas with higher laser intensities at the meniscus, thereby lowering the nucleation barrier by a greater amount, and thus changing the outcome of the laser-induced nucleation experiments compared to the other irradiation positions. Similarly, from the perspective of the Nanoparticle Heating mechanism, an increase in peak intensity at the meniscus could lead to more intense light absorption by nanoparticles/nanoimpurities at the air/solution interface, altering the vapor cavity radius and enhancing supersaturation.

From the perspective of Nanoparticle Heating mechanism, an additional scenario arises. At the air-solution interface, dust particles may adhere and hence locally increase the 'impurity' concentration, which has shown to have an increasing effect on the nucleation probability in NPLIN experiments [26, 27, 42].

Previous reports explaining the increase of nucleation probability at the air/solution interface have been provided in the literature. Ikni *et al.* [16] and Liu *et al.*[43] observed an increase in crystallization probability at air/solution interface with respect to carbamazepine and glycine supersaturated solutions irradiated with femtosecond laser and nanosecond laser respectively. The authors attributed this observation to the interplay between molecular adsorption and surface deformation, resulting in a distinct solution flow from the surface due to its free boundary characteristic. This unique flow resulting in surface deformation might contribute to enhancing crystallization probability at the air/solution (meniscus) interface. Similarly, Clair *et al.*[44] observed that glycine crystals obtained through NPLIN nucleate at the meniscus and exhibit different morphologies, even when the laser was directed through the air/solution interface from above.

Figure 2.5B gives an overview of the relative amounts of crystals (or crystal morphology) per nucleated sample in the position experiments. The bottom, middle and top experiments show a dominance in single crystals per nucleated sample and no clear distinction in crystal number or morphology could be observed. In contrast to this, the experiments in which the meniscus of the solution was irradiated, a significant increase in multiple crystals observed per sample, as well as an increase in the combination of cubic and needle-like geometries was observed. This supports the presence of multiple nucleation sites at the meniscus, either caused by an increase in generated supersaturation due to irradiation [45], multiple peak intensity hot spots or from dust adhesion to the surface leading to heterogeneous nucleation. A similar increase in number of crystals for KCl supersaturated solutions with an increase in the laser peak intensity was also observed in the literature[46, 47]. Hua *et al.*[47] studied microfluidic laser-induced nucleation in supersaturated KCl solutions ranging from 1.06 to 1.10 and observed that number

of crystals formed in the microfluidic device was proportional to the laser intensity. Meanwhile, Duffus et al.[46] observed crystal nucleation behavior in KCl-agarose gels prepared using 0.12-0.75% w/w powdered agarose in 1.06 supersaturated KCl solutions. Their findings also indicated a direct relationship between laser peak intensity and crystal formation.

2.4. CONCLUSIONS

This study focused on how NPLIN probability of supersaturated aqueous potassium chloride solutions is influenced by laser-exposed volume and laser position. Despite their significance in industrial scale implementation of NPLIN, these topics have not been extensively discussed in the NPLIN literature, if at all.

The NPLIN probability was found to depend on the laser-exposed volume under the constraints of constant supersaturation and peak intensity. Also, an increase in the number of crystals per nucleated sample was observed by enlarging the laser-exposed volume. Both the Nanoparticle Heating and the Dielectric Polarization model can partly explain these observations. However, in absence of data that exclusively favors one of the models, we cannot definitively conclude which which mechanism is dominant in presented experiments. Further experiments exploring the effects of different nanoparticles (size, concentration) on nucleation probability could provide valuable insights into the underlying mechanisms of NPLIN.

Regarding the effect of laser position, irradiation away from interfaces or in the vicinity of the air/solution or glass/solution interface yielded no change in nucleation probability. Only irradiation through the air/solution interface (meniscus), a significant increase in nucleation probability was observed. This observation was accompanied by an increase in number of crystals observed per sample along with an increase in cubic and needle-like geometries observed. This is attributed to preferential adsorption at interface, increased laser peak intensity at the meniscus caused by complex laser refraction, or laser induced heating of dust/impurity particles adhered at the interface resulting in evaporation. The presented results will contribute to the rational design of potential industrial applications of NPLIN, where controlling crystal quality parameters, such as morphology, is of paramount importance [48, 49].

BIBLIOGRAPHY

[1] J. Garside and R. J. Davey. *From molecules to crystallizers*. Oxford UK, 2001.

[2] D. Chakraborty and G. N. Patey. "How crystals nucleate and grow in aqueous NaCl solution". In: *Journal of Physical Chemistry Letters* 4.4 (2013), pp. 573–578. issn: 1948-7185. doi: 10.1021/jz302065w. url: https://doi.org/10.1021/jz302065w.

[3] J. F. Lutsko and J. Lam. "Classical density functional theory, unconstrained crystallization, and polymorphic behavior". In: *Physical Review E* 98.1 (2018). issn: 24700053. doi: 10.1103/PhysRevE.98.012604. arXiv: 1805.05673.

[4] P. G. Vekilov. "Nucleation of protein crystals". In: *Progress in Crystal Growth and Characterization of Materials* 62.2 (June 2016), pp. 136–154. issn: 0960-8974. doi: 10.1016/J.PCRYSGROW.2016.04.007. url: https://www.sciencedirect.com/science/article/pii/S0960897416300109.

[5] A. J. Alexander and P. J. Camp. "Non-photochemical laser-induced nucleation". In: *Journal of Chemical Physics* 150.4 (2019). issn: 00219606. doi: 10.1063/1.5079328. url: http://dx.doi.org/10.1063/1.5079328.

[6] T. Nakamuro, M. Sakakibara, H. Nada, K. Harano, and E. Nakamura. "Capturing the Moment of Emergence of Crystal Nucleus from Disorder". In: *Journal of the American Chemical Society* 143.4 (2021), pp. 1763–1767. issn: 15205126. doi: 10.1021/jacs.0c12100.

[7] V. Korede, N. Nagalingam, F. M. Penha, N. van der Linden, J. T. Padding, R. Hartkamp, and H. B. Eral. "A Review of Laser-Induced Crystallization from Solution". In: *Crystal Growth & Design* 23.5 (Apr. 2023), pp. 3873–3916. doi: 10.1021/acs.cgd.2c01526.

[8] R. Kacker, S. Dhingra, D. Irimia, M. K. Ghatkesar, A. Stankiewicz, H. J. Kramer, and H. B. Eral. "Multiparameter Investigation of Laser-Induced Nucleation of Supersaturated Aqueous KCl Solutions". In: *Crystal Growth and Design* 18.1 (2018), pp. 312–317. issn: 15287505. doi: 10.1021/acs.cgd.7b01277.

[9] M. R. Ward, I. Ballingall, M. L. Costen, K. G. McKendrick, and A. J. Alexander. “Nanosecond pulse width dependence of non-photochemical laser-induced nucleation of potassium chloride”. In: *Chemical Physics Letters* 481.1-3 (2009), pp. 25–28. issn: 00092614. doi: 10.1016/j.cplett.2009.09.049. url: http://dx.doi.org/10.1016/j.cplett.2009.09.049.

[10] M. R. Ward, S. McHugh, and A. J. Alexander. “Non-photochemical laser-induced nucleation of supercooled glacial acetic acid”. In: *Physical Chemistry Chemical Physics* 14.1 (2012), pp. 90–93. issn: 14639076. doi: 10.1039/c1cp22774b.

[11] J. Zaccaro, J. Matic, A. S. Myerson, and B. A. Garetz. “Non-photochemical, laser-induced nucleation of supersaturated aqueous glycine produces unexpected γ-polymorph”. In: *Crystal Growth and Design* 1.1 (2001), pp. 5–8. issn: 15287483. doi: 10.1021/cg0055171.

[12] B. A. Garetz, J. Matic, and A. S. Myerson. “Polarization Switching of Crystal Structure in the Nonphotochemical Light-Induced Nucleation of Supersaturated Aqueous Glycine Solutions”. In: *Physical Review Letters* 89.17 (2002), p. 175501. url: https://link.aps.org/doi/10.1103/PhysRevLett.89.175501.

[13] J. Matic, X. Sun, B. a. Garetz, and a. S. Myerson. “Intensity, Wavelength, and Polarization Dependence of Nonphotochemical Laser-Induced Nucleation in Supersaturated Aqueous Urea Solutions”. In: *Crystal Growth & Design* 5 (2005), pp. 1565–1567. doi: 10.1021/cg050041c.

[14] X. Sun, B. A. Garetz, and A. S. Myerson. “in the Nonphotochemical Laser-Induced Nucleation (NPLIN) of 2006”. In: *Crystal Growth & Design* 6.3 (2006), p. 684.

[15] X. Sun, B. A. Garetz, and A. S. Myerson. “Polarization switching of crystal structure in the nonphotochemical laser-induced nucleation of supersaturated aqueous l-histidine”. In: *Crystal Growth & Design* 8.5 (2008), pp. 1720–1722. issn: 15287483. doi: 10.1021/cg800028v.

[16] A. Ikni, B. Clair, P. Scouflaire, S. Veesler, J.-M. Gillet, N. El Hassan, F. Dumas, and A. Spasojević-de Biré. “Experimental Demonstration of the Carbamazepine Crystallization from Non-photochemical Laser-Induced Nucleation in Acetonitrile and Methanol”. In: *Crystal Growth & Design* 14.7 (2014), pp. 3286–3299. issn: 1528-7483. doi: 10.1021/cg500163c. url: http://dx.doi.org/10.1021/cg500163c.

[17] I. S. Lee, K. T. Kim, A. Y. Lee, and A. S. Myerson. “Concomitant Crystallization of Glycine on Patterned Substrates: The Effect of pH on the Polymorphic Outcome”. In: *Crystal Growth & Design* 8.1 (Jan. 2008), pp. 108–113. issn: 1528-7505. doi: 10.1021/cg700890m.

[18] N. Yennawar, S. Denev, V. Gopalan, and H. Yennawar. “Laser-improved protein crystallization screening”. In: *Acta Crystallographica Section F* 66.8 (Aug. 2010), pp. 969–972. doi: 10.1107/S1744309110023857. url: https://doi.org/10.1107/S1744309110023857.

[19] X. Sun, B. A. Garetz, M. F. Moreira, and P. Palffy-Muhoray. “Nonphotochemical laser-induced nucleation of nematic phase and alignment of nematic director from a supercooled thermotropic liquid crystal”. In: *Phys. Rev. E* 79 (2 Feb. 2009), p. 021701. doi: 10.1103/PhysRevE.79.021701. url: https://link.aps.org/doi/10.1103/PhysRevE.79.021701.

[20] M. R. Ward, W. J. Jamieson, C. A. Leckey, and A. J. Alexander. “Laser-induced nucleation of carbon dioxide bubbles”. In: *Journal of Chemical Physics* 142.14 (2015). issn: 00219606. doi: 10.1063/1.4917022. url: http://dx.doi.org/10.1063/1.4917022.

[21] B. C. Knott, J. L. Larue, A. M. Wodtke, M. F. Doherty, and B. Peters. “Communication: Bubbles, crystals, and laser-induced nucleation”. In: *Journal of Chemical Physics* 134.17 (2011). issn: 00219606. doi: 10.1063/1.3582897.

[22] Y. Liu, M. H. Van Den Berg, and A. J. Alexander. “Supersaturation dependence of glycine polymorphism using laser-induced nucleation, sonocrystallization and nucleation by mechanical shock”. In: *Physical Chemistry Chemical Physics* 19.29 (2017), pp. 19386–19392. issn: 14639076. doi: 10.1039/c7cp03146g.

[23] A. J. Alexander and P. J. Camp. “Single Pulse, Single Crystal Laser-Induced Nucleation of Potassium Chloride”. In: *Crystal Growth & Design* 9.2 (2009), pp. 958–963. doi: https://doi.org/10.1021/cg8007415.

[24] C. Duffus, P. J. Camp, and A. J. Alexander. “Spatial control of crystal nucleation in agarose gel”. In: *Journal of the American Chemical Society* 131.33 (2009), pp. 11676–11677. issn: 00027863. doi: 10.1021/ja905232m.

[25] T. Hua, C. Valentín-Valentín, O. Gowayed, S. Lee, B. A. Garetz, and R. L. Hartman. “Microfluidic Laser-Induced Nucleation of Supersaturated Aqueous Glycine Solutions”. In: *Crystal Growth & Design* 20.10 (Oct. 2020), pp. 6502–6509. issn: 1528-7483. doi:

10.1021/acs.cgd.0c00669. url: https://doi.org/10.1021/acs.cgd.0c00669.

[26] N. Javid, T. Kendall, I. S. Burns, and J. Sefcik. “Filtration Suppresses Laser-Induced Nucleation of Glycine in Aqueous Solutions”. In: *Crystal Growth & Design* 16.8 (July 2016), pp. 4196–4202. doi: 10.1021/acs.cgd.6b00046.

[27] M. R. Ward, A. M. Mackenzie, and A. J. Alexander. “Role of Impurity Nanoparticles in Laser-Induced Nucleation of Ammonium Chloride”. In: *Crystal Growth & Design* 16.12 (Dec. 2016), pp. 6790–6796. issn: 1528-7483. doi: 10.1021/acs.cgd.6b00882. url: https://doi.org/10.1021/acs.cgd.6b00882.

[28] B. A. Garetz, J. E. Aber, N. L. Goddard, R. G. Young, and A. S. Myerson. “Nonphotochemical, Polarization-Dependent, Laser-Induced Nucleation in Supersaturated Aqueous Urea Solutions”. In: *Physical Review Letters* 77.16 (1996), pp. 3475–3476. url: https://link.aps.org/doi/10.1103/PhysRevLett.77.3475.

[29] M. Nardone and V. G. Karpov. “A phenomenological theory of nonphotochemical laser induced nucleation”. In: *Phys. Chem. Chem. Phys.* 14.39 (2012), pp. 13601–13611. doi: 10.1039/C2CP41880K. url: http://dx.doi.org/10.1039/C2CP41880K.

[30] D. Irimia, J. Jose Shirley, A. S. Garg, D. P. Nijland, A. E. Van Der Heijden, H. J. Kramer, and H. B. Eral. “Influence of Laser Parameters and Experimental Conditions on Nonphotochemical Laser-Induced Nucleation of Glycine Polymorphs”. In: *Crystal Growth and Design* 21.1 (2021), pp. 631–641. issn: 15287505. doi: 10.1021/acs.cgd.0c01415.

[31] K. Fang, S. Arnold, and B. A. Garetz. “Nonphotochemical Laser-Induced Nucleation in Levitated Supersaturated Aqueous Potassium Chloride Microdroplets”. In: *Crystal Growth & Design* 14.5 (2014), pp. 2685–2688. doi: https://doi.org/10.1021/cg5004319.

[32] T. Hua, O. Gowayed, D. Grey-Stewart, B. A. Garetz, and R. L. Hartman. “Microfluidic Laser-Induced Nucleation of Supersaturated Aqueous KCl Solutions”. In: *Crystal Growth & Design* 19.6 (2019), pp. 3491–3497. doi: https://doi.org/10.1021/acs.cgd.9b00362.

[33] C. Tan and Y. Huang. “Dependence of refractive index on concentration and temperature in electrolyte solution, polar solution, nonpolar solution, and protein solution”. In: *Journal of Chemical & Engineering Data* 60.10 (2015), pp. 2827–2833. issn: 0021-9568.

[34] See Supplementary Information at [URL will be inserted by publisher] for hydrophobization protocol, droplet characterization results, estimation of cooling length and other miscellaneous details. 2023.

[35] [Online; accessed 04-05-2022]. 2022. url: https://refractiveindex.info/?shelf=main$%5C&$book=KCl$%5C&$page=Li.

[36] P. Atkins, J. d. Paula, and J. Keeler. *Atkins' physical chemistry*. Oxford University Press, 2018, p. 667.

[37] M. R. Ward and A. J. Alexander. "Nonphotochemical laser-induced nucleation of potassium halides: Effects of wavelength and temperature". In: *Crystal Growth and Design* 12.9 (2012), pp. 4554–4561. issn: 1528-7483. doi: 10.1021/cg300750c.

[38] K. Fang, S. Arnold, and B. A. Garetz. "Nonphotochemical Laser-Induced Nucleation in Levitated Supersaturated Aqueous Potassium Chloride Microdroplets". In: *Crystal Growth & Design* 14.5 (2014), pp. 2685–2688. issn: 1528-7483. doi: 10.1021/cg5004319.

[39] J. W. Mullin. *Crystallization*. Butterworth-Heinemann, 2004.

[40] R. Kacker, S. Dhingra, D. Irimia, M. K. Ghatkesar, A. I. Stankiewicz, H. J. M. Kramer, and H. B. Eral. "Multiparameter Investigation of laser-induced nucleation of supersaturated aqueous KCl solutions". In: *Crystal Growth & Design* 18.1 (2018). issn: 1528-7483. doi: 10.1021/acs.cgd.7b01277.

[41] J. Kardum, A. Sander, and A. Glasnoviae. "Batch Crystallization of KCl: the Influence of the Cooling and Mixing Rate on the Granulometric Properties of Obtained Crystals". In: *Chemical and Biochemical Engineering Quarterly* 19 (Mar. 2005).

[42] K. L. Mittal and R. Jaiswal. *Particle adhesion and removal*. Scrivener Publishing, 2015.

[43] T.-H. Liu, T. Uwada, T. Sugiyama, A. Usman, Y. Hosokawa, H. Masuhara, T.-W. Chiang, and C.-J. Chen. "Single femtosecond laser pulse-single crystal formation of glycine at the solution surface". In: *Journal of Crystal Growth* 366 (Mar. 2013), pp. 101–106. doi: 10.1016/j.jcrysgro.2012.11.018.

[44] B. Clair, A. Ikni, W. Li, P. Scouflaire, V. Quemener, and A. Spasojevic-de Bire. "A new experimental setup for high-throughput controlled non-photochemical laser-induced nucleation: application to glycine crystallization". In: *Journal of Applied Crystallography* 47 (2014), pp. 1252–1260. doi: https://doi.org/10.1107/S160057671401098X.

[45] N. Nagalingam, A. Raghunathan, V. Korede, C. Poelma, C. S. Smith, R. Hartkamp, J. T. Padding, and H. B. Eral. “Laser-Induced Cavitation for Controlling Crystallization from Solution”. In: *Physical Review Letters* 131.12 (Sept. 2023). issn: 1079-7114. doi: 10.1103/physrevlett.131.124001.

[46] C. Duffus, P. J. Camp, and A. J. Alexander. “Spatial control of crystal nucleation in agarose gel”. In: *Journal of the American Chemical Society* 131.33 (2009), pp. 11676–11677. issn: 00027863. doi: 10.1021/ja905232m.

[47] T. Hua, O. Gowayed, D. Grey-Stewart, B. A. Garetz, and R. L. Hartman. “Microfluidic Laser-Induced Nucleation of Supersaturated Aqueous KCl Solutions”. In: *Crystal Growth $&Design* 19.6 (2019), pp. 3491–3497. doi: 10.1021/acs.cgd.9b00362.

[48] A. S. Myerson, D. Erdemir, and A. Y. Lee, eds. *Handbook of Industrial Crystallization*. Cambridge University Press, June 2019. doi: 10.1017/9781139026949.

[49] A. B. de Haan, H. B. Eral, and B. Schuur. *Industrial Separation Processes*. De Gruyter, July 2020. doi: 10.1515/9783110654806.

3

DESIGN AND VALIDATION OF A DROPLET-BASED MICROFLUIDIC SYSTEM TO STUDY NON-PHOTOCHEMICAL LASER-INDUCED NUCLEATION OF POTASSIUM CHLORIDE SOLUTIONS

Non-Photochemical Laser-Induced Nucleation (NPLIN) emerged as a promising primary nucleation control technique offering spatio-temporal control over crystallization with potential for polymorph control. So far, NPLIN was mostly investigated in millilitres vials, through laborious manual counting of the crystallized vials by visual inspection. Microfluidics represents an alternative to acquiring automated and statistically reliable data. Thus, we designed a droplet-based microfluidic platform capable of identifying the droplets with crystals emerging upon Nd:YAG laser irradiation using the deep learning method. In our experiments, we used supersaturated solutions of KCl in water and the effect of laser intensity, wavelength (1064 nm, 532 nm, 355 nm), solution supersaturation (S), solution filtration and intentional doping with nanoparticles on the nucleation probability is quantified and compared to control cooling crystallization experiments. Ability of dielectric polarization and the nanoparticle heating mechanisms proposed for NPLIN to explain the acquired results is tested. Solutions with lower supersaturation (S=1.05) exhibit significantly higher NPLIN probabilities than those in the control experiments for all laser wavelengths above a threshold intensity (50 MW/cm^2). At higher

This chapter is based on Vikram Korede, Frederico Marques Penha, Vincent de Munck, Lotte Stam, Thomas Dubbelman, Nagaraj Nagalingam, Maheswari Gutta, PingPing Cui, Daniel Irimia, Antoine E.D.M. van der Heijden, Herman J.M. Kramer, and Hüseyin Burak Eral, Crystal Growth & Design, 2023, 23(8), 6067-6080

supersaturation studied (S=1.10), irradiation was already effective at lower laser intensities (10 MW/cm^2). No significant wavelength effect was observed besides irradiation with 355 nm light at higher laser intensities (≥ 50 MW/cm^2). Solution filtration and intentional doping experiments showed that nanoimpurities might play a significant role in explaining NPLIN phenomena.

3.1. INTRODUCTION

Crystallization is arguably the most widely used separation and purification techniques applied in a multitude of industries such as pharmaceuticals, food & beverage, agriculture, fine chemicals and many more [1–8]. The process of crystallization consists of two main stages, namely nucleation and growth. Significant advances in the understanding of the mechanism of nucleation from solution have been made[9–13], yet many aspects of the nucleation process, such as the mechanism of polymorph selection and on-demand spatial-temporal control, are far from being completely understood.This makes the deterministic design and scale up of industrial crystallization processes challenging.

In an attempt to improve control over nucleation and consequently over crystal properties, more advanced crystallization methods are sought. One promising technique is Non-Photochemical Laser Induced Nucleation (NPLIN), where a nanosecond laser pulse is used to trigger instantaneous crystallization in supersaturated solutions that would otherwise take several weeks to nucleate without any external interference [14]. This physicochemical process is termed 'non-photochemical' because the solution does not absorb any light at the irradiated wavelength, and hence the laser pulse does not induce any photochemical reaction[15].

Numerous studies have been conducted on this phenomenon, gathering data on experimental parameters influencing NPLIN such as laser intensity, laser polarization, supersaturation, and impurities [15–18]. Many compounds, including small organics [19–21], metal halides[22], single component systems [23, 24], dissolved gases[25, 26] and a macromolecule - lysozyme[27] have been crystallized with NPLIN. Based on the collected observations, three mechanistic hypotheses were proposed to explain the NPLIN phenomena. The first mechanism is based on the Optical Kerr Effect (OKE), i.e., the electric field of the laser induces a dipole moment in the system and can further produce a torque to align the molecules in the cluster along the field direction accelerating the structural order in the cluster to form a crystal [14]. This light induced alignment of the molecules have also been proposed to explain reports on polymorphic form control with polarization of light, reported for supersaturated solutions of glycine [28], sulfathiazole[29] and carbamazepine[30]. The second mechanism was proposed by

Alexander *et al.*[16], suggesting an explanation based on the Isotropic Electronic Polarization (IEP). The hypothesis is based on the fact that, in the presence of an applied optical electrical field, the free energy of a dielectric particle is reduced when immersed in a medium of lower electric permittivity. The reduction in free energy of the pre-nucleating clusters leads to reduction in the size of critical nuclei and thus enhances the nucleation kinetics. However, this mechanism fails to explain how NPLIN favours the preferential formation of certain polymorphs in NPLIN experiments. The third potential mechanism proposed is based on the heating of impurity nanoparticles existing in the system - molecular impurities (intrinsic) and/or dust particles (extrinsic). The nanoparticles are hypothesized to heat up on absorbing the incident laser light and the resulting heat is then transferred to the surrounding liquid vaporizing volume of liquid around them. Upon evaporation of liquid, the growth of the vapour bubbles promotes the aggregation and accumulation of the solute molecules at the vapour liquid interface driving them to nucleate and form crystals. Yet, no clear consensus on mechanism has been reached, as the proposed mechanisms fail to fully describe all the reported experimental results in literature[15].

Research on NPLIN is largely hindered by the stochastic nature of the phenomenon, requiring a substantial number of repeated experiments to draw definitive conclusions. Therefore, past research on NPLIN studies often used large numbers (order 10 to 100) batch samples to reach statistically significant data points, a labor intensive procedure[18, 31]. In 2014, Clair *et al.*[32] developed the first high throughput controlled setup for NPLIN studies. The setup used an automated carousel holding 90 HPLC vials that a laser could irradiate through the air/liquid interface. Even though this setup takes away much of the manual labour, it still results in long processing times needed to obtain large data sets because of manual crystal detection. Microfluidics represents an alternative to acquire automated and statistically reliable data and has already proven its value in the investigation of crystal synthesis of pharmaceuticals, nanocrystals and proteins [33–40].

So far, only two studies on NPLIN in continuous systems have been reported in the literature. Hua *et al.*[41] presented a single phase microfluidic device that exposed a continuously moving supersaturated solution of KCl to pulsed laser beams. In their device, supersaturation is regulated by strict temperature control of the microchannel, which permits cooling of the solution upon entry and reheating near the exit to avoid clogging of the channel. This study provided insight into the effects of supersaturation, laser energy, pulse duration, and the number of pulses on the number of crystals and their size. The authors further expanded their work with their set-up to study NPLIN on supersaturated aqueous glycine solutions [42]. Upon irradiation of freshly prepared supersaturated glycine solutions (S = 1.4 - 1.6), no NPLIN effect was

observed. However, a significant increase in nucleation probability was seen when the glycine solutions were left to age for 24 hours in a sealed syringe. The effect of ageing glycine solution had already been reported in experiments conducted with milliliter size vials[18, 43]. Moreover, results of Hua *et al.*[41] also agreed with prior batch studies that observed a change of glycine crystal morphology with increasing supersaturation.[20, 44].

In this study, we present a droplet-based microfluidic setup tailored for NPLIN studies where the droplets containing crystals identified using the deep learning method. Using this tailor designed setup, we performed a systematic study of NPLIN-affecting parameters (laser wavelength, peak laser intensity, solution supersaturation, solution filtration and intentional doping with nanoparticles) on supersaturated aqueous KCl solutions. The microfluidic device was designed to create stable, supersaturated droplets of the solution with desired volume, allowing every droplet to act as a separate micro-reactor. In comparison to the traditional manual methods used in NPLIN experiments which only allow for a limited number of experiments (10 to 100)[16, 32], our device enables the collection of a much larger quantity of independent data points, typically over 1000 experiments, effectively addressing the stochastic nature of the crystallization process. The NPLIN experiments are conducted by exposing aqueous KCl droplets of designated supersaturation (1.05 and 1.1) created by cooling the droplets from 40 °C to room temperature. The droplets are exposed to continuous 10 Hz laser pulses at designated peak laser intensity (varied between 10 to 100 MW/cm^2) and wavelength (1064, 532 and 355 nm) with an unfocused laser beam diameter of 1.35 mm. Moreover, we report how filtration and addition of nanoparticles influences the NPLIN probability and discuss our results in the context of dielectric polarization and the nanoparticle heating mechanisms proposed for NPLIN.

3.2. EXPERIMENTAL

3.2.1. MATERIAL

KCl (Sigma Aldrich, molecular biology¸ 99.0 %, CAS: 7447-40-7) solutions in Ultrapure water (ELGA Purelab, UK, 18.2 *MΩ.cm*) and Silicone oil, with a viscosity of 10 cSt (Sigma Aldrich, CAS: 63148-62-9) were used, respectively, as dispersed and continuous phase. The solutions were prepared by adding the designated amount of KCl to reach desired supersaturation at room temperature and stirred rigorously. The prepared solutions are then placed in the oven at 50°C to ensure the complete dissolution of all crystals. The solutions were maintained at this temperature until they are used in experiments. Supersaturated solutions were prepared based on 352.4 g KCl/kg water solubility at 25 °C [45].

3.2.2. SOLUTIONS DOPED WITH NANOPARTICLES

In order to produce supersaturated solution samples doped with known amounts of solid nanoparticles, a stock solution of KCl with concentration C = 5.42 mol/kg (S = 1.127) was prepared and filtered into cleaned beaker at 50°C. A known quantity (1.25 g) of liquid dopant was added to the filtered solution to give a resulting concentration of C = 5.29 mol/kg (S = 1.1). The liquid dopant included aqueous dispersion of iron oxide nanoparticles (≥97%, CAS: 1317-61-9, 50-100 nm nominal diameter), with pure water as a control, prepared in the similar way as given in the article from Ward *et al.*[46]. Dispersion was than subjected to ultrasonic treatment (750 W, CV334) for a period of 2 h before use to ensure maximum dispersion.

3.2.3. MICROFLUIDIC SETUP

A droplet-based microfluidic system to study NPLIN was designed and developed to generate large data sets (≈1000 droplets) for each parameter investigated, where each droplet acts as an independent crystallization reactor. The schematics of the system are shown in Figure 3.1. The system is divided into three main sections: the droplet generation zone, the laser exposure zone and the crystal observation zone.

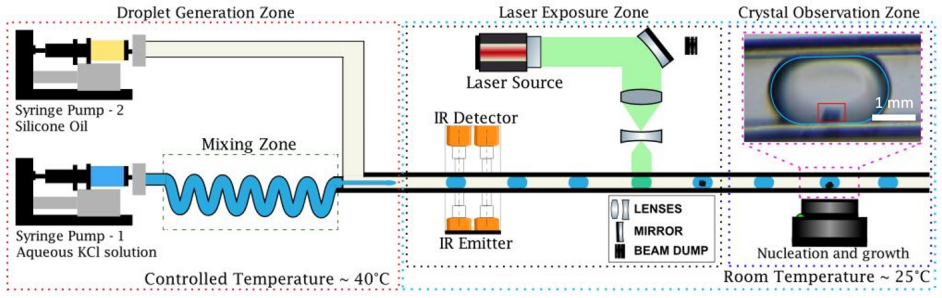

Figure 3.1.: A schematic representation of the droplet-based microfluidic system designed for this study. The system consists of three different zones: droplet generation, laser exposure, and crystal observation.

DROPLET GENERATION ZONE

The droplet generation zone is placed within a temperature controlled environment, kept at 40°C, to ensure that no crystallization takes place during the droplet generation process. Two microfluidic syringe pumps (NE-1002X-ES, New Era Pump Systems Inc.) are used: one for the dispersed phase, namely aqueous KCl solution, and one for the continuous phase, i.e., silicone oil. Both dispersed and continuous

streams flow through polytetrafluoroethylene (PTFE, 900 μm diameter) tubes connected to the syringes, at 10 and 100 μL/min, respectively. Immediately after being pumped into the system, aqueous KCl solution encounters a mixing zone of ten bends to ensure homogeneous solution concentration. Bends are reported to break the symmetry in the velocity field within the fluid direction by promoting variations in wall drag forces, thus inducing passive mixing[47, 48]. After leaving the mixing zone, the dispersed phase meets the continuous phase at a T-junction, for the coaxial formation of the droplets. The dispersed phase flows through an inner round capillary (Vitrocom Inc., borosilicate, 700 μm diameter) surrounded by a squared glass capillary(Vitrocom Inc., borosilicate, 900 μm side) through which the continuous phase flows, leading to the formation of the droplets at the edge of the inner capillary. It is worth noting that both material and geometry changes, from round PTFE tubes to glass squared capillary, were necessary. PTFE tubing is not suitable to withstand the incident laser light while the square geometries help minimise reflection and refraction of the laser. The glass capillary was hydrophobized (see Appendix B section B.1[49]) to minimize the interaction between the droplet and square capillary, which could otherwise induce crystal nucleation within the droplets.

LASER EXPOSURE ZONE

As the droplets form and flow through the square glass capillary, they enter the laser exposure zone, located outside the temperature-controlled environment (40 °C). Hence, droplets undergo cooling to room temperature (25 °C) and become supersaturated after travelling approximately 15.6 mm, a distance much smaller than the distance between the T-junction and location of the laser irradiation, (see Appendix B section B.2[49]) for details of this calculation). An infrared (IR) sensor set was implemented at the beginning of the laser exposure zone. Data from the set of IR sensors is used to count and measure droplet velocity and volume.

Droplets are irradiated 8 cm after leaving the temperature-controlled environment by an unfocused pulsed laser beam (10 Hz, 9 mm diameter, Nd-YAG laser, Continuum Powerlite DLS 8000). The beam was redirected towards a set of two lenses, positioned in a telescopic fashion, by a first mirror, as shown in Figure 3.1. In this arrangement, the reduction of the beam size (from 9 to 1.35 mm diameter) and amplification of the laser intensity are achieved. As the droplets are irradiated 8 cm after leaving the temperature-controlled environment, a distance much greater than 15.6 mm predicted to reach desired saturation, we can safely assume that the droplets are irradiated after they reach the designated supersaturation.

CRYSTAL OBSERVATION ZONE

The observation zone is located 16 cm after the droplets were exposed to the laser beam. Within this distance, KCl crystals can nucleate and grow within the droplets. Droplets in the capillary are imaged using an objective lens (4X, 0.1 NA), a microscope camera, and a diffuse white LED light source. The observation time here, limited by the length and cross-sectional area of the squared glass capillary, positioning of the imaging system, flow rates of continuous and dispersed phases was found to be approximately 70.7 seconds. Droplets containing crystals were counted manually and automatically through a tailored image processing code for comparison. The results of automatic count of droplet containing crystals were used in evaluating the cumulative nucleation probability at a fixed time lag of 70.7 seconds, defined here as the ratio of the droplets containing crystals to the total number of droplets for a given experiment.

3.2.4. DROPLET IDENTIFICATION

INFRARED SENSORS

The infrared sensors (IR) were used as a non-invasive measuring technique to detect interfaces between the continuous and the dispersed phase through the refracting and reflecting nature of the curved interface between them. Each IR sensor consists of an IR LED and photodiode (BPV10NF), located on opposite sides of the capillary. Both parts were held in place by a 3D-printed sensor holder, and mounted in a circuit with two operational amplifiers (Op-Amp MCP6241) to improve signal quality. The recognition of the droplets by the IR sensors is based on the differences in light transmission from the LED to the diode at the edge of the oil water interface of the droplets compared to that in the continuous phase respectively. Since the curvature of the interface deviates the light emitted by the LED, fewer photons reach the photodiode and a drop in the voltage generated can be seen. The sensors were connected to a hardware prototyping platform (Arduino Mega, ATmega 328P, Arduino LLC, Ivrea, Italy) that provided data collection and analysis. The data was used to identify the peak of each voltage drop, i.e., the liquid-liquid interfaces, and to count, estimate the volume and determine droplet velocity. An example of data collected by Arduino can be found in Figure 3.2A.

DEEP LEARNING METHOD

Parallel to the IR sensors, another droplet identification technique was developed to count the droplets, estimate their length and determine their velocity from experimental videos using deep learning method. In addition, the algorithm developed was also capable of counting the

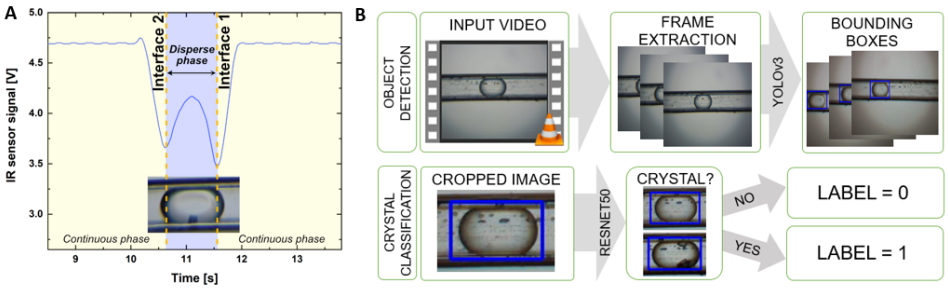

Figure 3.2.: Droplet identification using (A) Infrared (IR) sensors, (B) Illustration of deep learning method implemented to calculate cumulative nucleation probability automatically.

droplets containing crystals automatically. The algorithm includes object detection and crystal classification based on two deep learning models as shown in the flowchart in the Figure 3.2B.

For the object detection, an experimental video was divided into frames firstly. The frames were then used as an input to YOLOv3 for droplet detection. YOLOv3 gives the probability of a droplet being present in an image and generates a bounding box around the image. This bounding box allows us to find the droplet location in the image, and further can be used to calculate its velocity. The bounding box around the droplet is than used to crop only the droplet area as it is much easier to see crystals in a cropped image than in a complete image. The cropped area is then padded to increase the image size to 128×128. At this point, another deep learning routine (ResNet50) was used to classify the image based on whether or not there was a crystal in the droplet.

Classification of the cropped images to detect the presence of the crystal is more challenging than droplet detection. One of the primary reasons for this difficulty is attributed to the different morphology of KCl crystals, as shown in the Appendix B Figure SIII[49]. To solve these problems and to accurately detect the presence of the crystal, a parameter called alpha (α) defined as the ratio of the frames in which the crystal is seen within the droplet to the frames in which the droplet is seen was optimized. In addition to this, a ResNet50 algorithm was used to get high accuracies and F1-scores for different experimental videos. Furthermore, details regarding training process of the algorithm and output quality of the classifier in the form of confusion matrix numbers for all the experimental videos of $S = 1.1$ is provided in the Appendix B Table SIII[49].

STATISTICAL ANALYSIS

The microfluidic device allows for statistically significant number of experiments (≥ 1000 experiments) under identical conditions to be conducted in comparision to classic NPLIN experiments (10 to 100 experiments), with low consumption of solute and solvents. The advantage of those large amounts of virtually identical experiments is the statistical significance of the obtained results, with major improvements regarding reliability over batch experiments[50–54]. In the experiments performed in this study, the number of droplets containing crystals was divided by the total number of droplets to obtain the cumulative nucleation probability at fixed time lag. Nevertheless, the droplets generated in the microfluidic device are not exactly the same and a distribution is expected regarding droplet volumes, which are intrinsically related to the nucleation probability[54–56]. Thus, it is essential to analyse mean droplet volumes (μ_v), standard deviation (σ_v), variance (σ_v^2) and coefficient of variance ($\psi = \sigma_v/\mu_v$) in all experiments, to make sure volume variation will not significantly affect the nucleation probabilities. To account for the error in the nucleation probability, the Wilson's score method was chosen to calculate statistical (95%) confidence intervals [57].

3.2.5. LASER IRRADIATION EXPERIMENTS

The developed microfluidic system is used to quantify NPLIN probability as a function of supersaturation, laser wavelength, laser intensity, solution filtration and intentional doping. Table 3.1 offers an overview of the experimental conditions for all experiments. Supersaturated aqueous KCl solution used as the dispersed phase are prepared with two different supersaturations (S = 1.05 and 1.10). The cooling crystallization experiments with identical supersaturations were performed as controls for the laser irradiation experiments. In both irradiation and control experiments performed, the desired supersaturation was created by allowing the droplets to cool down from the temperature of the droplet generation zone, illustrated in Figure 3.1. For the NPLIN experiments, droplets of solution were irradiated with the laser beam 8 cm after droplet generation in the temperature-controlled environment. Laser wavelengths (1064, 532 and 355 nm) commonly used in NPLIN literature were utilized to investigate the effects of laser wavelength on the nucleation probability. Four different laser intensities (10, 25, 50 and 100 MW/cm^2) were tested at each wavelength. Moreover, the role of impurities facilitating nanoparticle heating mechanism was examined by filtering KCl solutions through different pore size filters and intentionally doping Fe_3O_4 nanoparticles into the filtered solutions.Each experiment consisted of at least 1000 droplets.

Table 3.1.: Overview of experimental conditions used during laser irradiation experiments varying supersaturation, laser wavelength and laser intensity.

Experimental condition	Value	Unit
Dispersed phase fluid	KCl	
Dispersed phase flow rate	10	μL/min
Continuous phase fluid	Silicone oil	
Continuous phase flow rate	100	μL/min
Supersaturation ratios (S)	1.05, 1.1	
Laser wavelengths	1064, 532, 355	nm
Laser diameter	1.35	mm
Laser intensity	10, 25, 50, 70, 100	MW/cm^2
Laser frequency	10	Hz

3.3. RESULTS & DISCUSSIONS

3.3.1. DROPLET CHARACTERIZATION

The droplet length distribution was characterized via both the IR sensors and the deep learning method for all the experiments performed and the results are shown in the Appendix B Table SI[49]. An example of the droplet length distributions for one of the experiment (S = 1.1, 1064 nm, 25 MW/cm^2) in the form of histograms can be found in the Appendix B Figure SI[49]. The length distribution based on histograms for both the methods employed displays no outliers, and the coefficient of variance was found to be 27% and 10% respectively. The absence of outliers indicates that neither droplet coalescence nor breakage is taking place in the system. The length data obtained through the IR sensor yields a broader distribution and, consequently, a lower average length compared to the length distribution data from the deep learning method. This is most likely due to the susceptibility of the IR sensor to external light sources. On the other hand, despite relying on an external light source to record the passing droplets in the capillary, the method of detecting droplet size by video microscopy coupled with deep learning method was less prone to interference from the light source. Also we compared a small sample of manually measured average droplet lengths (consisting of 100 droplets) with the average length data obtained from both the IR sensor and the deep learning method. These results can be found in the Appendix B Table SII[49]. The manually measured average droplet length closely matched the data obtained from the deep learning method, reinforcing the conclusion that the deep learning method provides more accurate droplet length data than the IR sensor. Consequently, further calculations were performed using the average length data obtained from the deep learning method.

Droplet volume variation affect nucleation probability distribution,

since nucleation rates and detection times are intrinsically related to the volume of the crystallizer [54]. Moreover in NPLIN literature, the sample volume exposed to the laser has a significant effect on the nucleation rate of NPLIN according to Alexander *et al.*[16]. Thus, characterization of the droplet size is essential for robust statistics in studying NPLIN through microfluidics .

When comparing all the experiments performed under S = 1.05 and 1.10, we observed that the volume of droplets created varied. This variation was caused by slightly different inner capillaries used, with capillary diameters varying between 300 and 400 μm. The variation of capillary diameters accross experiments was unavoidable in the experiments, as the capillaries were fragile. They were replaced several times due to breakage while assembling the setup. Despite the error bars of volume distributions overlapping, the average volume changed significantly between experiments (more information is provided in the Appendix B Figures SIIA & SIIC[49].

To test whether the measured nucleation probabilities were dominated by unavoidable volume variations between experiments, we performed three independent cooling experiments where the mean droplet volume was intentionally altered. Figure 3.3A shows the nucleation probability of three droplet populations with varying mean volume at S = 1.1. We ensured that the variation in mean droplet volume in Figure 3.3A was similar to the experiments reported. No significant differences in the measured nucleation probability were observed in Figure 3.3A, as the error bars overlapped for the three independent cooling experiments with three different average droplet volumes. The range of average droplet volume values changed in these three experiments was approximately the same as the variations observed in NPLIN experiments reported in this study. Hence, we conclude that the unavoidable variations in droplet volume in controlled cooling and NPLIN experiments do not significantly alter the measured nucleation probabilities.

Since the laser is irradiating the glass capillary at 10 Hz, both continuous and dispersed phase get irradiated by multiple laser pulses. As a result, the average number of pulses per droplet vary from 11 to 15 between different experiments due to variation in droplet volume and is shown in the Appendix B Figure SIIB & SIID[49]. Previous reports have demonstrated that the number of laser pulses per unit volume does not influence nucleation probabilities[16, 18, 41]. Irimia *et al.*[18] compared nucleation probabilities in 8 ml vials containing glycine solutions, irradiated with a single pulse and 1 minute laser exposure (600 pulses) using a 1064 nm laser, and found no significant difference. Nonetheless, with the presented experimental setup, it is not possible to expose droplets to a fixed number of pulses. This is a shortcoming of the developed system. A solution to this issue would be developing a microfluidic system in which droplets are temporarily stopped and

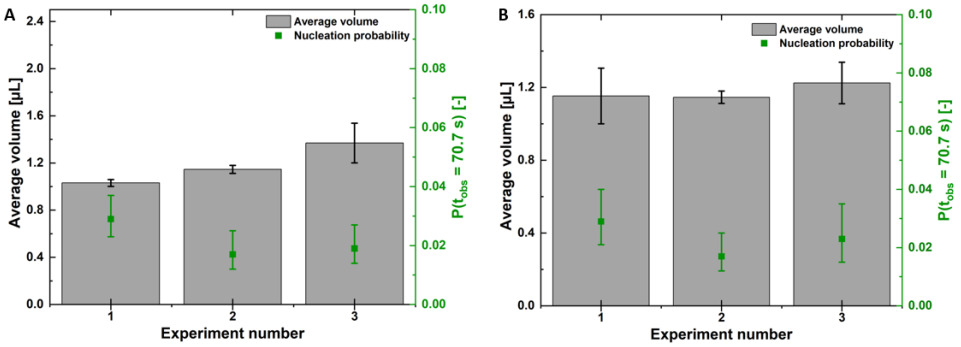

Figure 3.3.: Nucleation probabilities and average droplet volumes for cooling experiments. (A) Results are shown for three distinct average droplet volumes conducted at S = 1.1 to evaluate the impact of average droplet volume on measured cumulative nucleation probabilities with a fixed time lag of 70.7 seconds. Here time lag refers to the time between laser irradiation and detection of crystals within the droplets (B) Average droplet volumes and nucleation probabilities for three different cooling experiments conducted at S = 1.1 are presented to assess the experimental reliability of the developed microfluidic system.

then exposed to a single pulse, similar to the technique used in stop-flow lithography[58]. However, designing and implementing such a system would require advanced microfluidic techniques and coordination between the detection system and the laser, which is beyond the scope of this current work.

3.3.2. COOLING EXPERIMENTS & REPEATABILITY

The repeatability of the microfluidic setup is checked by performing three independent cooling crystallization experiments at fixed supersaturation, S = 1.1, under identical conditions(laser intensity, wavelength and cooling profile) including similar average droplet volumes. The results of these experiments are shown in the Figure 3.3B. No significant difference was observed in the nucleation probabilities recorded as the error bars of measured nucleation probability overlapped for the all the independent cooling experiments.

The nucleation probabilities measured for the control (cooling) experiments were lower than 3% for S = 1.10 and lower than 1.5% for S = 1.05. We attribute the measured non-zero nucleation probabilities to the high surface area to volume ratio of the droplets facilitating heterogeneous nucleation. Hua[41] used comparable KCl supersaturations (from 1.06 to 1.10) and detected no nucleation for the control experiments in single-phase microfluidic NPLIN experiments.

The solution flow was continuous in that study, providing a much lower surface area to volume ratio. Another potential reason is the temperature variation between experiments. Despite the fact that the lab is temperature-controlled, we cannot rule out the possibility of minute fluctuations affecting the supersaturation.

3.3.3. LASER IRRADIATION EXPERIMENTS

Figure 3.4 displays the nucleation probabilities at fixed observation time for varying laser intensity (MW/cm^2) at three different wavelengths. To facilitate quick comparison with NPLIN experiments, the results of the control (cooling) experiments included in the plot as a solid line with error bars represented as dotted line. It is worth mentioning that the average nucleation probability obtained in this study is fairly small when compared to previous reports [16, 17] for KCl. This difference is due to much lower volumes (three orders of magnitude lower) used in microfluidic scale [55] for laser irradiation and to the substantially different detection times of crystal observation. Alexander *et al.*[16], while conducting experiments with supersaturated KCl solution, used a fixed detection time of 20 minutes, to check the samples for crystal formation after laser irradiation. Kacker *et al.*[17] used a fixed detection time of 60 minutes to ensure nuclei had sufficient time to grow to a detectable size, even though after 20 minutes the authors observed no significant change in the nucleation probability. On the other hand, Hua *et al.*[41], in their microfluidic device, varied the detection times from (1 - 20 minutes) in their experiments for different combinations of supersaturation, laser intensities and laser pulses in order to record number of crystals. In our experiments, the detection time is approximately 70.7 seconds and it is limited by the flow rates of dispersed and continuous phase solutions, length of the square glass capillary and the position of the imaging system. Furthermore, the nucleation probabilities found in the cooling experiments will serve as a reference for the laser irradiation experiments. In hindsight, the low nucleation probabilities measured in our experiments can be improved by increasing the length of the capillary in order to accommodate longer detection times for crystal observation. However our attempts to work with longer capillaries were hampered by clogging issues due to poor hydrophobization [59]. Additionally, the use of a silicone tubing in combination with 30 cm capillaries to prolong the droplets residence time caused leaks at the point where tubing was connected to the capillary tube. Therefore, capillary tubes longer than 30 cm were not used in this study.

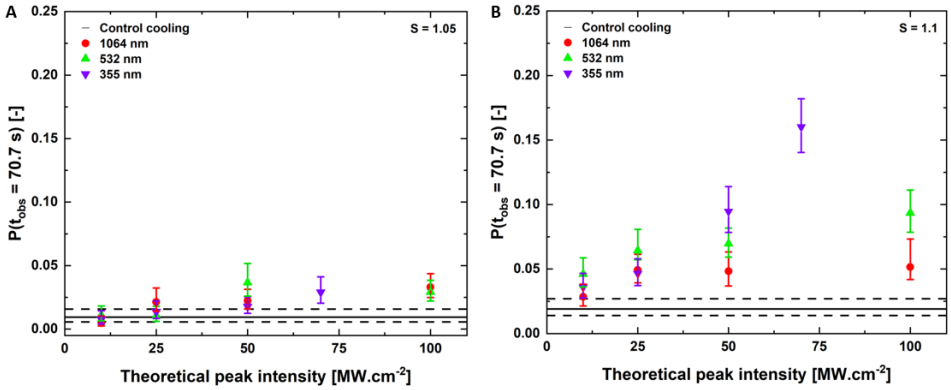

Figure 3.4.: Nucleation probabilities for the experiments performed under supersaturations of (A) S=1.05 and (B) S=1.10, irradiated by 1064, 532 & 355 nm laser wavelengths. The dotted lines refer to the nucleation probability from control cooling experiments that serve as a reference to laser irradiation experiments. Note: An example of the nucleation probability numbers for one of the experiments (S = 1.1, 1064 nm, 25 MW/cm^2), P(t_{obs} = 70.7s)) ≈ 0.049 signifies that out of 1483 droplets, there were N = 73 crystallization events.

EFFECT OF LASER INTENSITY

No laser intensity effect was observed at S = 1.05 (Figure. 3.4A). For laser irradiation up to 50 MW/cm^2 peak intensity, the measured nucleation probability was identical to the control experiments - except for 532 nm at 50 MW/cm^2. Only for peak intensities higher than 50 MW/cm^2 the laser pulses did the laser pulses increase the nucleation probability for all the wavelengths, as the probabilities recorded exceeded those of the control experiments. No significant effect of wavelength on the nucleation probabilities was observed as error bars overlapped.

For S = 1.10 (Figure. 3.4B), the overall trend showed that irradiation with increasingly higher laser intensities increased the nucleation probability. At 532 nm, an increase in the nucleation probability is observed for 25 and 100 MW/cm^2, yet the probabilities for 25 and 100 MW/cm^2 are not statistically different. The slow increase in nucleation probability for 532 nm and 1064 nm between 25, 50 and 100 MW/cm^2, may indicate a saturation value above which increasing the laser intensity no longer has a direct effect on the nucleation probability. This observation is corroborated by previous literature observations [17]. For 355 nm, the nucleation probabilities were found to increase with increasing peak laser intensities more steeply than for other wavelengths.

One possible explanation for the less steep increase observed for 532

nm and 1064 relative to 355 nm could be the local heating of the solution resulting in lower supersaturation values . Around 1064 nm, water has a slight absorption band [60, 61] which would imply some heating effect in the supersaturated solution upon laser irradiation. Previously, Irimia *et al.*[18] conducted batch NPLIN experiments with supersaturated aqueous glycine solutions at a 1064 nm laser wavelength. They observed a similar local heating of the solution and identified two competing phenomena with opposite effects. The local heating of the supersaturated solution reduces the supersaturation, thereby lowering the nucleation probability. On the other hand, a temperature gradient induces mixing, which contributes to the enhancement of the apparent nucleation probability. According to the authors, the temperature effect on batch samples (8 ml) is negligible. In our study, the much lower volume of the droplets and the fact that the full droplet is irradiated eliminates the induced convective mixing effect, and its influence on the nucleation probability. While this interpretation might not hold for all wavelengths, it does apply for KCl solutions between 355 - 532 nm. Within this range, the solutions show no detectable absorption bands[60, 61], despite the small ones shown by water near 355 nm[62]. These bands are so weak that they cannot cause any significant heating effect, particularly when compared to the near-infrared spectrum.

Another explanation might be found in impurity heating mechanism. This mechanism revolves around the rapid heating of impurity nanoparticles, which leads to the formation of a small vapor cavity, analogous to laser-induced cavitation. In the vicinity of this cavity, the solute concentration may be enhanced, thereby promoting nucleation [63]. Nevertheless, as these impurity particles absorb energy, a rapid temperature increase occurs in the surrounding solution, temporarily reducing local supersaturation. At lower intensity irradiation, the applied energy may not be large enough for the solution temperature to reach the vaporization temperature [46, 63, 64]. A competition between heating and vapor cavity effects on supersaturation may take place at higher laser peak intensities, suggesting a threshold value for NPLIN. Previous studies in the literature have shown evidence of threshold intensities. Alexander *et al.*[16] reported a threshold for NPLIN in batch KCl solution samples, indicating its value to be practically supersaturation independent at 6.4 ± 0.5 MW/cm^2. Kacker *et al.*[17], in batch irradiation of S = 1.035, 1.049, and 1.055 KCl solutions, found the threshold value to be around 0.5 MW/cm^2 and observed 100% nucleation at laser intensity values above 5 MW/cm^2. In this study, threshold values were found to be $\geq$ 10 MW/cm^2 for S = 1.10 and $\geq$ 50 MW/cm^2 for S = 1.05. The difference in threshold values is possibly due to the smaller volumes used in this study. The dynamics in a batch scale experiment differ significantly from the effects observed on the microfluidic scale[56]. In droplet microfluidic experiments, much

smaller volumes and detection times are used. Furthermore, the entire solution volume is irradiated by the laser, as opposed to partial volume irradiation in batch experiments.

EFFECT OF LASER WAVELENGTH

Overall, no significant wavelength effect on nucleation probability was observed. The measured nucleation probabilities followed the same trend when S = 1.05 (Figure. 3.4A) solutions were irradiated with three different wavelengths. The error bars for all laser intensities overlap in Figure. 3.4A , indicating no statistically significant wavelength effect. At S = 1.10 (Figure. 3.4B), also no significant variation was observed when droplets were exposed to 1064 or 532 nm laser pulses. Even at the higher laser intensity (100 MW/cm^2), the obtained nucleation probabilities are still considered comparable.

An exception of this general trend is nucleation probabilities measured in droplets irradiated at 355 nm for intensities $\geq$ 50 MW/cm^2. It is noteworthy to mention that the irradiation with 355 nm proved to be experimentally challenging compared to experiments conducted with 1064 and 532 nm. Whereas with 1064 and 532 nm it was possible to irradiate the square borosilicate capillaries with laser intensities up to 100 MW/cm^2 for a long period of time (over 2.5 h), at 355 nm the irradiation above 70 MW/cm^2 resulted in broken capillaries in a matter of minutes. This observed effect hindered data collection at these higher laser intensity values, so the highest applied laser intensity for 355 nm was 70 MW/cm^2.The nucleation probabilities under 355 nm were approximately two times higher than for 1064 and 532 nm above peak laser intensities ($\geq$ 50 MW/cm^2). Slightly higher nucleation probabilities upon irradiation of KCl solutions with 355 nm as compared to irradiation with 1064 and 532 nm have been reported before for all laser intensities[17]. However, in our studies, the effect was only observed for the higher laser intensities ($\geq$ 50 MW/cm^2). The wavelength effect observed in our study could also be attributed to the photochemical effect induced by UV light irradiation, potentially heating smaller impurity particles in a manner distinct from the nanoparticle heating mechanism[17, 65]. However, a definitive verification of this hypothesis extends beyond the scope of the current work.

EFFECT OF SUPERSATURATION

NPLIN probability has been reported to increase with increasing supersaturation in macroscopic NPLIN experiments [22]. Comparing panels A and B in Figure.3.4 shows how supersaturation influences nucleation probability. Overall, nucleation probabilities for all theoretical peak intensities are higher for S=1.10 compared to S=1.05. For S = 1.10, irradiation with 10 MW/cm^2 has a higher NPLIN probability than

the control indicated with dotted lines. On the other hand, for S = 1.05, irradiation at intensities up to ≥ 50 MW/cm^2, for 1064 and 355 nm, are still inefficient in triggering NPLIN where the measured nucleation probabilities are similar to control experiments.

3.3.4. COMMENTS ON NPLIN MECHANISMS

DIELECTRIC POLARIZATION MODEL

We first investigate the ability of Dielectric polarization (DP) model hypothesis to explain our experimental findings of nucleation probabilities at different theoretical peak intensities at each wavelength, for both of the studied supersaturations. The DP model can be interpreted such that the number of crystals is directly proportional to the peak laser intensity (Equation 3.1). Equation 3.2 can then be used to describe the nucleation probability[16], where I is the laser peak intensity and m is the lability factor. The lability factor in the NPLIN literature describes the ease with which a system nucleates and is thought to be specific for each solute[22]. In this study t_{obs} denoted fixed observation time taken as $t_{obs} = 70.7\,s$. Analysis of the data in the DP model thus requires the determination of the lability factor.

$$N_{crystals} = mI \tag{3.1}$$

$$P(t_{obs}) = 1 - exp(-mI) \tag{3.2}$$

However, the relationships in Equations 3.1 and 3.2 fail to accurately describe a peak laser intensity threshold for NPLIN to occur, encountered in experimental data[22]. Therefore, Equations 3.1 and 3.2 are generally adjusted to Equations 3.3 and 3.4, respectively, where I_o is the threshold theoretical peak intensity.

$$N_{crystals} = m(I - I_o) \tag{3.3}$$

$$P(t_{obs}) = 1 - exp(-m(I - I_o)) \tag{3.4}$$

The analysis was carried out by plotting a semi-logarithm graph between 1- P(t_{obs} = 70.7s) and the theoretical peak intensity. The experimental data was fitted by linear regression - where P(t_{obs} = 70.7s) is the nucleation probability at the detection time of approximately 70.7 seconds (Figure 3.5). The lability factor was then determined directly from the slope of the line, and through the intercept, threshold peak intensity I_o was calculated. The values are shown in the table 3.2 with 95% confidence intervals.

Analyzing the results for S = 1.05 in Table 3.2, it can be deduced that the lability factor obtained from fitting process fall within 95% confidence

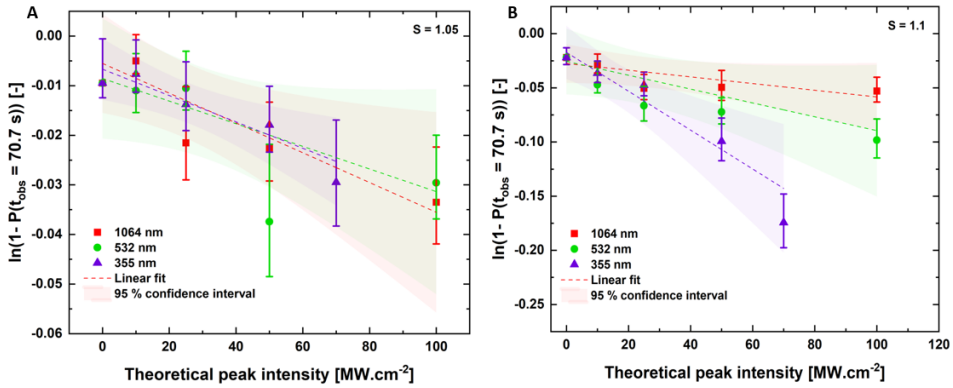

Figure 3.5.: DP model semi logarithm straight line fits with 95% confidence interval prediction for all the wavelengths of experimental data under supersaturations of (A) S=1.05 and (B) S=1.10.

intervals for all laser wavelengths and hence the irradiated solutions had similar ease to nucleate. However, when the lability factor for S = 1.10 is examined, substantial differences can be seen between the factors determined for 1064 & 532 nm and 355 nm. This difference might be due to the considerably higher nucleation probabilities observed for irradiation with 355 nm at higher laser intensities, as opposed to those at 1064 & 532 nm. Interestingly, the confidence interval bounds are in the same order of magnitude as the mean values for both supersaturation levels at all laser wavelengths.

Table 3.2.: Overview of the fitted parameters i.e., lability (m) and threshold peak intensity (I_o) for different wavelengths for both the supersaturations with uncertainties based on 95% confidence intervals.

S	Wavelength (nm)	Lability (cm^2 MW^{-1})	Threshold peak intensity (MW cm^{-2})
1.05	1064	3.00E-04 ± 2.52E-04	-18 ± 33
	532	2.28E-04 ± 2.66E-04	-37 ± 53
	355	2.66E-04 ± 1.79E-04	-25 ± 23
1.1	1064	3.09E-04 ± 7.51E-04	-89 ± 57
	532	6.40E-04 ± 9.77E-04	-40 ± 47
	355	1.80E-03 ± 1.02E-03	-9 ± 13

From Table 3.2, we find that the values of lability at all the wavelengths vary by 1 or 2 orders of magnitude compared to literature values from Alexander *et al.*[22] and Hua *et al.*[42]. The primary reason for this finding is likely the difference in sample volume subjected to laser irradiation. In this study, we irradiate microdroplets of μL volumes with a laser, as compared to the mL volumes reported in the literature. It's worth mentioning that in studies irradiating solutions in 10 mL vials, despite higher nucleation probabilities, the number of crystals per vial is usually 1-2. This means that, despite the larger volume of molecules and particles exposed to the laser, only one or two nuclei succeed in growing to detectable sizes. Considering the much lower volumes in our work, the likelihood of nucleation significantly diminishes. Therefore, to initiate the crystallization process in these smaller droplets, a higher intensity of laser irradiation is likely required to activate particles that are smaller than those that would typically induce crystallization in a larger volume. This observation strengthens the hypothesis of the nanoparticle heating mechanism discussed in the next section. Moreover, the role of interfaces should not be overlooked. In our microfluidic setup, the irradiated beam travels through the glass-oil, oil-solution interfaces twice, yet in macroscopic NPLIN experiments, the irradiation only interacts with the glass-solution interface twice. This difference in interface interaction should be taken into account when comparing results from the microfluidic and macroscopic setup.

Moreover the threshold peak intensity values reported in Table 3.2 for both supersaturations display negative values, which are physically unrealistic. This discrepancy arises because the DP model does not account for background spontaneous crystallization, i.e., nucleation in the control experiments. Additionally, since the nucleation probabilities $P(t_{obs} = 70.7s)$ yield low numbers, the slope of the fitted line is also low, resulting in low lability factors and negative threshold intensities. Improvements to the setup to increase P(t) and reduce background spontaneous crystallization could potentially yield better fitting results. In contrast, multiple laser intensity thresholds for supersaturated aqueous KCl systems under similar conditions were reported in the literature for batch sample irradiation[16, 17, 41], as previously mentioned. From this analysis, we conclude that the DP model could not describe our experimental findings; hence, more focus was put on further experiments testing the (nano)impurities heating mechanism.

3.3.5. SOLUTION FILTRATION

EFFECT OF FILTER PORE SIZE

To investigate the influence of filtration on NPLIN probability, a series of experiments were performed with KCl solution (S = 1.10) with filters of different size, namely 0.22 μm (PTFE syringe filter), 0.45 μm

syringe filters (PTFE syringe filter) and 7 μm paper filter (Grade-3HW, Whatman filter). The experiments were carried out using the developed microfluidic setup and included both control cooling experiments and laser irradiation experiments with incident wavelength of 532 nm and peak intensity of 50 MW/cm^2. The nucleation probabilities obtained in these experiments are shown in the Figure 3.6A.

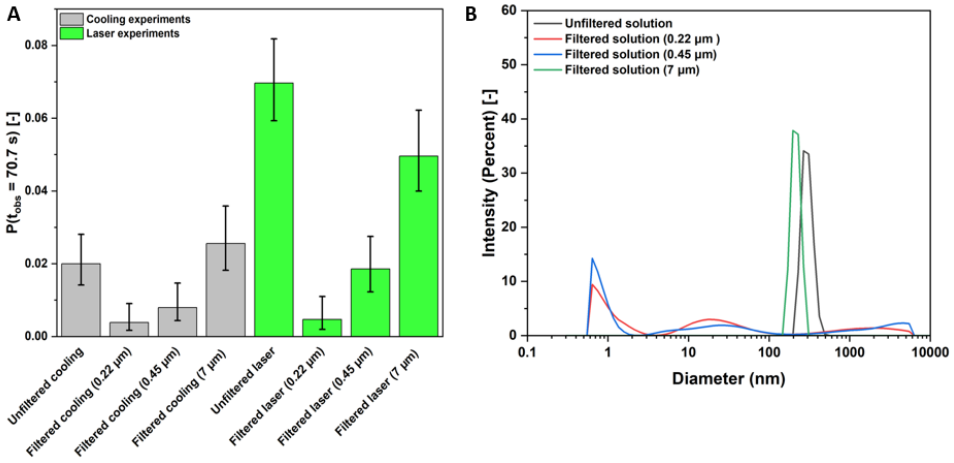

Figure 3.6.: (A) Nucleation probabilities for filtered solution with different pore size diameters and unfiltered solution under S = 1.1 in both control cooling & laser experiments at a constant laser wavelength (532 nm) and constant theoretical peak intensity (50 MW/cm^2) and (B) Particle size distribution obtained for unfiltered KCl solution and filtered KCl solution with 0.22 μm, 0.45 μm and 7 μm filters

Higher nucleation probability was observed in laser experiments with an unfiltered solution as compared to a filtered solution from 0.22 μm and 0.45 μm pore size filters. Moreover, laser irradiation increased the nucleation probability in the unfiltered solution, whilst for the filtered solution, no significant difference is seen between cooling and laser experiments for 0.22 μm and 0.45 μm pore size filters. This observation is attributed to the presence and absence of impurities in the unfiltered and filtered solutions, respectively, which are intrinsically related to the (nano)impurity heating mechanism proposed for the NPLIN phenomena[17, 46, 66]. Yet another explanation for the observed reduced nucleation probability upon filtration is the reduction of existing KCl clusters due to the high shear force produced as the fluid travels through the sub-micrometer size pores of the filter. As drag force scales with size at low Reynolds number flows[58], disordered clusters that are discussed in two-state nucleation theory [9] may be broken into smaller sizes or dissolve back into the solution upon filtration. Further

laser experiment results showed similar nucleation probability for both 7 μm pore size filtered and unfiltered solution, indicating the 7 μm filter was ineffective in removing nanoimpurities/nanoclusters present in the solution. This is further supported by the similar results obtained for control cooling experiments. These findings suggest that the initial presence of nanoimpurities/nanoclusters in the unfiltered solution might be larger than 0.45 μm in mean hydrodynamic diameter and could not be effectively filtered by the 7 μm pore size filter. A supportive evidence to this claim also comes from Dynamic light scattering (DLS) data for these experiments as shown in the Figure 3.6B.

Dynamic light scattering (DLS) was used to estimate the particle size distributions (PSD) in KCl solutions. To prevent spontaneous nucleation, the KCl solution was slightly undersaturated (S = 0.98). The non-negative least squares approach was used to compute the particle size distribution from the DLS data. The measurements were performed for unfiltered KCl solution and filtered KCl solutions with different pore size filters (0.2 μm, 0.45 μm, 7 μm). The correlation functions and the corresponding fitted PSD for all the solutions are shown in Appendix B Figure SIV[49]. The particle size distribution (PSD) of the unfiltered solution reveals a mean hydrodynamic diameter of 264 ± 50 nm. Upon filtration with 0.22 μm and 0.45 μm filters, particles at 264 ± 50 nm were eliminated, resulting in a residual population of particles $\leq$ 70 nm and $\leq$ 200 nm, respectively. Still for solutions filtered with 0.22 μm and 0.45 μm filters, peaks are seen in $\leq$ 1 nm. However, literature reports that particle populations $\leq$ 1 nm from DLS measurements were identified as scattering from the solute and do not correspond to a true representation of the particles in solution[46]. In contrast, filtration with a 7 μm filter produced a PSD in a similar size range to that of the unfiltered solution with a mean hydrodynamic diameter of 209 ± 14 nm. These findings suggest the 7 μm filter was not effective in eliminating nanoimpurities or clusters and led to a nucleation probability comparable to that of the unfiltered solution. Similarly, the 0.22 μm and 0.45 μm filters effectively removed nanoimpurities from the unfiltered solution, thus resulting in lower nucleation probability. The obtained results in Figure 3.6 provide supporting evidence for the nanoparticle/impurity heating mechanism[67].

NPLIN PROBABILITY IN DOPED SOLUTIONS

Subsequently, laser-induced nucleation experiments were performed with filtered solution (0.45 μm pore size filter) doped with Fe_3O_4 nanoparticles (50 - 100 nm nominal diameter) with a concentration of 14.6 μg/ml in solution droplets, with an incident wavelength of 532 nm and a peak intensity of 50 MW/cm^2 to determine if addition of nanoparticles can enhance NPLIN nucleation probability by laser-impurity interaction. The results in Figure 3.7 show a nucleation probability of

100%, with multiple crystals formed per droplet, compared to unfiltered and filtered laser experiments where mostly a single crystal per droplet was observed. One possible explanation for the presence of multiple crystals per droplet is the high number of nucleation sites that are active within the droplet in the form of dopant nanoparticles. Another factor that could contribute to this phenomenon is the use of multiple laser shots (10-15) per droplet, which could trigger secondary nucleation events within the droplet. Similarly, control cooling experiments performed with filtered solution doped with Fe_3O_4 nanoparticles resulted in a nucleation probability comparable to unfiltered and filtered solution (0.45 μm pore size filter) cooling experiments results. These findings provide additional support for the observations derived from laser experiments, indicating that the dopant nanoparticles may not be intrinsically enhancing the nucleation process through heterogeneous nucleation. Instead, the laser-nanoparticle interaction within the droplet is likely the primary factor contributing to the observed nucleation behavior.

The increase in nucleation probability for doping solutions could be attributed to the fact that Fe_3O_4 nanoparticles exhibit a specific absorption efficiency when exposed to 532 nm laser light depending the size of the nanoparticles. This allows us to estimate the energy absorbed by the nanoparticle from the laser. Quantitative information about specific absorption to size of the Fe_3O_4 nanoparticle can be found in the work from Nagalingam *et al.*[68]. This energy can further be used to vaporize the surrounding liquid and create a vapor bubble. To calculate the size of the vapor bubble formed from laser irradiation, we could use simple thermodynamic calculations, assuming that one laser shot on one nanoparticle produces one vapor bubble[26]. However, the DLS result of the filtered doped solution gave a PSD with mean hydrodynamic diameter of 465 ± 33 nm, revealing that iron oxide nanoparticles are agglomerated within the supersaturated solution, a commonly encountered problem in high ionic strength solutions [69]. Consequently, treating the agglomerated particle as a single particle may not be entirely accurate, given that the complex nature of agglomeration leads to modifications in the nanoparticles properties, including variation in its optical characteristics[69]. These differences affect the way the agglomerated particle interacts with laser light. Therefore, accurately estimating the bubble size for the agglomerated system is beyond the scope of this paper.

At this stage, we hypothesize that upon laser irradiation of the filtered doped solution, there might be numerous vapor bubbles that would eventually merge into a larger bubble compared to the bubble size that would have been obtained in an unfiltered solution. The maximum size of the bubble, as predicted by Hidman *et al.*[63] numerically and by Nagalingam *et al.*[68] combining experiments and numerics, would

lead to a higher local supersaturation around the vapor-liquid interface. This increased local supersaturation could accelerate the nucleation process and could explain the much higher nucleation probabilities observed in doped solutions compared to unfiltered solutions upon laser irradiation. Moreover, the morphology of crystals within the droplets obtained in laser-irradiated doped solutions, as compared to unfiltered solutions, supports this hypothesis. In nearly every droplet containing nanoparticles, we observed multiple needle-shaped crystals, suggesting creation of a high degree of local supersaturation upon laser irradiation. This is consistent with reports on the tendency for needle-shaped KCl crystals to form in higher bulk supersaturation conditions. In contrast, the presence of mostly cubic KCl crystals in almost every droplet of laser-irradiated unfiltered solutions indicates relatively lower local supersaturation levels, aligning with the typical formation of cubic crystals in lower bulk supersaturation environments[70, 71].

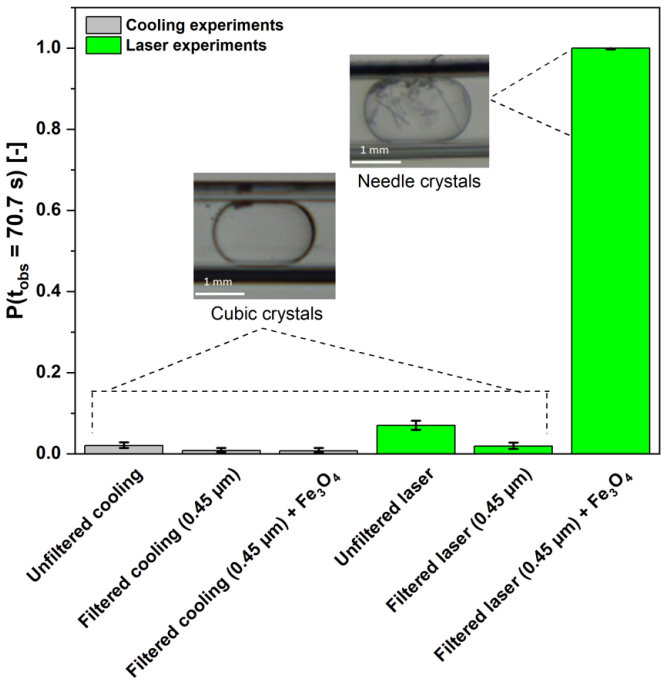

Figure 3.7.: Comparison of nucleation probabilities for filtered solution along with addition of Fe_3O_4 nanoparticles and unfiltered solution under S = 1.1 in both control cooling & laser experiments at a constant laser wavelength (532 nm) and constant theoretical peak intensity (50 MW/cm^2)

From the perspective of impurity heating mechanism hypothesis,

the reduction of the nucleation probability in filtered solutions and enhancement of nucleation probability in dopant solutions may be interpreted as a consequence of the reduced and enhanced interaction respectively between the laser and the impurities. Several authors have provided evidence to substantiate this claim. Javid *et al.* [66] performed NPLIN experiments with filtered and unfiltered aqueous glycine solutions, in which they observed a suppression of nucleation probability in filtered solution and a change in the favoured polymorphic form for filtered glycine solutions compared to unfiltered solutions. Ward *et al.*[46] investigated the effect of intentionally added impurities of Fe_3O_4 nanoparticles and polyethylene glycol surfactant on the nucleation probability and crystal count in aqueous NH_4Cl solutions. These authors have seen that filtration significantly decreases the nucleation probability, which could again be increased to the initial (unfiltered) levels by doping the solution with the Fe_3O_4 nanoparticles. The same authors also found lower nucleation probabilities of CO_2 bubbles in filtered carbonated sucrose solutions[26]. Similarly, NPLIN experiments were carried out in filtered and unfiltered aqueous KCl solutions by Kacker *et al.*[17] in which they concluded that NPLIN depends on the presence of impurities in solution. Although the observations of our experiments, along with previous claims in the literature, strengthen the evidence of a dependence of NPLIN on the presence of (nano)impurities, additional research is still required to deliver a definitive statement on the role of impurities in the induction of nucleation in NPLIN research. Further studies exploring the effects of various nanoparticles with different absorption efficiency, nanoparticle concentration and their sizes on laser intensity threshold and nucleation probability in supersaturated solutions may provide further insights into the mechanism of NPLIN.

3.4. CONCLUSIONS

A droplet-based microfluidic system tailor designed for NPLIN studies, in combination with a fully automated droplet and crystal count monitoring system using a deep learning method, is reported for the first time to study NPLIN. The design addresses a major criticism on the NPLIN literature, i.e., the lack of large data sets due to manually intensive nature of bulk NPLIN experiments. Variations in the form of experimental conditions such as supersaturation, laser wavelength, laser intensity and the effect of solution filtration are studied using aqueous KCl solutions to quantify their influence on NPLIN kinetics and draw parallels with the proposed underlying NPLIN mechanisms in the literature. With respect to the laser peak intensity experiments for $S = 1.05$, laser irradiation was only proven to be effective at laser intensities ≥ 50 MW/cm^2. Notably, no significant difference in nucleation probabilities as

function of the laser peak intensity were found at any wavelength for this supersaturation. For S = 1.10 the irradiation was already seen to be effective at laser intensities ≥ 10 MW/cm^2. As for the influence of laser wavelength, besides larger values obtained with irradiation of S = 1.10 with 355 nm at laser intensities ≥ 50 MW/cm^2, no significant wavelength effect was observed. These observations are speculated to be caused by nonlinear absorption of the light by the impurities within the solution. Finally, concerning the effect of supersaturation, it was evident that a higher supersaturation resulted in a higher nucleation probability. The Dielectric Polarization model could not describe the measured nucleation probabilities with different wavelengths, as the lability parameters and threshold peak intensities calculated are inconsistent with literature and physically unrealistic. Solution filtration with pore size less than 7 micrometers suppressed the NPLIN probabilities. The addition of Fe_3O_4 nanoparticles to the filtered solution enhanced the nucleation probabilities and altered the morphology of emerging crystals. These results highlight the role of the impurities in the solution and reinforce the nanoparticle/impurity heating mechanism hypothesis for NPLIN. It is noteworthy that the droplet microfluidic setup presented here exhibits some limitations arising from both the small volume of the droplets and the high surface area-to-volume ratio. As a result, it yields low nucleation probabilities and increases the background spontaneous nucleation (control experiments). Experimental efforts to increase the measured NPLIN probabilities by increasing supersaturation resulted in clogging of capillary downstream. Experiments at higher observation times or higher laser intensities to measure higher NPLIN probabilities was experimentally challenging due to fragile nature of the capillaries. Despite these limitations, the proposed setup may offer advantages such as statistical accuracy and ability to automation, provided that droplet microfluidics setup is re-designed to reach higher observation times or higher laser intensities.

REFERENCES

[1] Z. Gao, S. Rohani, J. Gong, and J. Wang. “Recent Developments in the Crystallization Process: Toward the Pharmaceutical Industry”. In: *Engineering* 3.3 (2017), pp. 343–353. doi: http://dx.doi.org/10.1016/J.ENG.2017.03.022.

[2] J. A. Dirksen and T. A. Ring. “Fundamentals of Crystallization: Kinetic Effects on Particle Size Morphology”. In: *Chemical Engineering Science* 46.10 (1991), pp. 2389–2427. doi: https://doi.org/10.1016/0009-2509(91)80035-W.

[3] J. H. ter Horst, C. Schmidt, and J. Ulrich. “32 - Fundamentals of Industrial Crystallization”. In: *Handbook of Crystal Growth (Second Edition)*. Ed. by P. Rudolph. Second Edition. Handbook of Crystal Growth. Boston: Elsevier, 2015, pp. 1317–1349. isbn: 978-0-444-63303-3. doi: https://doi.org/10.1016/B978-0-444-63303-3.00032-8. url: https://www.sciencedirect.com/science/article/pii/B9780444633033000328.

[4] W. Beckman. *Crystallization - Basic Concepts and Industrial Applications*. Wiley-VCH, 2013, pp. 1–14.

[5] W. Moerman, M. Carballa, A. Vandekerckhove, D. Derycke, and W. Verstraete. “Phosphate removal in agro-industry: Pilot- and full-scale operational considerations of struvite crystallization”. In: *Water Research* 43.7 (2009), pp. 1887–1892. doi: https://doi.org/10.1016/j.watres.2009.02.007.

[6] M. L. Ovecoglu, B. Kuban, and H. Ozer. “Characterization and Crystallization Kinetics of a Diopside-Based Glass-Ceramic Developed from GlassIndustry Raw Materials”. In: *Journal of European Ceramic Society* 7.17 (1997), pp. 957–962. doi: https://doi.org/10.1016/S0955-2219(96)00200-2.

[7] C. D. Doan, I. Tavernier, P. K. Okuro, and K. Dewettinck. “Internal and external factors affecting the crystallization, gelation and applicability of wax-based oleogels in food industry”. In: *Innovative food science & Emerging Technologies* 45 (2018), pp. 42–52. doi: http://dx.doi.org/10.1016/j.ifset.2017.09.023.

[8] M. Giulietti, M. M. Seckler, S. Derenzo, M. I. Ré, and E. Cekinsk. “Industrial Crystallization and Precipitation from Solutions: State of the Technique”. In: *Brazilian Journal of Chemical Engineering* 18.4 (2001), pp. 423–440. doi: http://dx.doi.org/10.1590/S0104-66322001000400007.

[9] D. Erdemir, A. Y. Lee, and A. S. Myerson. “Nucleation of Crystals from Solution: Classical and Two-Step Models”. In: *Accounts of Chemical Research* 42.5 (Apr. 2009), pp. 621–629. doi: 10.1021/ar800217x.

[10] D. Chakraborty and G. N. Patey. “How crystals nucleate and grow in aqueous NaCl solution”. In: *Journal of Physical Chemistry Letters* 4.4 (2013), pp. 573–578. issn: 1948-7185. doi: 10.1021/jz302065w. url: https://doi.org/10.1021/jz302065w.

[11] J. F. Lutsko and J. Lam. “Classical density functional theory, unconstrained crystallization, and polymorphic behavior”. In: *Physical Review E* 98.1 (2018). issn: 24700053. doi: 10.1103/PhysRevE.98.012604. arXiv: 1805.05673.

[12] P. G. Vekilov. “Nucleation of protein crystals”. In: *Progress in Crystal Growth and Characterization of Materials* 62.2 (June 2016), pp. 136–154. issn: 0960-8974. doi: 10.1016/J.PCRYSGROW.2016.04.007. url: https://www.sciencedirect.com/science/article/pii/S0960897416300109.

[13] T. Nakamuro, M. Sakakibara, H. Nada, K. Harano, and E. Nakamura. “Capturing the Moment of Emergence of Crystal Nucleus from Disorder”. In: *Journal of the American Chemical Society* 143.4 (2021), pp. 1763–1767. issn: 15205126. doi: 10.1021/jacs.0c12100.

[14] B. A. Garetz, J. E. Aber, N. L. Goddard, R. G. Young, and A. S. Myerson. “Nonphotochemical, Polarization-Dependent, Laser-Induced Nucleation in Supersaturated Aqueous Urea Solutions”. In: *Physical Review Letters* 77.16 (1996), pp. 3475–3476. url: https://link.aps.org/doi/10.1103/PhysRevLett.77.3475.

[15] A. J. Alexander and P. J. Camp. “Non-photochemical laser-induced nucleation”. In: *The Journal of Chemical Physics* 150.4 (2019), pp. 040901–99. doi: https://doi.org/10.1063/1.5079328.

[16] A. J. Alexander and P. J. Camp. “Single Pulse, Single Crystal Laser-Induced Nucleation of Potassium Chloride”. In: *Crystal Growth & Design* 9.2 (2009), pp. 958–963. doi: https://doi.org/10.1021/cg8007415.

[17] R. Kacker, S. Dhingra, D. Irimia, M. K. Ghatkesar, A. Stankiewicz, H. J. Kramer, and H. B. Eral. “Multiparameter Investigation of Laser-Induced Nucleation of Supersaturated Aqueous KCl Solutions”. In: *Crystal Growth and Design* 18.1 (2018), pp. 312–317. issn: 15287505. doi: 10.1021/acs.cgd.7b01277.

[18] D. Irimia, J. Jose Shirley, A. S. Garg, D. P. Nijland, A. E. Van Der Heijden, H. J. Kramer, and H. B. Eral. “Influence of Laser Parameters and Experimental Conditions on Nonphotochemical Laser-Induced Nucleation of Glycine Polymorphs”. In: *Crystal Growth and Design* 21.1 (2021), pp. 631–641. issn: 15287505. doi: 10.1021/acs.cgd.0c01415.

[19] J. Matic, X. Sun, B. A. Garetz, and A. S. Myerson. “Intensity, Wavelength, and Polarization Dependence of Nonphotochemical Laser-Induced Nucleation in Supersaturated Aqueous Urea Solutions”. In: *Crystal Growth & Design* 5.4 (June 2005), pp. 1565–1567. doi: 10.1021/cg050041c.

[20] A. Sun, B. A. Garetz, and A. S. Myerson. “Supersaturation and Polarization Dependence of Polymorph Control in the Nonphotochemical Laser-Induced Nucleation (NPLIN) of Aqueous Glycine Solutions”. In: *Crystal Growth & Design* 6.3 (2006), pp. 684–689. doi: https://doi.org/10.1021/cg050460+.

[21] X. Sun, B. A. Garetz, and A. S. Myerson. “Polarization switching of crystal structure in the nonphotochemical laser-induced nucleation of supersaturated aqueous L-histidine”. In: *Crystal Growth and Design* 8.5 (2008), pp. 1720–1722. issn: 15287483. doi: 10.1021/cg800028v.

[22] M. R. Ward and A. J. Alexander. “Nonphotochemical laser-induced nucleation of potassium halides: Effects of wavelength and temperature”. In: *Crystal Growth and Design* 12.9 (2012), pp. 4554–4561. issn: 15287483. doi: 10.1021/cg300750c.

[23] X. Sun, B. A. Garetz, M. F. Moreira, and P. Palffy-Muhoray. “Nonphotochemical laser-induced nucleation of nematic phase and alignment of nematic director from a supercooled thermotropic liquid crystal”. In: *Physical Review E - Statistical, Nonlinear, and Soft Matter Physics* 79.2 (2009), pp. 1–6. issn: 15393755. doi: 10.1103/PhysRevE.79.021701.

[24] M. R. Ward, S. McHugh, and A. J. Alexander. “Non-photochemical laser-induced nucleation of supercooled glacial acetic acid”. In: *Physical Chemistry Chemical Physics* 14.1 (2012), pp. 90–93. issn: 14639076. doi: 10.1039/c1cp22774b.

[25] B. C. Knott, J. L. Larue, A. M. Wodtke, M. F. Doherty, and B. Peters. “Communication: Bubbles, crystals, and laser-induced nucleation”. In: *Journal of Chemical Physics* 134.17 (2011), p. 171102. issn: 00219606. doi: 10.1063/1.3582897.

[26] M. R. Ward, W. J. Jamieson, C. A. Leckey, and A. J. Alexander. “Laser-induced nucleation of carbon dioxide bubbles”. In: *Journal of Chemical Physics* 142.14 (2015), p. 144501. issn: 00219606. doi: 10.1063/1.4917022. url: http://dx.doi.org/10.1063/1.4917022.

[27] I. S. Lee, J. M. Evans, D. Erdemir, A. Y. Lee, B. A. Garetz, and A. S. Myerson. “Nonphotochemical laser induced nucleation of hen egg white lysozyme crystal”. In: *Crystal Growth and Design* 8.12 (2008), pp. 4255–4261. issn: 15287483. doi: 10.1021/cg800696u.

[28] B. A. Garetz, J. Matic, and A. S. Myerson. “Polarization Switching of Crystal Structure in the Nonphotochemical Light-Induced Nucleation of Supersaturated Aqueous Glycine Solutions”. In: *Physical Review Letters* 89.17 (2002), p. 175501. url: https://link.aps.org/doi/10.1103/PhysRevLett.89.175501.

[29] W. Li, A. Ikni, P. Scouflaire, X. Shi, N. El Hassan, P. Gémeiner, J.-M. Gillet, and A. Spasojević-de Biré. “Non-Photochemical Laser-Induced Nucleation of Sulfathiazole in a Water/Ethanol Mixture”. In: *Crystal Growth & Design* 16.5 (2016), pp. 2514–2526. issn: 1528-7483. doi: 10.1021/acs.cgd.5b01526. url: http://dx.doi.org/10.1021/acs.cgd.5b01526.

[30] A. Ikni, B. Clair, P. Scouflaire, S. Veesler, J.-M. Gillet, N. El Hassan, F. Dumas, and A. Spasojević-de Biré. “Experimental Demonstration of the Carbamazepine Crystallization from Non-photochemical Laser-Induced Nucleation in Acetonitrile and Methanol”. In: *Crystal Growth & Design* 14.7 (2014), pp. 3286–3299. issn: 1528-7483. doi: 10.1021/cg500163c. url: http://dx.doi.org/10.1021/cg500163c.

[31] Y. Xiao, S. K. Tang, H. Hao, R. J. Davey, and T. Vetter. “Quantifying the Inherent Uncertainty Associated with Nucleation Rates Estimated from Induction Time Data Measured in Small Volumes”. In: *Crystal Growth & Design* 17.5 (2017), pp. 2852–2863. doi: https://doi.org/10.1021/acs.cgd.7b00372.

[32] B. Clair, A. Ikni, W. Li, P. Scouflaire, V. Quemener, and A. Spasojevic-de Bire. “A new experimental setup for high-throughput controlled non-photochemical laser-induced nucleation: application to glycine crystallization”. In: *Journal of Applied Crystallography* 47 (2014), pp. 1252–1260. doi: https://doi.org/10.1107/S160057671401098X.

[33] A. M. Ganan-Calvo, J. M. Mantanero, L. Martin-banderas, and M. Flores-mosquera. “Building functional materials for health care and pharmacy from microfluidic principles and Flow Focusing”. In: *Advanced Druge Delivery Reviews* 65.11-12 (2013), pp. 1447–1469. doi: https://doi.org/10.1016/j.addr.2013.08.003.

[34] Q. Feng, J. Sun, and X. Jiang. “Microfluidics-mediated assembly of functional nanoparticles for cancer-related pharmaceutical applications”. In: *Nanoscale* 8 (2016), pp. 12430–12443. doi: https://doi.org/10.1039/C5NR07964K.

[35] S. Sigiura, T. Oda, Y. Izumida, Y. Aoyagi, M. Satake, A. Ochiai, Y. Ohkohchi, and M. Nakajima. “Size control of calcium alginate beads containing living cells using micro-nozzle array”. In: *Biomaterials* 26.16 (2005), pp. 3327–3331. doi: https://doi.org/10.1016/j.biomaterials.2004.08.029.

[36] L. H. Hung, K. M. Choi, W. Y. Tseng, Y. C. Tan, K. J. Shea, and A. P. Lee. “Alternating droplet generation and controlled dynamic droplet fusion in microfluidic device for CdS nanoparticle synthesis”. In: *Lab on a Chip* 2 (2006), pp. 174–178. doi: https://doi.org/10.1039/B513908B.

[37] L. Frenz, A. El Harrak, M. Pauly, S. Begin-Colin, A. D. Griffiths, and J. C. Baret. “Droplet–Based Microreactors for the Synthesis of Magnetic Iron Oxide Nanoparticles”. In: *Angewandte Chemie International Edition* 47.36 (2008), pp. 6817–6820. doi: https://doi.org/10.1002/anie.200801360.

[38] B. Zheng, J. D. Tice, L. Spencer Roach, and R. F. Ismagilov. “A Droplet–Based, Composite PDMS/Glass Capillary Microfluidic System for Evaluating Protein Crystallization Conditions by Microbatch and Vapor–Diffusion Methods with On–Chip X–Ray Diffraction”. In: *Angewandte Chemie International Edition* 43.19 (2004), pp. 2508–2511. doi: https://doi.org/10.1002/anie.200453974.

[39] J. Ferreira, F. Castro, F. Rocha, and S. Kuhn. “Protein crystallization in a droplet-based microfluidic device: Hydrodynamic analysis and study of the phase behaviour”. In: *Chemical Engineering Sciences* 191 (2018), pp. 232–244. doi: https://doi.org/10.1016/j.ces.2018.06.066.

[40] L. Li and R. F. Ismagilov. “Protein Crystallization Using Microfluidic Technologies Based on Valves, Droplets, and SlipChip”. In: *Annual Review of Biophysics* 39 (2010), pp. 139–158. doi: https://doi.org/10.1146/annurev.biophys.050708.133630.

[41] T. Hua, O. Gowayed, D. Grey-Stewart, B. A. Garetz, and R. L. Hartman. “Microfluidic Laser-Induced Nucleation of Supersaturated Aqueous KCl Solutions”. In: *Crystal Growth & Design* 19.6 (2019), pp. 3491–3497. doi: https://doi.org/10.1021/acs.cgd.9b00362.

[42] T. Hua, C. Valentin-Valentin, O. Gowayed, S. Lee, B. A. Garetz, and R. L. Hartman. “Microfluidic Laser-Induced Nucleation of Supersaturated Aqueous Glycine Solutions”. In: *Crystal Growth & Design* 20.10 (2020), pp. 6502–6509. doi: https://doi.org/10.1021/acs.cgd.0c00669.

[43] J. Zaccaro, J. Matic, A. S. Myerson, and B. A. Garetz. “Nonphotochemical, Laser-Induced Nucleation of Supersaturated Aqueous Glycine Produces Unexpected γ-Polymorph”. In: *Crystal Growth & Design* 1.1 (Nov. 2000), pp. 5–8. doi: 10.1021/cg0055171.

[44] J. F. Lutsko and G. Nicolis. “Theoretical Evidence for a Dense Fluid Precursor to Crystallization”. In: *Physical Review Letters* 96 (2006), pp. 046102–046102. doi: https://doi.org/10.1103/PhysRevLett.96.046102.

[45] A. M. Schwartz and A. S. Myerson. “1 - Solutions and solution properties”. In: *Handbook of Industrial Crystallization (Second Edition)*. Woburn: Butterworth-Heinemann, 2002, pp. 1–31. isbn: 978-0-7506-7012-8. doi: http://dx.doi.org/10.1016/B978-075067012-8/50003-3. url: http://www.sciencedirect.com/science/article/pii/B9780750670128500033.

[46] M. R. Ward, A. M. Mackenzie, and A. J. Alexander. “Role of Impurity Nanoparticles in Laser-Induced Nucleation of Ammonium Chloride”. In: *Crystal Growth & Design* 16.12 (2016), pp. 6790–6796. doi: https://doi.org/10.1021/acs.cgd.6b00882.

[47] Y. M. Harshe, M. J. van Eijk, C. R. Kleijn, M. T. Kreutzer, and P. E. Boukany. “Scaling of mixing time for droplets of different sizes traveling through a serpentine microchannel”. In: *RSC Advances* 6.101 (2006), pp. 98812–98815. doi: https://doi.org/10.1039/c6ra17728j.

[48] S. D. Shingte, O. Altenburg, P. J. T. Verheijen, H. J. M. Kramer, and H. B. Eral. “Microfluidic Platform with Serpentine Geometry Providing Chaotic Mixing in Induction Time Experiments”. In: *Crystal Growth & Design* 22.7 (June 2022), pp. 4072–4085. doi: 10.1021/acs.cgd.1c01436.

[49] See Supplementary Information at [URL will be inserted by publisher] for hydrophobization protocol, droplet characterization results, estimation of cooling length and other miscellaneous details. 2023.

[50] L. Li and R. F. Ismagilov. “Protein Crystallization Using Microfluidic Technologies Based on Valves, Droplets, and SlipChip”. In: *Annual Review of Biophysics* 39 (2010), pp. 139–158. doi: https://doi.org/10.1146/annurev.biophys.050708.133630.

[51] J. Ferreira, F. Castro, F. Rocha, and S. Kuhn. “Protein crystallization in a droplet-based microfluidic device: Hydrodynamic analysis and study of the phase behaviour”. In: *Chemical Engineering Sciences* 191 (2018), pp. 232–244. doi: https://doi.org/10.1016/j.ces.2018.06.066.

[52] B. M. A. Wolffenbuttel, T. A. Nijhuis, A. Stankiewicz, and J. A. Moulijn. “Novel method for non-intrusive measurement of velocity and slug length in two- and three-phase slug flow in capillaries”. In: *Measurement Science and Technology* 13.10 (2002), pp. 1540–1544. doi: https://doi.org/10.1088/0957-0233/13/10/305.

[53] A. M. Ganan-Calvo, J. M. Mantanero, L. Martin-banderas, and M. Flores-mosquera. “Building functional materials for health care and pharmacy from microfluidic principles and Flow Focusing”. In: *Advanced Druge Delivery Reviews* 65.11-12 (2013), pp. 1447–1469. doi: https://doi.org/10.1016/j.addr.2013.08.003.

[54] E. C. dos Santos, A. Ładosz, G. M. Maggioni, P. Rudolf von Rohr, and M. Mazzotti. “Characterization of shapes and volumes of droplets generated in PDMS T-junctions to study nucleation”. In: *Chemical Engineering Research and Design* 138 (2018), pp. 444–457. issn: 02638762. doi: 10.1016/j.cherd.2018.09.001. url: https://doi.org/10.1016/j.cherd.2018.09.001.

[55] R. Grossier and S. Veesler. “Reaching One Single and Stable Critical Cluster through Finite-Sized Systems”. In: *Crystal Growth & Design* 9.4 (2009), pp. 1917–1922. doi: https://doi.org/10.1021/cg801165b.

[56] K. Fang, S. Arnold, and B. A. Garetz. “Nonphotochemical Laser-Induced Nucleation in Levitated Supersaturated Aqueous Potassium Chloride Microdroplets”. In: *Crystal Growth & Design* 14.5 (2014), pp. 2685–2688. doi: https://doi.org/10.1021/cg5004319.

[57] S. Wallis. “Binomial Confidence Intervals and Contingency Tests: Mathematical Fundamentals and the Evaluation of Alternative Methods”. In: *Journal of Quantitative Linguistics* 20.3 (July 2013), pp. 178–208. doi: 10.1080/09296174.2013.799918.

[58] R. Georgiev, S. Toscano, W. Uspal, B. Bet, S. Samin, R. Van Roij, and H. Eral. “Universal motion of mirror-symmetric microparticles in confined Stokes flow”. In: 2023. doi: /10.1073/pnas.2005068117.

[59] N. Nagalingam, A. Raghunathan, V. Korede, E. F. Overmars, S.-T. Hung, R. Hartkamp, J. T. Padding, C. S. Smith, and H. B. Eral. “Low-cost fluorescence microscope with microfluidic device fabrication for optofluidic applications”. In: *HardwareX* 14 (June 2023), e00415. doi: 10.1016/j.ohx.2023.e00415.

[60] G. M. Hale and M. Querry. “Optical Constants of Water in the 200-nm to 200-μm Wavelength Region”. In: *Applied Optics* 12.3 (1973), pp. 555–563. doi: https://doi.org/10.1364/AO.12.000555.

[61] R. D. Peters and S. D. Noble. “Using near infrared measurements to evaluate NaCl and KCl in water”. In: *Journal of Near Infrared Spectroscopy* 27.2 (2019), pp. 147–155. issn: 17516552. doi: 10.1177/0967033518821834.

[62] R. M. Pope and E. S. Fry. “Absorption spectrum (380–700 nm) of pure water II Integrating cavity measurements”. In: *Applied Optics* 36.33 (Nov. 1997), p. 8710. doi: 10.1364/ao.36.008710.

[63] N. Hidman, G. Sardina, D. Maggiolo, H. strom, and S. Sasic. “Numerical Frameworks for Laser-Induced Cavitation: Is Interface Supersaturation a Plausible Primary Nucleation Mechanism?” In: *Crystal Growth & Design* 20.11 (2020), pp. 7276–7290. doi: https://doi.org/10.1021/acs.cgd.0c00942.

[64] B. C. Knott, J. L. LaRue, A. M. Wodtke, A. M. Doherty, and B. Peters. “Communication: Bubbles, crystals, and laser-induced nucleation”. In: *The Journal of Chemical Physics* 134.17 (2011), pp. 171102–171102. doi: https://doi.org/10.1063/1.3582897.

[65] C. Li. *Nonlinear Absorption and Refraction of Light. In: Nonlinear Optics*. Vol. 1. Springer, 2017, pp. 177–214. doi: https://doi.org/10.1007/978-981-10-1488-8_7.

[66] N. Javid, T. Kendall, I. S. Burns, and J. Sefcik. “Filtration Suppresses Laser-Induced Nucleation of Glycine in Aqueous Solutions”. In: *Crystal Growth & Design* 16.8 (July 2016), pp. 4196–4202. doi: 10.1021/acs.cgd.6b00046.

[67] V. Korede, N. Nagalingam, F. M. Penha, N. van der Linden, J. T. Padding, R. Hartkamp, and H. B. Eral. “A Review of Laser-Induced Crystallization from Solution”. In: *Crystal Growth & Design* 23.5 (Apr. 2023), pp. 3873–3916. doi: 10.1021/acs.cgd.2c01526.

[68] N. Nagalingam, A. Raghunathan, V. Korede, C. Poelma, C. S. Smith, R. Hartkamp, J. T. Padding, and H. B. Eral. “Laser-Induced Cavitation for Controlling Crystallization from Solution”. In: *Physical Review Letters* 131.12 (Sept. 2023). issn: 1079-7114. doi: 10.1103/physrevlett.131.124001.

[69] J. M. Zook, V. Rastogi, R. I. MacCuspie, A. M. Keene, and J. Fagan. “Measuring Agglomerate Size Distribution and Dependence of Localized Surface Plasmon Resonance Absorbance on Gold Nanoparticle Agglomerate Size Using Analytical Ultracentrifugation”. In: *ACS Nano* 5.10 (Sept. 2011), pp. 8070–8079. doi: 10.1021/nn202645b.

[70] J. Kardum, A. Sander, and A. Glasnoviae. “Batch Crystallization of KCl: the Influence of the Cooling and Mixing Rate on the Granulometric Properties of Obtained Crystals”. In: *Chemical and Biochemical Engineering Quarterly* 19 (Mar. 2005).

[71] A.-C. Cheng, H. Masuhara, and T. Sugiyama. “Evolving Crystal Morphology of Potassium Chloride Controlled by Optical Trapping”. In: *The Journal of Physical Chemistry C* 124.12 (Mar. 2020), pp. 6913–6921. doi: 10.1021/acs.jpcc.9b11651.

4

INFLUENCE OF NANOPARTICLE PROPERTIES ON NON-PHOTOCHEMICAL LASER-INDUCED NUCLEATION

In non-photochemical laser-induced nucleation (NPLIN), a nanosecond laser pulse triggers rapid nucleation in supersaturated solutions, a process that would typically take days or weeks to occur naturally. Previous studies have shown that the introduction of nanoparticles into these supersaturated solutions enhances the probability of NPLIN when measured at a fixed time lag, compared to control experiments without nanoparticles. However, the precise mechanisms driving this enhancement remain unclear. In this study, we systematically investigate how the properties of added nanoparticles—specifically their concentration and chemical composition—affect the NPLIN probability in supersaturated urea solutions. We found that filtering the supersaturated urea solutions before irradiation reduced the NPLIN probability, while the addition of gold nanoparticles (AuNPs) to these filtered solutions significantly increased it, consistent with earlier reports. Additionally, we observed that higher laser intensities at a fixed AuNP concentration resulted in elevated NPLIN probabilities. Similarly, increasing the concentration of AuNPs at a fixed laser intensity also led to higher NPLIN probabilities. When comparing the effects of gold and silica nanoparticles of the same size and concentration, the gold-doped solutions exhibited greater NPLIN probabilities. We interpret these experimental results in light of the impurity heating hypothesis, which has been proposed to explain NPLIN. Our findings offer new insights into the factors influencing NPLIN and underscore the importance of

This chapter is based on Pingping Cui, Vikram Korede, Pepijn van Tooren, Nagaraj Nagalingam, Runze Wang, Qiuxiang Yin, Antoine E.D.M. van der Heijden, Herman J.M. Kramer, and Hüseyin Burak Eral (Submitted)

nanoparticle characteristics in the design of heteronucleants optimized for NPLIN applications.

4.1. INTRODUCTION

Non-photochemical laser induced nucleation (NPLIN) employs nanosecond laser pulses to initiate nucleation in supersaturated solutions without causing any detectable photochemical reaction, as neither the solute nor the solvent molecules absorb light at the irradiated wavelength [1, 2]. Since its discovery by Garetz *et al.* in 1996 using urea [3], NPLIN has been applied to crystallize over forty compounds, including small organic molecules [4], proteins and inorganic salts[5]. NPLIN reduces the induction time for supersaturated solutions from weeks to mere minutes or seconds[6, 7]. Moreover, NPLIN has been reported to offer control over crystal morphology[8] and (pseudo)polymorphic forms[9, 10]. More recently, NPLIN has also been used for cocrystal crystallization [11]. Despite these advances, a comprehensive physical understanding of NPLIN remains elusive[5].

Initial studies of NPLIN attributed to the interaction between the laser electric field and dipole moment of solute molecules, according to the Optical Kerr effect (OKE) [3]. This hypothesis suggests that the electric field of pulsed laser light induces anisotropic polarization, producing a weak torque that aligns the most polarizable axis of the molecule in the direction of the applied electric field. Furthermore, for aqueous glycine solutions, it was observed that the linear and circular polarization of light produced a different electric field, which altered the structural motifs of the crystal formed[12].

Subsequent studies, however, have demonstrated that crystal orientation does not depend on the direction of the electric field [13], and there appears to be no definitive correlation between the glycine polymorphism and the laser polarization [9, 14]. Interestingly, Irimia et al. reported the polymorphic form crystallizing from solution with NPLIN was different than the one nucleating during flash cooling [9]. Monte Carlo simulations suggest that the intensities of the lasers used in experiments are too low to induce nucleation via orientational bias [15]. As a result, an alternative mechanism, dielectric polarization (DP), has been proposed [16]. This mechanism considers the isotropic electronic polarizability of molecular clusters. According to this theory, the optical electric field could decrease the free energy within the clusters due to the difference in the dielectric permittivity between the solute and the solvent [5], thus reducing the size of the critical nucleus required for nucleation [16]. Although the DP model has been successful in correlating nucleation probability with peak laser intensity and solution supersaturation, it fails to explain the influence of laser pulse duration and threshold intensity on nucleation. Knott *et al.*[17] demonstrated

that while a laser could induce CO_2 bubble nucleation in carbonated water, this phenomenon could not be adequately explained by the DP mechanism.

Interestingly, the nucleation probability in filtered solutions, such as those of glycine, NH_4Cl, KCl, was lower than in unfiltered solutions under same laser irradiation conditions, indicating the significant role of either insoluble impurity nanoparticles or clusters in NPLIN [9, 18, 19]. However, this effect of filtration could be reversed by adding iron-oxide (Fe_3O_4) nanoparticles to filtered NH_4Cl samples [19]. Consequently, the nanoparticle heating mechanism was proposed as a third alternative mechanism for NPLIN, based on empirical evidence. This mechanism posits that impurity nanoparticles in the solution are heated by the laser, causing the surrounding liquid to vaporize and form bubbles. The evaporation of solvent around these bubbles is hypothesized to facilitate nucleation. Despite efforts to visualize the hypothesized bubbles in NPLIN experiments, no experimental evidence could be acquired. Using numerical simulations and inspired by experimental data from Soare *et al.*[20], Hidman *et al.* [21] built a numerical framework suggesting evaporation of solvent around the bubble increases local supersaturation hence triggering nucleation [21]. Since dedicated experiments were unavailable when Hidman *et al.* [21] published their results, it was not possible to verify the finite element simulations with experimental data. In other words, there was a lack of experimental evidence to support the hypothesized evaporation of a bubble around an impurity. To address this issue, Nagalingam *et al.*[22] used high-speed video microscopy to record bubble expansion and collapse followed by nucleation of KCl crystals and used numerical simulations to quantify the solute concentration around the bubble. These experiments were possible due to two significant changes introduced in the experimental settings, namely addition of ppm level soluble impurity, $KMnO_4$ and switching to an experimental geometry facilitating easy optical access essential for high speed microscopy. They observed a temporary peak (O(μs)) in local supersaturation at the vapor-liquid interface during rapid bubble expansion[22]. By combining high speed microscopy with finite element simulations, Nagalingam *et al.*[22] provided the first verified experimental evidence suggesting that thermocavitation bubbles forming in NPLIN experiments might trigger nucleation. Furthermore, Korede *et al.*[7] observed that adding Fe_3O_4 nanoparticles to filtered KCl samples not only increased the nucleation probability, but also altered the crystal morphology from cubic to needle-like in a droplet-based microfluidic system. The study by Briard *et al.*[23] on aqueous solutions of ethylenediamine sulfate (EDS) further investigates the hypothesis of nanoparticle heating, exploring the role of solid impurities in NPLIN and their potential in modulating nucleation probabilities.

In summary, impurity heating hypothesis appear to explain trends observed in NPLIN experiments that Optical Kerr effect and DP hypothesis can not explain[5]. However, the interaction of laser pulses with impurity nanoparticles and how the nature of the nanoparticles—such as material and concentration—affect NPLIN remain largely unexplored. Therefore, further experiments and detailed studies are required to better understand the role of nanoparticles in inducing NPLIN.

The primary objective of this study is to gain more experimental evidence for impurity heating mechanism in NPLIN and to investigate the influence of nanoparticle characteristics on the NPLIN probability. Experiments were conducted using supersaturated urea solution (S = 1.5) with 50 nm gold nanoparticles (AuNPs) of various concentrations and 50 nm silica nanoparticles at a laser wavelength of 532 nm. AuNPs were chosen as a result of their higher chemical stability and more frequent usage in such applications. Additionally, Au NPs are known for their unique optical properties, particularly their strong absorption in the visible light spectrum, which is expected to enhance the laser-impurity interaction[24].

4.2. EXPERIMENTAL

4.2.1. MATERIALS AND METHOD

Urea (molecular biology grade: 98.5-101.5%, CAS: 7447-40-7) and Au NPs dispersed in phosphate buffered saline (PBS) with 50 nm (SKU 753645, 3.5×10^{10} NPs/ml), were procured from Sigma Aldrich, Netherlands. Silica nanospheres with a diameter of 50 nm (10 mg/ml $\approx 7.64\times10^{10}$ NPs/ml), dispersed in Milli-Q water, was obtained from Alpha Nanotech Inc. Thiol-functionalized methoxyl polyethylene glycol (PEG-SH) with a molecular weight of 5000 Da was obtained from Rapp Polymere GMBH, Germany. Ultrapure water, from an internal Milli-Q system (ELGA Purelab, UK, 18.2 MΩ.cm), was used in all experiments.

Urea solution (30.2 mol kg^{-1}, S = 1.5) was prepared by dissolving urea in ultrapure water. This solution was placed in an ultrasonic heating water bath for 1 hour, then transferred to an oven set at 50°C overnight to ensure complete dissolution. The solution was then directly filtered into preheated 8 ml borosilicate glass vials using 0.22 μm (PTFE syringe filter). The vials were maintained at 50°C during this process. For each experimental set, 100 samples were prepared. After filtration, the vials were transferred to a 50°C water bath, gradually cooled to 25°C for 3 hours and aged for a day before laser exposure. Samples showing spontaneous nucleation prior to laser experiments were excluded from the study.

4.2.2. FILTERED SOLUTIONS DOPED WITH NANOPARTICLES

50 NM GOLD NANOPARTICLES

Urea supersaturated solutions with different concentrations were prepared, doped with various concentrations of 50 nm AuNPs to maintain a consistent supersaturation level (S=1.5). Detailed information on the specific concentrations of the urea solutions, the volume of the PEG-AuNPs suspension added, and the consequent concentrations of the AuNPs can be found in the Table 4.1. Additionally, the use of different concentrations of nanoparticles was instrumental in understanding the effect of nanoparticle concentration on the nucleation probability.

Table 4.1.: Summary of Urea Concentrations with corresponding volumes and concentrations of Doped PEG-AuNPs

Urea solution concentration (mol kg^{-1})	**Volume of PEG-AuNPs suspension added (ml)**	**Concentration of AuNPs (particles/ml)**
30.337	0.02	1.74×10^8
30.488	0.04	3.47×10^8
30.639	0.06	5.17×10^8
30.790	0.08	6.86×10^8
31.318	0.15	1.27×10^9

4.2.3. LASER IRRADIATION EXPERIMENTS

Figure 4.1 depicts the schematic of the experimental setup that includes Q-switched Nd:YAG laser (Continuum, Powerlite DLS8000), which emits 7 ns pulses of linearly polarized light with a wavelength of 532 nm at a frequency of 10 Hz.

The direction of light was adjusted by a mirror (NB1-K13, Thorlabs) or a beam splitter (BSN10, Thorlabs), according to the desired intensity levels. Subsequently, the fundamental beam, with a diameter of 9 mm, was passed through a Galilean telescope, resulting in a decrease in its diameter to 4.5 mm. To eliminate any artifacts produced by the laser, an iris was used. Before irradiating the samples through its center, the average energy per pulse was determined by averaging the measurements from 20 pulses using an energy meter (QE25LP-H-MB-QED-D0, Gentec EO). Each sample, free from spontaneous nucleation, was subjected to a single pulse of laser light at various intensities (10, 50, 100, 200, and 376 MW/cm^2). Immediately following the laser exposure, the sample was returned to the water bath set at 25°C. The presence of crystals in the vials was examined after 60-minutes, considering prior studies[18]. The nucleation probability, denoted as

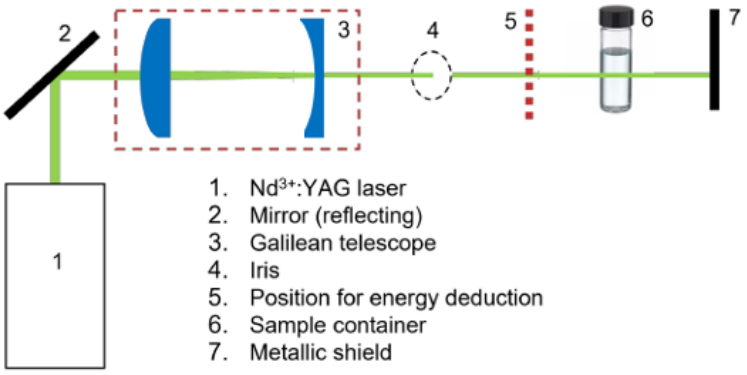

Figure 4.1.: A schematic of the experimental setup

P(t_{obs} = 60 min), was then calculated as the ratio of nucleated samples to the overall number of samples irradiated.

4.2.4. DYNAMIC LIGHT SCATTERING (DLS) TESTS

Dynamic Light Scattering (DLS) analysis were performed using a Zetasizer Pro (Malvern Panalytical Ltd, UK) to determine the particle size distribution (PSD) of filtered solution, unfiltered solution, and filtered urea solution doped with AuNPs. DLS measurements were conducted at 25°C using a 633 nm wavelength laser at a scattering angle of 173°. The non-negative least squares (NNLS) fitting algorithm was employed for calculating PSDs. To avoid urea crystallization during DLS tests, the solution concentration was kept at 16.65 mol kg^{-1} (S = 0.98). It is important to note that the PSD obtained from DLS represents the hydrodynamic diameter, which may not precisely correspond to the physical size of the nanoparticles.

4.3. RESULTS

4.3.1. EFFECT OF FILTRATION AND DOPING

Laser-induced nucleation experiments were performed with supersaturated filtered urea solution (S = 1.5) doped with PEG coated AuNPs (50 nm nominal diameter, 6.86 × 10^8 NPs/ml), at an incident wavelength of 532 nm and peak intensity of 376 MW/cm^2 to determine if addition of nanoparticles can enhance NPLIN nucleation probability by laser-impurity interaction. The nucleation probabilities obtained in these experiments are shown in the Figure 4.2A.

The unfiltered solution showed a nucleation probability of 22%, significantly higher than the 4% in filtered samples, highlighting the role

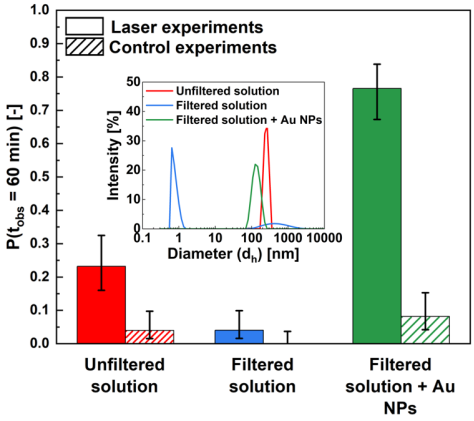

Figure 4.2.: (A) Comparison of nucleation probabilities for unfiltered, filtered and filtered solutions with addition of AuNPs (50 nm; d_m) under S = 1.5 in both control & laser experiments at a laser wavelength (532 nm) and laser peak intensity (376 MW/cm^2). The inset figure represents particle size distribution, reflecting the hydrodynamic diameter (d_h) obtained for unfiltered, filtered, and doped solutions with addition of AuNPs (concentration of 6.86 × 10^8 NPs/ml). The error bars are computed using the Wilson score method.

of nanoimpurities in NPLIN. Control samples exposed to air without laser showed minimal nucleation, corroborating unpublished observations by Ward[19] and Liu [13]. Doping with 50 nm gold nanoparticles increased the nucleation probability to 73% post-laser irradiation, compared to 12% in control samples. This enhancement is consistent with NPLIN studies on ammonium chloride and potassium chloride solutions [7, 19], supporting the hypothesis that gold nanoparticles reverse the effects of filtration in NPLIN studies.

To validate these experimental results, additional experiments were carried out using dynamic light scattering (DLS) to estimate the particle size distributions (PSD) in urea solutions, as shown in Figure 4.2B. Measurements were conducted on unfiltered urea solutions, filtered urea solutions, and urea solutions doped with AuNPs. The PSD curve of the unfiltered urea solution revealed a dominant peak at 260 ± 40 nm, likely due to nanoparticle impurities or clusters. Filtration almost completely removed the species at 260 ± 40 nm from the solution, leaving only a residual population peak smaller than 1 nm. Similar observations have been reported for filtered solutions of KCl and NH_4Cl, where particle populations were also ≤ 1 nm, attributed to the scattering of solute molecules rather than actual particles in solution[7, 19]. On the contrary, the filtered urea solution doped with 50 nm AuNPs

(denoted as d_m) exhibited a population size of approximately 120 ± 20 nm, indicative of the hydrodynamic diameter (d_h). This measurement suggests that the gold nanoparticles are slightly agglomerated within the solution. As a result, it may not be precise to consider agglomerated particles as individual entities due to the complexities introduced by agglomeration. This phenomenon alters various properties of the nanoparticles, including their optical characteristics[25]. However, for our analysis, AuNPs are treated based on the size provided by the manufacturer. This assumption is a limitation that must be considered when interpreting the results of our study, as the actual behavior of agglomerated nanoparticles could differ from that of well- dispersed, individual nanoparticles. Despite extensive efforts to optimize the dispersion of gold nanoparticles (AuNPs) within the urea solution, the level of dispersion achieved in our experiments represents the best possible outcome under the given experimental conditions.

The increase in nucleation probability for doping solutions can be attributed to the specific absorption efficiency of gold nanoparticles when exposed to 532 nm laser light. This efficiency, which depends on the size of the nanoparticles, is critically enhanced by the pronounced surface plasmon resonance (SPR) of gold nanoparticles. The absorption cross-section (C_{abs}), quantifying this efficiency, leads to increased localized heating around the nanoparticles, a key factor in initiating the nucleation process. This absorbed energy likely plays a pivotal role in creating the vapor bubbles observed during nucleation, reinforcing the hypothesis that localized heating around gold nanoparticles is instrumental in driving nucleation events. Quantitative details regarding the absorption relative to the size of the gold nanoparticles are provided in the Appendix C section C.2. For accurate calculations of absorption coefficients, using Mie theory, the true size of the gold nanoparticles was used.

In light of recent studies on the influence of metallic nanoparticle doping in increasing NPLIN efficiency [23], our observations with gold nanoparticles suggest that similar mechanisms may be at play. Studies have shown that doping with metallic particles significantly enhances nucleation probabilities in supersaturated EDS solutions. In our case, the strong absorption capabilities of gold nanoparticles due to SPR likely contributed to a similar enhancement in urea solutions, underscoring the critical role of metallic nanoparticles in the NPLIN mechanism.

4.3.2. EFFECT OF LASER INTENSITY ON NPLIN

Figure 4.3 shows the nucleation probability of filtered urea samples containing 50 nm AuNPs (6.86×10^8 NPs/ml) at various laser intensities (50, 100, 200, and 376 MW/cm^2). The nucleation probabilities observed at 10 MW/cm^2 overlapped with the control experiments, which did

not involve laser irradiation. However, with increasing laser intensity, nucleation probabilities also increased, reaching 73% at an intensity of 376 MW/cm^2.

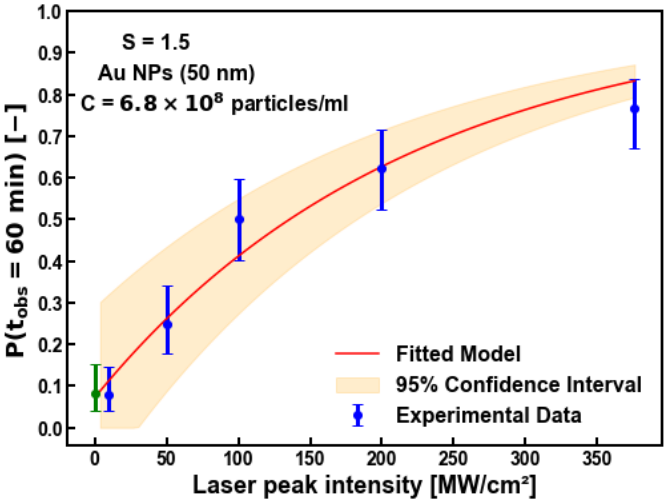

Figure 4.3.: Nucleation probability of filtered urea solution containing AuNPs (50 nm) under different laser intensities. The green data point corresponds to control experiment. The particle concentration in urea solution is 6.86 × 10^8 NPs/ml. Error bars are computed using the Wilson's score method.

At this stage, the experimental data was fitted to a curve representing Poisson distribution, as described by equation 4.1.

$$P(m) = \frac{N^m}{m!} e^{-N} \tag{4.1}$$

Where $P(m)$ is the probability of obtaining m nuclei in a sample and N is the average number of nuclei produced by the laser.

Since the total probability is equal to unity, the probability of having at least 1 nucleus in the sample can than be given by equation 4.2

$$P(t_{obs}; m \geq 1) = 1 - P(0) = 1 - e^{-N} \tag{4.2}$$

The average number of nuclei (N) formed over observation time t_{obs} can than be described in terms of nucleation rate per unit time (k) given by equation 4.3.

The average number of nuclei (N) can be obtained from the following equation:

$$\int_0^N dN = \int_0^{t_{obs}} k dt \tag{4.3}$$

Effectively the nucleation rate per unit time (k) includes contribution from spontaneous nucleation rate (k_0) for laser intensity (I) below a certain threshold laser intensity (I_0) and from laser-induced nucleation rate ($f(I)$) when the laser intensity exceeds the threshold intensity as shown in equation 4.4. It is noteworthy to mention that spontaneous nucleation rate per unit time k_0 here specifically pertains to the filtered urea supersaturated solutions containing 50 nm AuNPs at a concentration (C_{const}) of 6.86×10^8 particles/ml.

$$k = \begin{cases} k_0 & \text{if } I \leq I_0 \\ f(I, C) & \text{if } I > I_0 \end{cases} \tag{4.4}$$

The laser-induced nucleation rate $f(I, C)$ can than be approximated as a linear function of the laser intensity I by limiting the expansion of its Taylor series to the first order.

$$f(I, C) \approx f(I = I_0, C = C_{\text{const}}) + \left.\frac{\partial f}{\partial I}\right|_{I=I_0, C=C_{\text{const}}} (I - I_0) \tag{4.5}$$

$$f(I) \approx k_0 + b(I - I_0) \tag{4.6}$$

Here, $b = \left.\frac{df}{dI}\right|_{I=I_0}$ is the laser-induced nucleation rate sensitivity to changes in the laser intensity.

Inserting form 4.6 into 4.4, one obtains:

$$k = \begin{cases} k_0 & \text{if } I \leq I_0 \\ k_0 + b(I - I_0) & \text{if } I > I_0 \end{cases} \tag{4.7}$$

Form 4.7 is not useful for integrating the nucleation rate k over a given observation time t_{obs}. Furthermore, since the final goal of this section is to derive an expression of probability of nucleation as a function of intensity, which can be used for curve fitting, an analytically smooth function is needed. A sigmoid function is a good approximation for the above problem. The sigmoid function can be defined as follows:

$$\sigma(x) = \frac{1}{1 + e^{-1000x}} \tag{4.8}$$

The sigmoid function defined above rapidly approaches 0 when $x < 0$ and rapidly approaches 1 when $x > 0$. The coefficient 1000

in the exponent specifically ensures this sharp transition. This characteristic makes the sigmoid function particularly suitable for modeling phenomena that exhibit a sudden change in behavior around a certain threshold value of x.

$$k \approx k_0 + b(I - I_0)\sigma(I - I_0) \tag{4.9}$$

Inserting equation 4.9 into equation 4.3 and integrating, gives

$$N = k_0 t_{obs} + b(I - I_0)\delta t\sigma(I - I_0) \tag{4.10}$$

In this equation 4.10, δt represents the pulse-width of the laser. It is essential to emphasize that the laser-induced contribution to the nucleation rate, depicted by $b(I - I_0)\delta t\sigma(I - I_0)$, is explicitly linked to the duration δt when the laser intensity is applied. The function $\sigma(I - I_0)$ serves as a switch that activates the laser-induced nucleation rate when the intensity I exceeds the threshold I_0, and becomes 0 otherwise. Therefore, during the intervals 0 to $t-$ and $t+$ to t_{obs}, where the laser intensity is not applied, $\sigma(I - I_0)$ becomes 0. This ensures the contribution of the laser-induced nucleation rate to N is precisely confined to the laser pulse duration.

Substituting equation 4.10 into equation 4.2 gives

$$P(t_{obs}; m \geq 1) = 1 - P(0) = 1 - e^{-k_0 t_{obs} + b(I - I_0)\delta t\sigma(I - I_0)} \tag{4.11}$$

$$P(t_{obs}) \approx 1 - e^{-k_0 t_{obs}} e^{-b(I - I_0)\delta t\sigma(I - I_0)} \tag{4.12}$$

Rewriting equation 4.11 as 4.12 and substituting $a_I = e^{-k_0 t_{\text{obs}}}$ and $m_I = b\delta t$

Finally equation 4.12 can be written as 4.13

$$P(t_{obs}) = 1 - a_I e^{-m_I(I - I_0)\sigma(I - I_0)} \tag{4.13}$$

This analysis allows us to express the nucleation probability, denoted as $P(t_{\text{obs}})$, as a function of laser intensity, defined by three key parameters: the intensity sensitivity factor m_I, spontaneous nucleation factor a_I and laser intensity threshold I_0. The intensity sensitivity factor m_I measures the degree of change in nucleation probability in response to variations in laser intensity I, while the spontaneous nucleation factor a_I refers to the baseline probability of nucleation events occurring independently of laser intensity. The laser intensity threshold $(I_o)_{\text{exp}}$ refers to the minimum threshold intensity above which laser heating of nanoparticles ideally forms a cavitation bubble that acts as nucleation site for crystallization. The fitting process resulted in an intensity sensitivity factor (m_I) of approximately $0.0045^{+0.0024}_{-0.0024}$ cm^2/MW, spontaneous nucleation factor (a_I) of $0.918^{+0.216}_{-0.216}$ and laser

intensity threshold of approximately $2.34^{+68.82}_{-2.34}$ MW/cm^2. Matic *et al.*[26] observed similar threshold values of approximately 20–60 MW/cm^2 using multiple laser pulses with unfiltered urea solutions.

Although the physical meaning of the sensitivity parameter m_I is not directly obvious at this point, a speculation on its meaning was made in the context of impurity heating mechanism. The sensitivity parameter m_I provides insight into the relationship between laser intensity and the mean crystal count. It represents how efficiently the laser intensity causes the solvent evaporation at the vapor/liquid interface leading to crystal formation. However, an exact description of m_I within this model in terms of fundamental laser and solution parameters requires more theoretical research and is outside the scope of this work.

The experimentally obtained laser intensity threshold is then compared with a theoretical value obtained using equation 4.14[27]. The equation described below is used to calculate the theoretical laser intensity threshold at which the nanoparticle temperature exceeds the boiling point of the surrounding liquid, leading to the formation of a vapor layer on the nanoparticle surface. This vapor layer experiences a rapid increase in pressure, resulting in the rapid expansion and subsequent formation of a cavitation bubble[27].

$$(I_o)_{\text{theo}} = \frac{4\pi R_{\text{np}} c_l \rho_l \gamma_l T_{\text{boil}}}{r_{\text{abs}}} \tag{4.14}$$

where, $(I_o)_{\text{theo}}$ represents the theoretical laser intensity threshold, $R_{\text{np}} = 25 \times 10^{-9}$ m (radius of the nanoparticle), $c_l = 2815.0$ J/(kg·K) (specific heat of the urea solution), $\rho_l = 1166.0$ kg/m^3 (density of the solution), $T_{\text{boil}} = 647.0$ K (boiling temperature), $r_{\text{abs}} = 7.92 \times 10^{-15}$ m^2 (absorption cross section), $\tau_L = 7 \times 10^{-9}$ s (pulse duration), and $\gamma_l = 1.83 \times 10^{-7}$ m^2/s (thermal diffusivity of the urea solution).

The theoretical laser intensity threshold of 1.54 MW/cm^2 was calculated under the assumption that only one nanoparticle, suspended in the solution, was irradiated by the laser[27, 28]. However, the discrepancy between this theoretical value and the higher experimental threshold of approximately $2.34^{+68.82}_{-2.34}$ MW/cm^2 is attributed to the background spontaneous crystallization, i.e., nucleation, in the control experiments. Improvements in the experimental procedure aimed at reducing this background spontaneous crystallization could potentially bring the experimental threshold values closer to the theoretical predictions.

In the context of this experiment, urea solution, with a total volume of 4 ml, contains a nanoparticle concentration of 6.86×10^8/ml. Assuming that the nanoparticles are homogeneously suspended throughout the sample volume, the energy absorbed by the nanoparticles is primarily used to evaporate the surrounding solvent molecules, thus aiding in the formation of cavitation bubbles. Consequently, crystallization could

occur due to an increase in the concentration of urea at the vapor/liquid interface[22, 29].

Drawing insights from Nagalingam *et al.*[22] and Hidman *et al.*[29], we hypothesize that the increase in incident laser intensity correlates with an increase in the size of bubbles formed around each nanoparticle. This hypothesis is based on the assumption that each nanoparticle produces a single bubble upon laser irradiation.

The energy absorbed by nanoparticles, crucial for bubble formation, can be quantified as $E_{\text{abs, P}} = Q_{\text{abs}}\pi R_p^2 I_{\text{eff}}\tau_L$, where Q_{abs} denotes the absorption efficiency, I_{eff} represents the effective laser intensity at the nanoparticle location, R_p is the nanoparticle radius, and τ_L is the pulse width of the laser [30].

Furthermore, the energy absorbed by the nanoparticles is utilized to evaporate the surrounding solvent molecules, facilitating the formation of cavitation bubbles, which can be approximated by the formula $E_{\text{abs, B}} \sim mh_l \sim \frac{3\pi}{4}R_{b,max}^3\rho_l h_l$, where m, h_l, and ρ_l represents mass, latent heat of vaporization, and density of the liquid, respectively, and R_b represents the maximum bubble radius[30]. Thus, the relationship between nanoparticle radius, effective laser intensity, and maximum bubble size is more precisely described by $R_{b,max} \propto (Q_{\text{abs}}R_p^2 I_{\text{eff}})^{1/3}$. Assuming a constant nanoparticle size and absorption coefficient, the maximum radius of the bubble, as theoretically predicted by Hidman *et al.*[29] and further corroborated by Nagalingam *et al.*[22] through a combined experimental and numerical approach, is expected to be significantly influenced by the local laser intensity at the nanoparticle sites.

In our experimental setup, the cylindrical curvature of our glass vial focuses the incident laser beam within the solution medium, as discussed in our previous article [31]. Moreover, the nanoparticles in the path of the laser beam absorb laser intensity, following the Beer-Lambert law. Hence, the effective intensity profile along the diameter of the vial is the result of the competition between the focusing effect induced by the cylindrical vial and the attenuation of intensity resulting from the absorption of the nanoparticles along the beam path.

At this stage, to account for the geometrical focusing effect alongside the absorption quantified by the Beer-Lambert law, the conventional absorbance equation is modified with an additional factor that represents the ratio of the beam area to the effective elliptical cross-sectional area within the vial. This elliptical cross-section arises because the cylindrical vial acts like a lens, focusing the beam in only one direction and thus transforming a circular beam into an ellipse, as elucidated in our previous article [31]. The revised expression for absorbance A, considering the focusing effect, is given by equation 4.15.

$$A = -\log_{10}\left(\frac{I_{\text{tra}}}{I_{\text{inc}}}\right) = \epsilon c l \cdot \frac{A_{\text{beam}}}{A_{\text{ellipse}}(x)} \tag{4.15}$$

Where A_{beam} is the area of the incident laser beam, given by $\pi \times R_{\text{beam}}^2$, calculated from the radius of the laser beam R_{beam} of 2.25 mm. The $A_{\text{ellipse}}(x)$ term represents the variable elliptical area at a position x along the vial, calculated as $\pi \times R_{\text{beam}} \times R_{\text{ellipse}}$,where R_{ellipse} at a position x in the vial is obtained from our previous article[31] and is included in the Appendix C section C.3. A is the absorbance, $I_{\text{inc}} = 376$ MW/cm^2 is the incident light intensity, I_{tra} is the transmitted light intensity, $\epsilon = 1.72 \times 10^9$ M^{-1}mm^{-1} is the molar extinction coefficient, which quantifies how strongly gold nanoparticles absorb light at a given wavelength (532 nm). This extinction coefficient is assumed constant across the range of diluted sample concentrations used in our experiments (from 8.75×10^6 to 1.26×10^9 particles/ml), justified by Sigma-Aldrich specification that it is valid up to 3.5×10^{10} particles/ml, $c = 1.11 \times 10^{-7}$ M (6.86×10^8 particles/ml) is the concentration of the absorbing species in the solution, and l is the path length at which the laser intensity significantly attenuates through the solution medium (in mm).

In our experiments, the absorption by nanoparticles causes a more significant reduction in the intensity of the laser light compared to the focusing effect of the cylindrical vial, which enhances it. This phenomenon is evident from the intensity profile graph presented along the diameter of the vial in the Appendix C section C.6, employing equation 4.15. As we increase the incident laser intensity from outside the vial, the effective intensity experienced by the nanoparticles in the path length also increases. This enhancement in effective intensity leads to larger bubble sizes and is expected to increase local supersaturation at the vapor-liquid interface. The increase in local supersaturation at the interface is likely to accelerate the nucleation process with increasing laser intensities, potentially explaining the higher nucleation probabilities observed[22, 29].

Furthermore the equation 4.15 can be used to determine the path length at which the intensity of light transmitted through a material is significantly reduced due to absorption. For practical reasons, the path length is calculated as the distance from the wall of the vial where the transmitted intensity drops to the sensitivity limit of the instrument (10^{-3} MW/cm^2).

It is noteworthy that the variation in the incident laser peak intensity at a constant concentration of AuNPs (50 nm: 6.86×10^8 particles/mL) led to minimal changes in the path length, as shown in Table 4.2. This observation implies that although increased laser intensity does enhance the energy absorbed per nanoparticle, utilized primarily for evaporating surrounding solvent molecules and facilitating in the formation of

cavitation bubbles, its overall impact on the path length appears to be less significant compared to the effects caused by changes in concentration of AuNPs (50 nm) for a fixed laser intensity, as further discussed in Section 4.3.3.

Table 4.2.: Summary of Laser Peak Intensities and the Corresponding Path Lengths in the Solution at a fixed Concentration of AuNPs (50 nm: (6.86×10^8 particles/ml)

Laser peak intensity (MW/cm^2)	**Path length (mm)**
10	0.021
50	0.025
100	0.026
200	0.028
376	0.030

The small path length numbers from Table 4.2 suggest that crystallization events, induced by the absorption of laser light by nanoparticles, occur predominantly near the glass-solution interface. To verify this, similar experiments with filtered urea solutions doped with AuNPs can be conducted using a high-speed camera to observe the locations of bubble formation and subsequent crystal formation within the glass vial following the laser shot through the glass/solution interface.

To further investigate the phenomena of preferential nucleation at the glass-solution interface, particularly in the context of laser-induced nucleation with nanoparticles, one promising approach could involve the deliberate attachment of nanoparticles to the glass surface through surface modification techniques prior to the laser induced nucleation experiments[32].

4.3.3. EFFECT OF IMPURITIES PROPERTIES ON NPLIN

Recent studies in NPLIN research, including those by Javid et al.[33], Ward et al.[19], Kacker et al.[18], and Korede et al.[7], have highlighted the crucial role of impurity nanoparticles within supersaturated solutions and their interaction with laser energy in influencing NPLIN probabilities. In light of these findings, this section investigates the effects of impurity properties such as concentration, size, and material composition on the NPLIN probabilities.

NANOPARTICLE CONCENTRATION

Figure 4.4A represents the nucleation probability of filtered urea samples containing 50 nm AuNPs at various nanoparticle concentrations. The

experiments were carried out at a laser wavelength of 532 nm and laser peak intensity of 376 MW/cm^2. It is evident from the Figure 4.4A that nucleation probability showed an overall increasing trend with increasing particle concentration. Similarly, control experiments, for different nanoparticle concentrations showed comparable nucleation probabilities within the observation time of 60 minutes. Our observations from Figure 4.4A indicate that within the nanoparticle concentration range of $(1.74 - 5.17) \times 10^8$ NPs/ml, the nucleation probabilities remain relatively stable, oscillating between 50% and 55%. A notable increase in nucleation probability, around 75%, is observed when concentration exceed 6.86×10^8 NPs/ml.

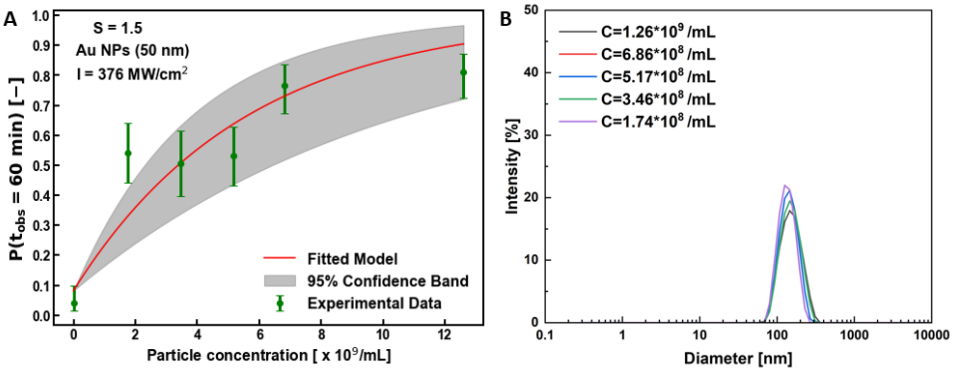

Figure 4.4.: (A) Nucleation probabilities of filtered urea solutions containing AuNPs (50 nm) with different nanoparticle concentration under S = 1.5 at a laser wavelength (532 nm) and laser peak intensity (376 MW/cm^2 and (B) Particle size distribution of filtered urea solutions with different nanoparticle concentration. Error bars are computed using the Wilson's score method.

At this stage, the experimental data was fitted to a curve representing Poisson distribution, as described by equation 4.1. Following the fitting process as described in the section 4.3.2 and from our experimental observations of nucleation probability increase with the nanoparticle concentration for a defined laser intensity, we can deduce that the sensitivity factor b is dependant on the nanoparticle concentration C. Specifically $b(C)$ can then be approximated as a linear function of the nanoparticle concentration C by limiting the expansion of its Taylor series to the first order.

$$b(C) \approx b(C = 0) + \left.\frac{db}{dC}\right|_{C=0} C \tag{4.16}$$

Equation 4.16 can be approximated as equation 4.17, for simplification

purpose and ease of calculations.

$$b(C) \approx yC \tag{4.17}$$

If a single nanoparticle acts as a absorption site for laser induced nucleation, $y = \frac{db}{dC}$ can be interpreted as the extent with which that nanoparticle can induce nucleation given laser intensity input beyond the threshold value I_0.

Substituting equation 4.17 into equation 4.12 gives the probability of nucleation at an observation time as a function of nanoparticle concentration in terms of poisson distribution.

$$P(t_{obs}) \approx 1 - e^{-k_0 t_{obs}} \times e^{-yC(I-I_0)\delta t \sigma (I-I_0)} \tag{4.18}$$

Incorporating the spontaneous nucleation factor a_I, derived from the curve fitting in Section 4.3.2, and substituting $m_C = y(I-I_0)\delta t\, \sigma(I-I_0)$ in equation 4.18 allows us to express nucleation probability by equation 4.19

$$P(t_{obs}) = 1 - a_I e^{-m_C C} \tag{4.19}$$

From this analysis, the equation of the fitted line describes the nucleation probability $P(\mathrm{t_{obs}})$ as a function of nanoparticle concentration, incorporating two critical parameters: the concentration sensitivity factor m_C and the spontaneous nucleation factor a_I. Since the control experiments for filtered urea solutions doped with different nanoparticle concentrations showed similar nucleation probabilities within an observation time ($\mathrm{t_{obs}}$) of 60 minutes (Appendix C section C.4), it can be inferred that the spontaneous nucleation rate remains relatively constant across the solutions with different nanoparticle concentrations. Consequently, a_I is obtained from the result of the curve fitting procedure of nucleation probability variation with laser intensity. The factor m_C measures the change in nucleation probability in response to varying nanoparticle concentrations. The fitting procedure yielded a concentration sensitivity factor of approximately $1.8^{+0.854}_{-0.854} \times 10^{-9}$ ml/particles.

The physical interpretation of the sensitivity parameter m_C is not immediately apparent. Speculation regarding its meaning has been made in the context of an impurity heating mechanism. m_C can be viewed as a measure of how effectively each nanoparticle converts absorbed laser energy into the localized heat necessary for crystallization, achieved through the evaporation of solvent molecules surrounding the nanoparticles. However, a precise description of m_C within this model, in terms of fundamental laser and solution parameters, requires further theoretical investigation, and lies beyond the scope of this study.

Additionally, higher concentrations of nanoparticles result in a shorter path length over which the light intensity is significantly attenuated, as indicated by the values in Table 4.3. Although the path length is reduced, the number of nanoparticles interacting with the laser within the path length remains relatively consistent (calculations in the Appendix C section C.5) across different AuNPs concentrations. Under these conditions, one might expect the nucleation probability to remain similar across different nanoparticle concentrations, since the energy absorbed by the nanoparticles—which leads to cavitation bubble formation and subsequent crystallization due to local supersaturation—is constant, as discussed in section 4.3.2. However, an increase in nucleation probability with increased nanoparticle concentration has been observed.

Table 4.3.: Summary of AuNP Concentrations and Corresponding Path Lengths in Solution at a Fixed Laser Peak Intensity of 376 MW/cm^2

Concentration of AuNPs (particles/ml)	**Path length (mm)**
1.74×10^8	0.115
3.47×10^8	0.058
5.17×10^8	0.039
6.86×10^8	0.030
1.27×10^9	0.016

This observation has been attributed to speculation surrounding the role of secondary nucleation processes, which are believed to occur after the initial crystallization, triggered by the absorption of laser light by nanoparticles within the path length. The resulting crystals may then interact with additional nanoparticles present beyond the path length, potentially facilitating further nucleation events. As nanoparticle concentration increases, the number of nanoparticles beyond the path length zone also increases, thereby enhancing the likelihood of such interactions. These interactions could contribute to the observed increase in nucleation probability with increase in AuNPs concentration observed in our experiments.

Further insights into particle dynamics were obtained from dynamic light scattering (DLS) curves, as illustrated in 4.4B. Regardless of concentration, filtered urea solutions with AuNPs (50 nm) of different nanoparticle concentrations displayed similar size peaks at approximately 120 $\pm$ 20 nm. This consistency in particle size across varying concentrations ensures that the observed effects on nucleation probability are predominantly due to changes in nanoparticle concentration rather than particle size or other physical characteristics.

NANOPARTICLE MATERIAL

To investigate the impact of impurity materials on NPLIN probability, experiments were carried out with filtered urea samples doped with 50 nm AuNPs and 50 nm silica nanoparticles, respectively. These experiments were performed at a laser wavelength of 532 nm and a peak laser intensity of 376 MW/cm^2. Figure 4.5A presents the nucleation probability of these doped urea samples in comparison with control experiments. Notably, the filtered urea samples doped with silica nanoparticles showed a significantly lower nucleation probability compared to those filtered urea samples doped with AuNPs.

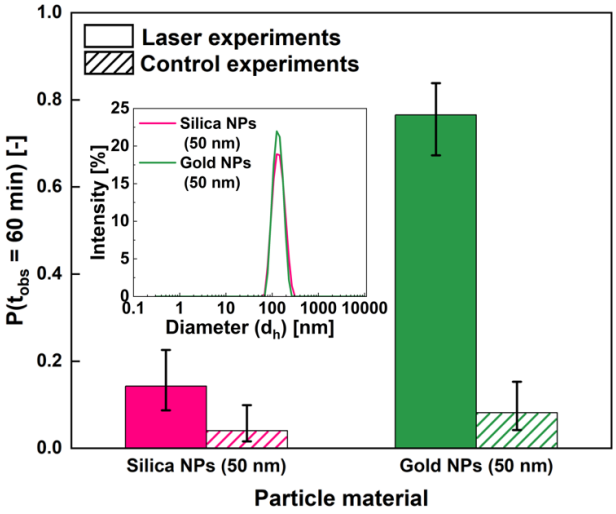

Figure 4.5.: Nucleation probabilities of filtered urea solutions containing AuNPs (50 nm) with different nanoparticle material under S = 1.5 at a laser wavelength (532 nm) and laser peak intensity (376 MW/cm^2) and Inset figure represents particle size distribution of of filtered urea solutions containing AuNPs (50 nm) with different nanoparticle material. Error bars are computed using the Wilson's score method.

For filtered urea samples doped with silica nanoparticles, PSD from DLS data (Figure 4.5 (a)) reveals a mean hydrodynamic diameter of 120 ± 20 nm, which is similar to that of AuNPs. This similarity in particle size between the two types of nanoparticles provides a consistent baseline for comparing the nucleation probabilities based on different materials.

Furthermore, laser irradiation enhanced the nucleation probability in the filtered urea solution doped with AuNPs relative to its control experiment. However, for the urea samples doped with silica nanoparticles, no significant difference in nucleation probability was observed when compared to their control experiment. AuNPs (50 nm),

with an absorption coefficient of 4.05, are more efficient at absorbing the 532 nm laser light than silica nanoparticles, which have an absorption coefficient of just 1.5×10^{-3}. This higher absorption coefficient leads to larger maximum size of the bubble around the AuNPs, as indicated by the relationship $R_{b,max} \propto (Q_{\text{abs}} R_{\text{p}}^2 I_{eff})^{1/3}$. Following the discussion given in section 4.3.2, larger maximum size of the bubble can lead to creating higher local supersaturation at the vapor-liquid interface[22, 29], which could potentially explain the higher nucleation probabilities observed in our experiments.

Also, the critical laser threshold calculated using Equation 4.14 (Appendix C section C.7)required for heating 50 nm silica nanoparticles to a degree that would induce bubble formation is significantly higher than the laser intensity used in our experiments. Therefore, for silica nanoparticles, there is effectively no bubble formation and, as a result, the nucleation probabilities observed in the filtered urea samples doped with silica overlap with those of the control experiments.

It becomes evident that impurities, which notably affect the NPLIN process, can arise from multiple sources such as the solute, the solvent, or additional materials involved in the experimental apparatus. Consequently, based on these experimental findings, it can be reasonably speculated that the concentration, presence, and characteristics of these impurities are critical in determining whether a particular solution will demonstrate NPLIN behavior.

4.4. CONCLUSIONS

This study is focused on understanding how various experimental parameters, including solution filtration, laser intensity, impurity nanoparticle properties such as concentration, particle material, influence the NPLIN probability of supersaturated aqueous urea solutions. The significant findings from this research contribute to a deeper understanding of the NPLIN mechanism, particularly in the context of nanoparticle characteristics and their interaction with laser irradiation.

Filtration was found to reduce NPLIN probability in urea solutions, whereas doping with nanparticles (AuNP or silica) significantly enhanced it, highlighting the critical role of insoluble impurities in the NPLIN process. NPLIN probability increased with increasing laser peak intensity as well as increasing nanoparticle concentration. The study demonstrated notable differences in NPLIN probabilities when doping with different nanoparticle materials, with AuNPs showing significantly nucleation probabilities compared to silica nanoparticles of same size. We attribute this observation to their higher absorption coefficients of AuNPs compared to silica nanoparticles. The study revealed that NPLIN probabilities exhibit a Poisson distribution on both nanoparticle concentration and laser intensity.

BIBLIOGRAPHY

[1] A. J. Alexander and P. J. Camp. “Non-photochemical laser-induced nucleation”. In: *Journal of Chemical Physics* 150.4 (2019). issn: 00219606. doi: 10.1063/1.5079328. url: http://dx.doi.org/10.1063/1.5079328.

[2] Z. Liao and K. Wynne. “A Metastable Amorphous Intermediate Is Responsible for Laser-Induced Nucleation of Glycine”. In: *Journal of the American Chemical Society* 144.15 (2022), pp. 6727–6733. doi: 10.1021/jacs.1c11154.

[3] B. A. Garetz, J. E. Aber, N. L. Goddard, R. G. Young, and A. S. Myerson. “Nonphotochemical, Polarization-Dependent, Laser-Induced Nucleation in Supersaturated Aqueous Urea Solutions”. In: *Physical Review Letters* 77.16 (1996), pp. 3475–3476. url: https://link.aps.org/doi/10.1103/PhysRevLett.77.3475.

[4] W. Li, A. Ikni, P. Scouflaire, X. Shi, N. El Hassan, P. Gémeiner, J.-M. Gillet, and A. Spasojević-de Biré. “Non-Photochemical Laser-Induced Nucleation of Sulfathiazole in a Water/Ethanol Mixture”. In: *Crystal Growth & Design* 16.5 (2016), pp. 2514–2526. issn: 1528-7483. doi: 10.1021/acs.cgd.5b01526. url: http://dx.doi.org/10.1021/acs.cgd.5b01526.

[5] V. Korede, N. Nagalingam, F. M. Penha, N. van der Linden, J. T. Padding, R. Hartkamp, and H. B. Eral. “A Review of Laser-Induced Crystallization from Solution”. In: *Crystal Growth $&Design* 23.5 (2023), pp. 3873–3916. doi: 10.1021/acs.cgd.2c01526.

[6] T. Hua, C. Valentín-Valentín, O. Gowayed, S. Lee, B. A. Garetz, and R. L. Hartman. “Microfluidic Laser-Induced Nucleation of Supersaturated Aqueous Glycine Solutions”. In: *Crystal Growth & Design* 20.10 (Oct. 2020), pp. 6502–6509. issn: 1528-7483. doi: 10.1021/acs.cgd.0c00669. url: https://doi.org/10.1021/acs.cgd.0c00669.

[7] V. Korede, F. M. Penha, V. de Munck, L. Stam, T. Dubbelman, N. Nagalingam, M. Gutta, P. Cui, D. Irimia, A. E. van der Heijden, *et al.* “Design and Validation of a Droplet-based Microfluidic System To Study Non-Photochemical Laser-Induced Nucleation of Potassium Chloride Solutions”. In: *Crystal Growth $&Design* (2023). doi: 10.1021/acs.cgd.3c00591.

[8] B. Clair, A. Ikni, W. Li, P. Scouflaire, V. Quemener, and A. Spasojević-de Biré. “A new experimental setup for high-throughput controlled non-photochemical laser-induced nucleation: application to glycine crystallization”. In: *Journal of Applied Crystallography* 47.4 (Aug. 2014), pp. 1252–1260. doi: 10.1107/S160057671401098X. url: https://doi.org/10.1107/S160057671401098X.

[9] D. Irimia, J. Jose Shirley, A. S. Garg, D. P. Nijland, A. E. Van Der Heijden, H. J. Kramer, and H. B. Eral. “Influence of Laser Parameters and Experimental Conditions on Nonphotochemical Laser-Induced Nucleation of Glycine Polymorphs”. In: *Crystal Growth and Design* 21.1 (2021), pp. 631–641. issn: 15287505. doi: 10.1021/acs.cgd.0c01415.

[10] E. R. Barber, M. R. Ward, A. D. Ward, and A. J. Alexander. “Laser-induced nucleation promotes crystal growth of anhydrous sodium bromide”. In: *CrystEngComm* 23 (47 2021), pp. 8451–8461. doi: 10.1039/D1CE01180D.

[11] D. Mellah, B. Nicolaï, B. Fournier, N. Bošnjaković-Pavlović, F.-X. Legrand, P. Gemeiner, V. Boemare, N. Guiblin, A. Assi, A. Tfayli, S. Konate, P. Durand, and A. Spasojević-de Biré. “New Cocrystallization Method: Non-photochemical Laser-Induced Nucleation of a Cocrystal of Caffeine–Gallic Acid in Water”. In: *Crystal Growth $&Design* 22.10 (2022), pp. 5982–5995. doi: 10.1021/acs.cgd.2c00624.

[12] X. Sun, B. A. Garetz, and A. S. Myerson. “in the Nonphotochemical Laser-Induced Nucleation (NPLIN) of 2006”. In: *Crystal Growth & Design* 6.3 (2006), p. 684.

[13] Y. Liu, M. H. Van Den Berg, and A. J. Alexander. “Supersaturation dependence of glycine polymorphism using laser-induced nucleation, sonocrystallization and nucleation by mechanical shock”. In: *Physical Chemistry Chemical Physics* 19.29 (2017), pp. 19386–19392. issn: 14639076. doi: 10.1039/c7cp03146g.

[14] Y. Liu, M. H. van den Berg, and A. J. Alexander. “Supersaturation dependence of glycine polymorphism using laser-induced nucleation, sonocrystallization and nucleation by mechanical shock”. In: *Phys. Chem. Chem. Phys.* 19 (29 2017), pp. 19386–19392. doi: 10.1039/C7CP03146G.

[15] B. C. Knott, M. F. Doherty, and B. Peters. “A simulation test of the optical Kerr mechanism for laser-induced nucleation”. In: *The Journal of Chemical Physics* 134.15 (Apr. 2011), p. 154501. issn: 0021-9606. doi: 10.1063/1.3574010. url: https://doi.org/10.1063/1.3574010.

[16] A. J. Alexander and P. J. Camp. “Single Pulse, Single Crystal Laser-Induced Nucleation of Potassium Chloride”. In: *Crystal Growth & Design* 9.2 (2009), pp. 958–963. doi: https://doi.org/10.1021/cg8007415.

[17] B. C. Knott, J. L. LaRue, A. M. Wodtke, M. F. Doherty, and B. Peters. “Communication: Bubbles, crystals, and laser-induced nucleation”. In: *The Journal of Chemical Physics* 134.17 (May 2011), p. 171102. doi: 10.1063/1.3582897.

[18] R. Kacker, S. Dhingra, D. Irimia, M. K. Ghatkesar, A. Stankiewicz, H. J. Kramer, and H. B. Eral. “Multiparameter Investigation of Laser-Induced Nucleation of Supersaturated Aqueous KCl Solutions”. In: *Crystal Growth and Design* 18.1 (2018), pp. 312–317. issn: 15287505. doi: 10.1021/acs.cgd.7b01277.

[19] M. R. Ward, A. M. Mackenzie, and A. J. Alexander. “Role of Impurity Nanoparticles in Laser-Induced Nucleation of Ammonium Chloride”. In: *Crystal Growth & Design* 16.12 (Dec. 2016), pp. 6790–6796. issn: 1528-7483. doi: 10.1021/acs.cgd.6b00882. url: https://doi.org/10.1021/acs.cgd.6b00882.

[20] A. Soare, R. Dijkink, M. R. Pascual, C. Sun, P. W. Cains, D. Lohse, A. I. Stankiewicz, and H. J. M. Kramer. “Crystal Nucleation by Laser-Induced Cavitation”. In: *Crystal Growth & Design* 11.6 (2011), pp. 2311–2316. issn: 1528-7483. doi: 10.1021/cg2000014. url: http://dx.doi.org/10.1021/cg2000014.

[21] N. Hidman, G. Sardina, D. Maggiolo, H. Ström, and S. Sasic. “Laser-induced vapour bubble as a means for crystal nucleation in supersaturated solutions—Formulation of a numerical framework”. In: *Experimental and Computational Multiphase Flow* 1 (2019), pp. 242–254.

[22] N. Nagalingam, A. Raghunathan, V. Korede, C. Poelma, C. S. Smith, R. Hartkamp, J. T. Padding, and H. B. Eral. “Laser-Induced Cavitation for Controlling Crystallization from Solution”. In: *Physical Review Letters* 131.12 (Sept. 2023). issn: 1079-7114. doi: 10.1103/physrevlett.131.124001.

[23] M. Briard, C. Brandel, and V. Dupray. “Strong Enhancement of Nucleation Efficiency of Aqueous Ethylenediamine Sulfate Solutions by Nonphotochemical Laser-Induced Nucleation: Investigations on the Role of Solid Impurities in the Mechanism”. In: *Crystal Growth & Design* 23.10 (Sept. 2023), pp. 7169–7178. issn: 1528-7505. doi: 10.1021/acs.cgd.3c00588.

[24] M.-C. Daniel and D. Astruc. “Gold Nanoparticles: Assembly, Supramolecular Chemistry, Quantum-Size-Related Properties, and Applications Toward Biology, Catalysis, and Nanotechnology.” In:

ChemInform 35.16 (Mar. 2004). issn: 1522-2667. doi: 10.1002/chin.200416213.

[25] J. M. Zook, V. Rastogi, R. I. MacCuspie, A. M. Keene, and J. Fagan. "Measuring Agglomerate Size Distribution and Dependence of Localized Surface Plasmon Resonance Absorbance on Gold Nanoparticle Agglomerate Size Using Analytical Ultracentrifugation". In: *ACS Nano* 5.10 (Sept. 2011), pp. 8070–8079. doi: 10.1021/nn202645b.

[26] J. Matic, X. Sun, B. a. Garetz, and a. S. Myerson. "Intensity, Wavelength, and Polarization Dependence of Nonphotochemical Laser-Induced Nucleation in Supersaturated Aqueous Urea Solutions". In: *Crystal Growth & Design* 5 (2005), pp. 1565–1567. doi: 10.1021/cg050041c.

[27] E.-A. Brujan. "Numerical investigation on the dynamics of cavitation nanobubbles". In: *Microfluidics and Nanofluidics* 11.5 (May 2011), pp. 511–517. issn: 1613-4990. doi: 10.1007/s10404-011-0816-3.

[28] S. Egerev, S. Ermilov, O. Ovchinnikov, A. Fokin, D. Guzatov, V. Klimov, A. Kanavin, and A. Oraevsky. "Acoustic signals generated by laser-irradiated metal nanoparticles". In: *Applied Optics* 48.7 (Nov. 2008), p. C38. issn: 1539-4522. doi: 10.1364/ao.48.000c38.

[29] N. Hidman, G. Sardina, D. Maggiolo, H. strom, and S. Sasic. "Numerical Frameworks for Laser-Induced Cavitation: Is Interface Supersaturation a Plausible Primary Nucleation Mechanism?" In: *Crystal Growth & Design* 20.11 (2020), pp. 7276–7290. doi: https://doi.org/10.1021/acs.cgd.0c00942.

[30] L. Wang, Y. Wu, X. Wu, and K. Cen. "Measurement of dynamics of laser-induced cavitation around nanoparticle with high-speed digital holographic microscopy". In: *Experimental Thermal and Fluid Science* 121 (2021), p. 110266. issn: 0894-1777. doi: https://doi.org/10.1016/j.expthermflusci.2020.110266. url: https://www.sciencedirect.com/science/article/pii/S089417772030769X.

[31] V. Korede, M. Veldhuis, F. M. Penha, N. Nagalingam, P. Cui, A. E. Van der Heijden, H. J. Kramer, and H. B. Eral. "Effect of Laser-Exposed Volume and Irradiation Position on Nonphotochemical Laser-Induced Nucleation of Potassium Chloride Solutions". In: *Crystal Growth & Design* 23.11 (Oct. 2023), pp. 8163–8172. issn: 1528-7505. doi: 10.1021/acs.cgd.3c00865.

[32] O. Kvítek, M. Bot, and V. Švorčík. “Gold nanoparticles grafting on glass surface”. In: *Applied Surface Science* 258.22 (Sept. 2012), pp. 8991–8995. issn: 0169-4332. doi: 10.1016/j.apsusc.2012.05.136.

[33] N. Javid, T. Kendall, I. S. Burns, and J. Sefcik. “Filtration Suppresses Laser-Induced Nucleation of Glycine in Aqueous Solutions”. In: *Crystal Growth & Design* 16.8 (July 2016), pp. 4196–4202. doi: 10.1021/acs.cgd.6b00046.

5

CONCLUSION

5.1. OVERVIEW

This thesis presents a comprehensive exploration of non-photochemical laser induced nucleation (NPLIN). An extensive introduction to NPLIN is provided with key experimental observations from the literature, focusing on how laser and solution parameters influence the nucleation kinetics in various solute-solvent systems. Furthermore, the primary mechanisms of NPLIN proposed in the literature, such as the Optical Kerr effect, the Dielectric Polarization model, and the Nanoparticle Heating mechanism, has been discussed. Addressing notable gaps identified in the literature, this research delved into identifying the fundamental mechanism of NPLIN, by investigating how specific laser and solution parameters affect (or influence) nucleation kinetics in various solute-solvent systems.

Chapter 2 describes the effects of the laser-exposed volume and the laser position on the NPLIN probability in supersaturated aqueous potassium chloride solutions. Our findings revealed that the NPLIN probability and the number of nuclei formed per sample are proportional to the sample volume exposed to the laser pulse. Additionally, we observed that the laser position of the exposed sample volume plays an important role in NPLIN, particularly when irradiating in the vicinity of the air/solution interface (meniscus), resulting in a significant increase in nucleation probability, accompanied by changes in crystal shapes. The results can be partly explained by the Nanoparticle Heating and Dielectric Polarization models, although no definitive conclusion can be drawn regarding the dominant mechanism. The implications of our findings extend to industrial applications of NPLIN, where the control of crystal quality parameters, such as morphology, is of great significance.

Chapter 3 introduces an automated droplet-based microfluidic system and a crystal count monitoring system, utilizing deep learning methods, tailored for NPLIN studies to address the key limitation in NPLIN research, i.e., insufficient data due to the labor-intensive nature of traditional bulk experiments. The study systematically explores various experimental

conditions, including supersaturation, laser wavelength, laser intensity, and the impact of solution filtration using aqueous KCl solutions, to quantify their influence on the NPLIN probability and to study the correlation of these results with the different NPLIN mechanisms proposed in the literature. Notably, the results show that laser intensities exceeding 50 MW/cm^2 are necessary to induce nucleation at a supersaturation level of $S = 1.05$ to achieve nucleation probabilities higher than in control experiments due to the small droplet volumes. However, for $S = 1.10$, an intensity of 10 MW/cm^2 was already sufficient to observe nucleation probabilities higher than control experiments. No significant wavelength effect was observed, except for irradiation with 355 nm light at higher laser intensities ($\geq$ 50 MW/cm^2). Solution filtration using a filter pore size smaller than 7μm effectively suppressed NPLIN, while the introduction of nanoparticles as dopants into the filtered solution enhanced nucleation probabilities and modified crystal morphology, in line with the hypothesis of the nanoparticle/impurity heating mechanism of NPLIN.

5

Chapter 4 delves into examining the effects of solution filtration, laser peak intensity, and impurity nanoparticle properties such as concentration and material on the NPLIN probability in supersaturated aqueous urea solutions. The study highlights the critical role of impurities in NPLIN, with notable differences observed in NPLIN probabilities when doping with different nanoparticle materials. Gold nanoparticles enhanced nucleation probabilities more effectively than silica nanoparticles as a result of their higher absorption coefficients. The study demonstrated a Poisson distribution dependency of NPLIN probabilities on both nanoparticle concentration and laser peak intensity. Furthermore, the presence and nature of impurities were emphasized as key determinants in the occurrence of NPLIN in different solutions.

Although the majority of observations from the literature and this thesis can be explained using the nanoparticle heating hypothesis, it is important to emphasize the absence of a comprehensive theoretical framework that fully explores this mechanism. Therefore, further research should involve computational simulations to model the interactions between laser light and nanoparticles present in the supersaturated solution. Such simulations could provide a theoretical framework that not only complements experimental observations but also predicts NPLIN based nucleation kinetics under varying laser and solution parameters, thereby guiding experimental designs and enhancing our understanding of the nanoparticle heating mechanism.

The work presented in this thesis has not only added to the existing knowledge base of NPLIN, providing valuable insights into the mechanisms governing NPLIN, but has also raised pertinent questions that will shape the direction of future research in this domain.. Future work could focus on utilizing the droplet-based microfluidic setup developed to provide a controlled environment for studying the formation of dif-

ferent polymorphs under varying laser and solution properties. This research could explore the potential of NPLIN to selectively induce the formation of desired polymorphs. The advantages and limitations of using NPLIN-generated seed crystals versus traditional seed crystals in terms of growth rates, crystal size distribution, and purity for secondary crystallization processes could reveal new insights into optimizing crystallization techniques for industrial applications. Further research could focus on how NPLIN can be utilised in more complex, multi-component systems.

In conclusion, while the findings of this thesis enhance our understanding of NPLIN, several challenges remain before it can be effectively applied in industrial settings. Future research should continue to explore the fundamental mechanisms of NPLIN, with a particular focus on scaling up the process to larger volumes, enhancing its robustness under diverse conditions, and integrating it with real-time monitoring and control systems. Additionally, efforts should be directed towards optimizing the economic feasibility of NPLIN technology towards industrial applications. Addressing these challenges should pave the way for NPLIN to transition from a promising laboratory method to a viable industrial technology, potentially revolutionizing the crystallization processes used in various industries.

A

APPENDIX A

A.1. LASER EXPOSED VOLUME DEPENDENCY OF DP MODEL

In line with the Dielectric Polarization model, the free energy change of cluster formation, ΔG, is made up of contributions from the free energy change of surface formation, ΔG_s, the free energy change of phase transformation, ΔG_v, and the change in free energy due to the introduction of an electric field, ΔG_{EF}. In presence of an electric field and under the constraint that the $\epsilon_p > \epsilon_s$, the free energy change of cluster formation (ΔG) is lowered by an amount proportional to $-v(\epsilon_p - \epsilon_s)E^2$, where v is the volume of the cluster, ϵ_p is the dielectric constant of a cluster of solute molecules, ϵ_s is the dielectric constant of the surrounding medium and E is the electric field strength [1]. For convenience, the electric field strength can be written in terms of intensity by the equation $I = \frac{1}{2}\epsilon_0 c E^2$, where I is the intensity of the light, ϵ_0 is the vacuum permittivity and c is the speed of light. Hence, by adding the contribution of the electric field induced by the light, the change in free energy becomes,

$$\begin{aligned} \Delta G &= \Delta G_s + \Delta G_v + \Delta G_{EF} \\ &= s\gamma + v\rho\Delta\mu - v\alpha I \end{aligned} \tag{A.1}$$

where s and v are the surface area and volume of the precritical cluster, respectively, γ is the interfacial tension between the cluster and surrounding solution, ρ is the number of molecules per unit volume in the solid phase and $\Delta\mu$ is difference in chemical potential of the substance in solution and in the crystal. The constant α contains the dielectric contrast between solute cluster and the surrounding medium.

$$\alpha = \frac{3\epsilon_s(\epsilon_p - \epsilon_s)}{c(\epsilon_p + 2\epsilon_s)} \tag{A.2}$$

Then, assuming the precritical clusters are spheres with a radius r, the free energy change of cluster formation becomes,

$$\Delta G(r, I) = 4\pi r^2\gamma + \frac{4}{3}\pi r^3\Delta\mu - \frac{4}{3}\pi r^3\alpha I \tag{A.3}$$

A

Substituting chemical potential in terms of supersaturation in equation A.3, assuming a supersaturated solution in which the solute chemical potential exceeds the chemical potential of the crystal, results in,

$$\Delta G(r, I) = 4\pi r^2 \gamma - \frac{4}{3}\pi r^3 (\rho k_B T \ln S + \alpha I) \tag{A.4}$$

where k_B is the Boltzmann constant, T is the temperature of the solution and S is the supersaturation ratio of the solution. Analogously to the Classical Nucleation Theory it is possible to derive the critical radius, $r_c(I)$, and nucleation barrier height, $\Delta G_c(I)$, under the influence of an electric field,

$$r_c(I) = \frac{2\gamma}{\rho k_B T \ln S + \alpha I} \tag{A.5}$$

$$\Delta G_c(I) = \frac{16\pi\gamma^3}{3(\rho k_B T \ln S + \alpha I)^2} \tag{A.6}$$

Prior to laser irradiation when nucleation has not yet occurred, all clusters are said to be smaller than the critical radius ($r < r_c(0)$). Upon laser irradiation, all clusters with size $r_c(I) < r < r_c(0)$ become supercritical. The average number of precritical clusters ($r < r_c(0)$) can be computed by,

$$N_{cluster} = \frac{N_{molecule}}{\langle n \rangle} \tag{A.7}$$

where $N_{molecule}$ is the number of solute molecules in the volume of the laser beam, and $\langle n \rangle$ is the average amount of solute molecules in a precritical cluster, which can be computed by assuming a Boltzmann distribution over the domain $r \in [0, r_c(0)]$,

$$\begin{aligned} \langle n \rangle &= \frac{4\pi\rho \langle r^3 \rangle}{3} \\ &= \frac{4\pi\rho}{3} \times \frac{\int_0^{r_c(0)} r^3 \exp[-\Delta G(r,0)/k_B T] dr}{\int_0^{r_c(0)} \exp[-\Delta G(r,0)/k_B T] dr} \end{aligned} \tag{A.8}$$

Hence,

$$\begin{aligned} N_{cluster} = &\frac{3N_{molecule}}{4\pi\rho} \\ &\times \frac{\int_0^{r_c(0)} \exp[-\Delta G(r,0)/k_B T] dr}{\int_0^{r_c(0)} r^3 \exp[-\Delta G(r,0)/k_B T] dr} \end{aligned} \tag{A.9}$$

To obtain the average number of clusters that go on to form viable crystals after laser irradiation, $N_{crystal}$, the average amount of precritical clusters is multiplied by the fraction of clusters that become supercritical,

$$N_{crystal} = N_{cluster} \times \frac{\int_{r_c(I)}^{r_c(0)} \exp\left[-\Delta G(r,0)/k_B T\right] dr}{\int_{0}^{r_c(0)} \exp[-\Delta G(r,0)/k_B T] dr} \tag{A.10}$$

Hence, by combining equation A.9 and A.10 a function for the average amount of clusters that go on to form viable crystals is obtained,

$$N_{crystal} = \frac{3N_{molecule}}{4\pi\rho} \times \frac{\int_{r_c(I)}^{r_c(0)} \exp\left[-\Delta G(r,0)/k_B T\right] dr}{\int_{0}^{r_c(0)} r^3 \exp[-\Delta G(r,0)/k_B T] dr} \tag{A.11}$$

The amount of solute molecules per unit volume can be written in terms of the solute density, $\rho = \frac{\rho_s N_A}{M}$, where N_A is Avogadro's constant and M is the molar mass of the solute. In addition, the amount of molecules in the volume of the laser beam can be written as,

$$N_{molecule} = \frac{V_{laser}\rho_l N_A W}{M} \tag{A.12}$$

where V_{laser} is the volume of the laser passing through the solution,ρ_l is the density of the surrounding medium and W is the solute mass fraction. Therefore the average amount of clusters that go on to form viable crystals becomes,

$$N_{crystal} = \frac{3V_{laser}\rho_l W}{4\pi\rho_s} \times \frac{\int_{r_c(I)}^{r_c(0)} \exp\left[-\Delta G(r,0)/k_B T\right] dr}{\int_{0}^{r_c(0)} r^3 \exp[-\Delta G(r,0)/k_B T] dr} \tag{A.13}$$

Under the constraints of constant intensity and supersaturation, the only dependent variable is V_{laser}, and hence we can write $N_{crystal}$ as,

$$N_{crystal} = m(I,S)V_{laser} \tag{A.14}$$

where $m(I,S)$ serves as a new, intensity and supersaturation dependent

A

lability constant,

$$m(I,S) = \frac{3\rho_l W}{4\pi\rho_s} \times \frac{\int_{r_c(I)}^{r_c(0)} \exp\left[-\Delta G(r,0)/k_B T\right] dr}{\int_0^{r_c(0)} r^3 \exp[-\Delta G(r,0)/k_B T] dr} \tag{A.15}$$

By assuming a Poisson distribution it is possible to compute the probability that no crystals are observed in any of the repeated experiments,

$$p_0 = \exp[-m(I,S)V_{laser}] \tag{A.16}$$

At last, the cumulative nucleation probability is computed as a function of intensity, supersaturation and laser exposed volume,

$$\begin{aligned} p_{nucleation} &= 1 - p_0 \\ &= 1 - \exp[-m(I,S)V_{laser}] \end{aligned} \tag{A.17}$$

A.2. LASER EXPOSED VOLUME CALCULATION

A cross-sectional view in the xy-plane of the laser beam passing through the vial is shown in Figure SIA. The laser passes through three media with different refractive indices, resulting in two directional changes of the laser path in the y-direction. In order to calculate the volume of the beam, the angles of incidence and angles of refraction passing through the vial have to be calculated. The angle of incidence resulting from the change of medium from air to borosilicate glass, Θ_1, can be computed by,

$$\sin\Theta_1 = \frac{r}{R_0} \tag{A.18}$$

where, r is the radius of the laser beam at a given cross-section and R_0 is the radius of the outer surface of the glass vial. Note that in Figure SIA, r is given as the radius of the incident beam, R_L. The usefulness of this will become evident at a later stage of this derivation. Then, by implementing Snell's law, it is possible to compute the first angle of refraction, Θ_2,

$$n_1 \sin\Theta_1 = n_2 \sin\Theta_2 \tag{A.19}$$

where n_1 and n_2 are the refractive indices of the air and borosilicate glass, respectively. Further inspection of a zoomed in version of the triangle enclosed by the path of the laser through the glass wall, L_L, and the outer and inner radius of the glass vial, R_0 and R_1, respectively (see Figure SIB) reveals,

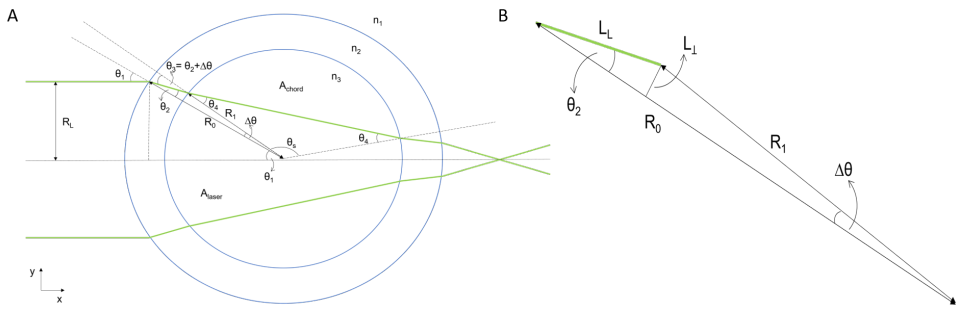

Figure SI.: (A) Cross-sectional area of the laser beam passing through a cylindrical vial. This figure is not to scale and thus the given angles are only a guide to the eye, (B) Zoomed in version of the triangle enclosed by the path of the beam and the outer and inner radius of the glass vial.

$$L_L \sin\Theta_2 = R_1 \sin\Delta\Theta \tag{A.20}$$

where $\Delta\Theta$ is the angle between R_0 and R_1. In addition, it shows that,

$$R_0 = L_L \cos\Theta_2 + R_1 \cos\Delta\Theta \tag{A.21}$$

Hence, by combining equations A.20 and A.21 an equation is obtained to describe the outer radius of the vial as a function of $\Delta\Theta$,

$$R_0 = \frac{R_1 \sin\Delta\Theta}{\tan\Theta_2} + R_1 \cos\Delta\Theta \tag{A.22}$$

Equation A.22 can be solved numerically to find the value for $\Delta\Theta$. Following a geometrical derivation, the second angle of incidence, Θ_3, can be written as $\Theta_2 + \Delta\Theta$. Then, using Snell's law again, the second angle of refraction, Θ_4 is obtained,

$$n_2 \sin(\Theta_2 + \Delta\Theta) = n_3 \sin\Theta_4 \tag{A.23}$$

From equations A.18-A.23 all necessary angles can be computed in order to calculate the central angle, Θ_s, and subsequently the area of the disc segment, A_{chord}. The central angle is given by,

$$\Theta_s = \pi - 2\Theta_4 \tag{A.24}$$

and the area of the disc segment by,

$$A_{chord} = \frac{R_1^2}{2}(\Theta_s - \sin\Theta_s) \tag{A.25}$$

A

The cross-sectional area of the inner circle of the vial, A_{circle}, can be written in terms of πR_1^2. Hence, the area of the laser path through the solution, A_{laser}, becomes,

$$A_{laser} = A_{circle} - 2A_{chord} = R_1^2(\pi - \Theta_s + \sin\Theta_s) \tag{A.26}$$

Subsituting equation A.24 into equation A.26 will give the area of the laser passing through the solution in terms of the second angle of refraction,

$$A_{laser} = R_1^2(2\Theta_4 + \sin 2\Theta_4) \tag{A.27}$$

Now that the cross-sectional area of a particular slice of the laser beam has been obtained, it is possible to compute the volume of the laser beam through the solution by summing all slices of the cross-sectional area. One particular slice is defined by half a chord length of the cross-sectional area of the incident laser beam (see Figure SII). Hence,

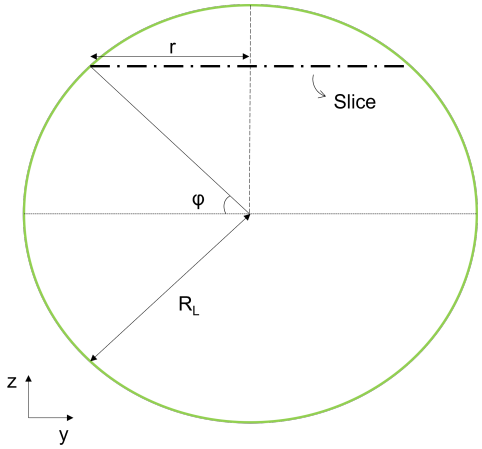

Figure SII.: Cross-sectional area of the incident laser beam.

$$r = R_L \cos\phi \tag{A.28}$$

Substituting equation A.28 in equation A.18 results in,

$$\sin\Theta_1 = \frac{R_L \cos\phi}{R_0} \tag{A.29}$$

Following this the area of the laser passing through the solution, A_{laser}, becomes a function of ϕ. The laser exposed volume, V_{laser}, can be computed by summing over all the slices,

$$V_{laser} = 2 \cdot \int_0^{\frac{1}{2}\pi} A_{laser} dr \tag{A.30}$$

or, by substituting equation A.28 and the derivative of equation A.29,

$$V_{laser} = 2R_L R_1^2 \cdot \int_0^{\frac{1}{2}\pi} (2\Theta_4 + \sin(2\Theta_4)) \cos\phi d\phi \tag{A.31}$$

The integral in equation A.31 has been solved numerically in order to find the volume of the laser beam passing through the solution. In addition, by recognizing that the cross-sectional area of the laser beam gets smaller due to the focusing effect in the y-direction, it is possible to calculate the change in intensity of the beam throughout the vial. Focusing the beam in solely the y-direction changes the profile of the beam from a circle to an ellipse. The radius of the ellipse in the y-direction is defined by the linear function of the laser beam through the solution, $y = mx + b$ (see Figure SIII). The slope coefficient, m, can be computed by,

$$m = \tan(-\Theta_m) = \tan(\Theta_1 + \Delta\Theta - \Theta_4) \tag{A.32}$$

At last, it is possible to compute the width of the ellipse at the end of the vial, $R_{ellipse}$,

$$R_{ellipse} = R_1 \sin(\Theta_4 - \Theta_m) \tag{A.33}$$

This allows for the calculation of the intensity of the laser beam at the exit of the vial.

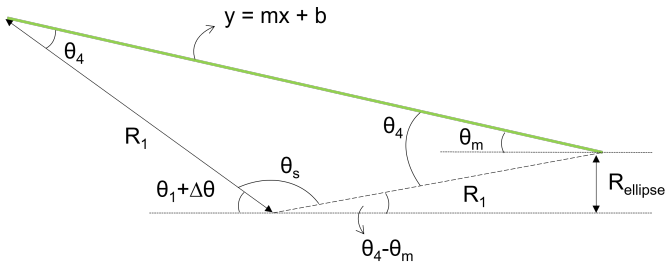

Figure SIII.: Zoomed in version of the triangle enclosed by the chord formed by the path of the beam through the solution and the inner radii of the glass vial.

A

A.3. LASER OPERATION AND CHOICE OF LASER PARAMETERS

Previous experiments on aqueous potassium chloride solutions have shown that the cumulative nucleation probability is a function of the peak intensity of the laser [2, 3]. In the current study, the peak intensity, I_{peak} is calculated by dividing the peak power, P_{peak}, by the cross-sectional area of the beam, A_{beam}.

$$I_{peak} = \frac{P_{peak}}{A_{beam}} \tag{A.34}$$

The peak power of the beam is obtained from the laser characteristics,

$$P_{peak} = \frac{E_{pulse}}{\tau} \tag{A.35}$$

where E_{pulse} is the pulse energy of the laser and τ is the pulse width. Substituting equation A.35 in equation A.34 and assuming that the cross-sectional area of the fundamental beam is a circle, results in

$$I_{peak} = \frac{2E_{pulse}}{\tau\pi R_L^2} \tag{A.36}$$

where R_L is the laser beam radius. The borosilicate HPLC vials act as a cylindrical lens due to their geometry and difference in refractive indices of air (n_1), borosilicate glass (n_2) and potassium chloride solution (n_3). As a result, the peak intensity of the laser beam changes depending on the position within the vial. Because the vials only focus the beam in the y-direction, the resulting cross-sectional area of the beam within the vial can be described by that of an ellipse, and hence the peak intensity becomes

$$I_{peak} = \frac{2E_{pulse}}{\tau\pi R_L R_{ellipse}(x)} \tag{A.37}$$

where $R_{ellipse}(x)$ is the length of the semi-minor axis of the ellipse, depending on the position, x, within the vial. Figure SIVA shows a cross-sectional top view in the xy-plane of the vial and corresponding fundamental laser beam with a diameter of 9 mm. The area of the cross-section of the laser beam is smallest at the back of the vial, and hence a maximum peak intensity, I_{peak}^{max}, is found at the position where the laser hits the inner walls at the back of the vial for the first time.

The first angle of incidence (Θ_1) changes depending on the laser beam diameter. As a result, the relative change of peak intensity throughout the vial is different for each beam diameter (shown in Figure SIVB). The peak intensity becomes increasingly larger when the laser propagates throughout the vial. This effect increases the larger the incident beam diameter. To account for this difference, *a priori* calculations have been

performed to determine the necessary peak intensity of the laser beam in front of the vial to achieve a maximum peak intensity that is constant for all beam diameters. Values of 16.6 and 0.5 mm were assumed for the vial outer diameter and glass thickness, respectively. In addition, the refractive index of air and borosilicate glass are assumed to be 1.0000 and 1.5195, respectively [4]. In absence of equipment to accurately record the refractive index of the potassium chloride solutions, an assumption has been made by calculating the refractive index using an empirical relation [5]

$$n_3 = 1.3352 + (1.6167 \cdot 10^{-3})c - (4.0 \cdot 10^{-7})c^2 - (1.1356 \cdot 10^{-4})T - (5.7 \cdot 10^{-9})T^2 \tag{A.38}$$

where c is the concentration of the solution in $g_{KCl}/g_{solution} \times 100\%$ and T the temperature of the solution in $°C$.

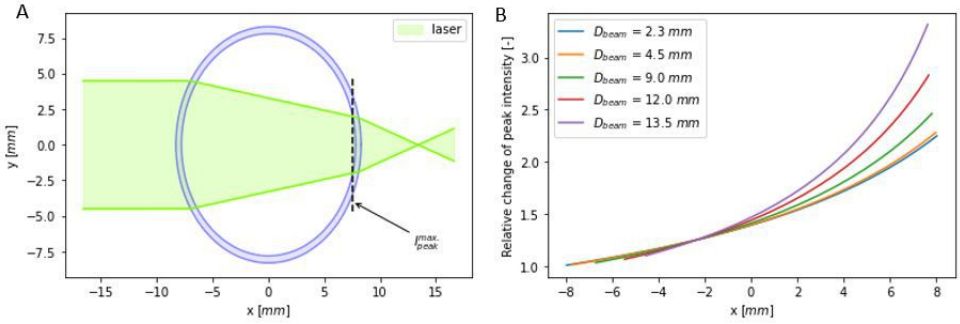

Figure SIV.: (a) Top view of the laser path through a vial containing an aqueous potassium chloride solution (S = 1.034). A incident beam diameter of 9.0 *mm* is shown. (b) Plot showing relative change in peak intensity throughout the vial for different beam diameters (D_{beam}).

A

A.4. ZEMAX SIMULATION

The additional data presented here elaborates on the laser-meniscus interaction study conducted within an HPLC vial. This is further illustrated with extended visualizations from the CAD model, which specifically emphasize the laser's interaction with the meniscus. This interaction can be seen from both the side and top views as shown in Figures SVA and SVB.

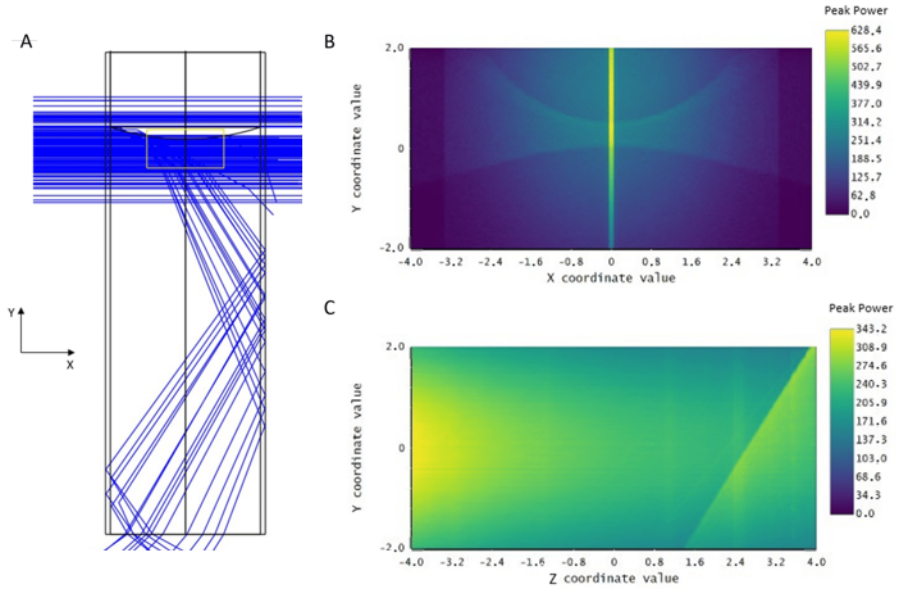

Figure SV.: (A) Simulation in Zemax OpticStudio showcasing the behavior of light rays as they encounter total internal reflection when a laser illuminates the meniscus of a solution (side view), (B) Top view, (C) A representation of the peak intensity distribution across the XY plane at a depth of Z = 0 mm within the volume detector, (D) A representation of peak intensity distribution across the YZ plane at a position of X = 0 mm.

In experiments, it has been observed that crystals always form at a point At this stage, to acquire a comprehensive understanding of the laser intensity distribution beneath the meniscus, a volumetric detector of dimensions 8*4*8 mm, color coded orange was placed directly below it. The volume detector was positioned based on the location of crystal formation observed experimentally on the meniscus following the laser shot. The positioning ensured that the bottom region of the meniscus was encompassed within the detecting volume. This detector was composed of 4 million voxels arranged in a 200 x 100 x 200 configuration, with each voxel designed to detect transmitted rays (flux) in MW/cm^2. Each voxel has a dimension of $40\times40\times40\mu$m. The power distribution within this 3D volume was visualized using 2D slices. For clarity and il-

lustrative purposes, the intensity distribution is represented across both parallel (XY) and perpendicular (YZ) planes, as depicted in Figures SVC & SVD. These images show the distribution at a fixed position of Z = 0 mm and a depth of X = 0 mm (axis numbers goes from -4 mm to 4 mm), respectively. For instance, at specific coordinates (highlighted as X in the figure), the detected laser peak intensity was approximately 17.18 MW/cm^2. Such pronounced peak intensities, especially at the meniscus, could be attributed to the cylindrical nature of the vial, the total internal reflection induced by the meniscus, and the rear wall partial reflection. These factors may probably explain the high nucleation probabilities observed in laser irradiation experiments at the meniscus in the context of Dielectric Polarization model or Nanoparticle Heating mechanism.

B

APPENDIX B

B.1. HYDROPHOBIZATION PROTOCOL

The following steps were taken to hydrophobically coat the 30 cm capillaries used in the microfluidic set-up for NPLIN experiments:

- Flush the inside of the capillary with 10 mL of 0.1M Sodium Hydroxide (NaOH) solution.
- Rinse the the inside of the capillary with 20 mL of ultra pure water.
- Dry the capillary externally (if wet) using a paper towel.
- Dry the inside of the capillary with pressurized nitrogen gas.
- Add 16 μL of trichloro(1H,1H,2H,2H-perfluoroctyl)-silane to a 1.5 mL glass vial and close it.
- Insert the capillary into the 1.5 mL glass vial through a hole in its cap.
- Place the vial with the inserted capillary into a desiccator.
- Close off the desiccator in the fume hood, reduce the pressure to <30 mbar and let it rest overnight (> 12 hours).
- Carefully return the desiccator to atmospheric pressure, open it in the fume hood and let it sit for a few minutes for any residual trichloro(1H,1H,2H,2H-perfluoroctyl)-silane to evaporate.
- Wipe the capillary externally with isopropanol, repeat with acetone and flush with pressurized nitrogen gas to ensure any residue of trichloro(1H,1H,2H,2H- perfluoroctyl)-silane is removed from the capillary.

B.2. ESTIMATION OF COOLING LENGTH

The IR temperature sensor was implemented in the system to study droplet temperature before the laser exposure location to make sure the droplets have reached ambient temperature. This is important, because only then the supersaturation of the KCl solutions in the droplets will have the desired value. To this end, a very simplified estimation of the cooling length was determined from the formula for thermal diffusion distance and thermal diffusion time.

$$x = \sqrt{2\alpha t} \tag{B.1}$$

$$t = \frac{L^2}{2\alpha} \tag{B.2}$$

where x is the distance in mm at which droplets attain the ambient temperature (25°C) within the capillary, α is the thermal diffusivity of water at ambient temperature in m^2/s, t is the time in seconds it takes for the droplets to reach ambient temperature, L is the length of the capillary in mm. However, the analysis considered here is an approximation method to calculate the temperature profile based on the following assumptions.

- Assuming that capillary tube is filled with only one fluid which has the physical properties of water at 25°C.
- Temperature in the capillary tube is assumed to be the same along the entire length of the tube and the heat only flows in one direction (axially) and is not affected by the radial direction or outer part of the capillary. This means that the temperature profile is assumed to be linear along the capillary. It is an approximation method to calculate the temperature profile and time taken to reach final temperature.
- Calculations of the temperature profile and time taken to reach the final temperature are performed under steady state conditions, assuming that the ambient temperature is constant.

Using the equations and assumptions above, the cooling length was estimated to be around 15.6 mm. The actual cooling length will be slightly different, because both conduction through the wall hindering heat transfer and convection in the air around the capillary promoting heat transfer have not been taken into account. Although the actual cooling length might deviate from the calculated value because of the oversimplification, it is safe to assume that the droplets have cooled down to room temperature before reaching the laser exposure location 8 cm into the capillary.

B.3. IR SENSORS VS DEEP LEARNING: A COMPARISON

The droplet length distribution for all experiments performed, characterized using both IR sensors and the deep learning method, is provided in Table SI. To illustrate the results, Figure SI provides a representative histogram of the droplet length distribution from a single experiment (S = 1.1, 1064 nm, 25 MW/cm^2). Additionally, Table SII presents a comparison of the average droplet lengths obtained from the IR sensor, deep learning method, and manual measurement. The approximate volume of the droplets per experimental video was obtained by estimating the individual length of each droplet from its bounding box and multiplying the length obtained with the dimensions of the square capillary (0.9*0.9 mm^2). The average volume per experimental video was then found by finding the mean of the individual droplet volumes.

Table SI.: Comparision of droplet length distribution characterized via both the IR sensors and the deep learning method for all the experiments performed

	Supersaturation (S)	Wavelength (nm)	Laser Intensity (MW/cm^2)	Average length (mm)	Average volume (μ_v) (μL)	Average volume variation (σ_v)	Coefficient of variation ($\psi = \sigma_v/\mu_v$)	Average pulses per droplet (#)	Average pulses per droplet ($\sigma_\#$))
Deep learning method	1.05	Blank	0	1.453	1.177	0.084	0.071	12.969	1.011
		1064	10	1.619	1.311	0.061	0.046	13.478	0.848
		1064	25	1.535	1.243	0.093	0.075	14.365	1.202
		1064	50	1.519	1.230	0.175	0.142	13.091	1.414
		1064	100	1.554	1.258	0.145	0.115	13.347	1.301
		532	10	1.500	1.215	0.101	0.083	12.892	1.002
		532	25	1.409	1.141	0.060	0.052	13.595	1.123
		532	50	1.702	1.378	0.163	0.118	14.805	1.657
		532	100	1.465	1.186	0.063	0.053	13.016	0.886
		355	10	1.865	1.511	0.092	0.061	14.315	1.06
		355	25	1.833	1.485	0.120	0.081	14.391	1.121
		355	50	1.509	1.222	0.105	0.086	12.423	1.010
		355	70	1.438	1.165	0.0571	0.049	12.510	0.906
	1.1	Blank	0	1.415	1.146	0.035	0.030	13.394	0.776
		1064	10	1.531	1.240	0.145	0.117	12.480	1.280
		1064	25	1.553	1.258	0.126	0.100	13.333	1.069
		1064	50	1.464	1.186	0.115	0.097	13.045	0.951
		1064	100	1.561	1.264	0.109	0.086	12.626	0.957
		532	10	1.535	1.243	0.130	0.104	13.680	1.792
		532	25	1.696	1.373	0.083	0.060	14.907	0.976
		532	50	1.299	1.052	0.029	0.027	9.863	0.783
		532	100	1.479	1.198	0.127	0.106	10.927	1.335
		355	10	1.528	1.238	0.100	0.081	12.731	1.594
		355	25	1.469	1.190	0.091	0.076	12.649	0.960
		355	50	1.498	1.213	0.063	0.052	13.505	0.985
		355	70	1.540	1.248	0.033	0.027	13.201	0.680
	Supersaturation (S)	Wavelength (nm)	Laser Intensity (MW/cm^2)	Average length (mm)	Average volume (μ_v) (μL)	Average volume variation (σ_v)	Coefficient of variation ($\psi = \sigma_v/\mu_v$)	Average pulses per droplet (#)	Average pulses per droplet ($\sigma_\#$))
Infrared sensors (IR)	1.05	Blank	0	1.197	0.897	0.1695	0.188	10.114	1.057
		1064	10	1.183	0.959	0.091	0.095	10.456	0.751
		1064	25	1.549	1.254	0.157	0.125	12.947	1.168
		1064	50	1.301	1.023	0.273	0.267	11.087	1.610
		1064	100	1.275	1.032	0.285	0.276	11.053	1.656
		532	10	1.176	0.952	0.195	0.205	10.371	1.225
		532	25	1.270	1.029	0.135	0.131	9.560	0.900
		532	50	1.968	1.594	0.37	0.232	13.914	2.136
		532	100	1.437	1.164	0.143	0.122	9.887	1.450
		355	10	1.581	1.280	0.170	0.133	11.792	1.127
		355	25	1.608	1.303	0.217	0.166	11.806	1.272
		355	50	1.191	0.965	0.083	0.086	10.105	0.996
		355	70	1.225	0.992	0.368	0.371	10.587	1.995
	1.1	Blank	0	1.280	1.037	0.095	0.091	10.971	1.121
		1064	10	1.428	1.157	0.609	0.526	11.050	3.151
		1064	25	1.170	0.948	0.256	0.270	10.467	1.451
		1064	50	1.024	0.829	0.175	0.211	9.934	1.049
		1064	100	1.179	0.955	0.173	0.182	10.368	1.132
		532	10	1.428	1.280	1.037	0.196	0.189	10.939
		532	25	1.170	1.730	1.401	0.141	0.100	12.664
		532	50*	-	-	-	-	-	-
		532	100	1.179	1.254	1.016	0.303	0.298	10.771
		355	10	1.306	1.058	0.516	0.487	11.025	2.760
		355	25	1.345	1.089	0.581	0.533	10.934	2.990
		355	50	1.456	1.179	0.105	0.089	11.369	0.830
		355	70	1.223	0.991	0.074	0.075	10.751	0.679

IR sensors data was not available for the experiment with * sign.

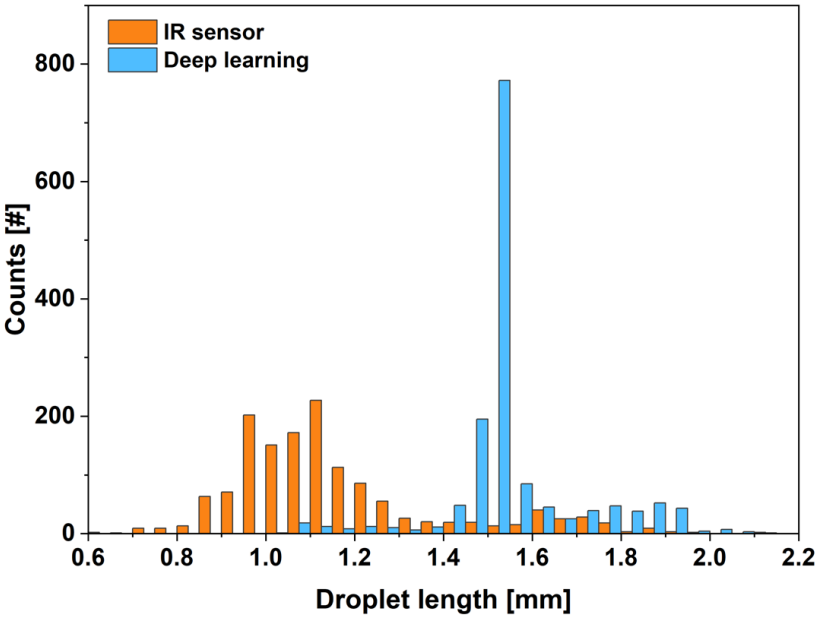

Figure SI.: Comparison of the droplet length distribution using IR and deep learning methods.

As discussed in the main article, the average length results obtained from the deep learning method were found to be reliable in comparison to IR sensors results.

Table SII.: Table comparing average droplet length measurements taken via three different methods.

Measurement method (100 readings)	Average droplet length (mm)
IR sensor	1.526
Deep learning	1.812
Manual	1.833

B.4. DROPLET CHARACTERIZATION RESULTS

To further show the comparision between individual experiments, Droplet volume distributions obtained for all the experiments under S = 1.05 & 1.10 from deep learning method are shown in Figure SII A & C respectively. At each wavelength, the measurements are portrayed in order of increasing laser intensity. Similarly pulses per droplet distribution are shown in SII B & D respectively.

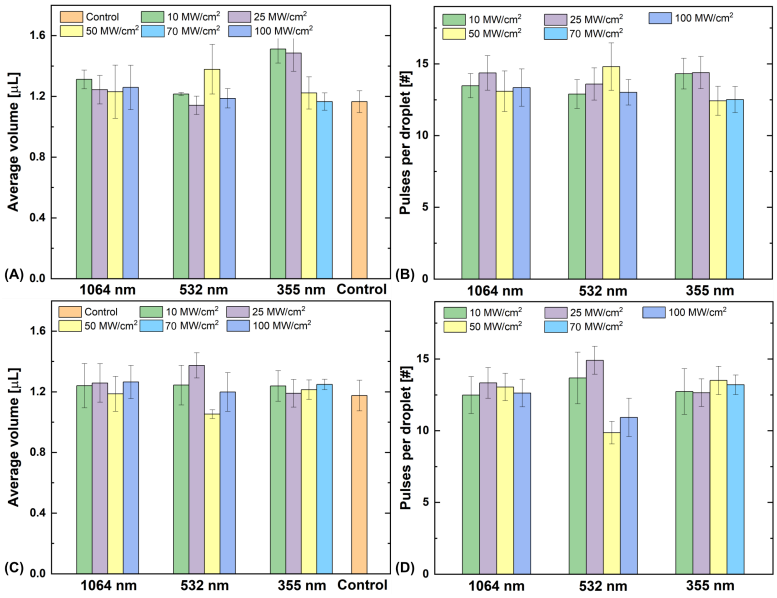

Figure SII.: Droplet characterization for experiments under S = 1.05 (A & B) and S = 1.10 (C & D) showing the average droplet volume and average number of pulses per droplet for all the experiments.

B.5. DEEP LEARNING METHOD

As described in the deep learning section of the article, the classification of cropped images to detect the presence of a crystal is more challenging than droplet detection. One primary reason for this difficulty is the different morphologies of KCl crystals, as shown in Figure SIII. Some images of droplets, such as SIIIc, SIIId, and SIIIe, display transparent crystals that are potentially difficult to detect due to poor contrast. In addition, a few needle-shaped crystals SIIIb were also observed. Moreover, there might be images of droplets with impurities present on the outside of the capillary, which might also be classified as a crystal. Therefore, it is crucial to train the algorithm sufficiently well to robustly detect different morphologies of KCl crystals automatically.

B.5.1. TRAINING INFORMATION

The training of the images was not performed on experimental videos with 1.05 supersaturation because the crystals were too small for the algorithm to detect. Consequently, a manual count of droplets containing crystals was provided for 1.05 supersaturation experimental videos to estimate nucleation probabilities and for further data analysis. On the other hand, the training of the images was performed through super-

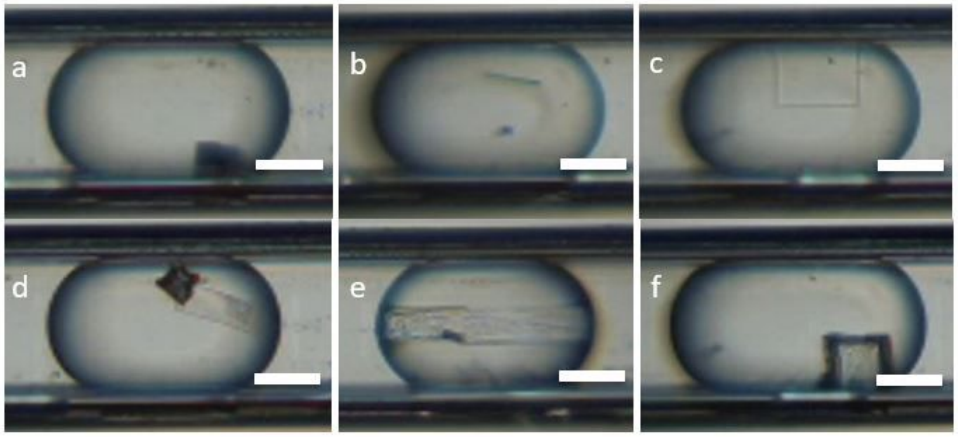

Figure SIII.: Images of the different droplets having the same KCl crystal but with different morphologies. Scale bar is 1 mm for all the images.

vised learning, i.e., hand-labeling 777 images from different videos with 1.1 supersaturation. The images were carefully chosen to ensure they were challenging to categorize and could be easily misclassified. Selecting these types of images is crucial for training the model, as the more difficult and complex the samples, the more robust the training process. The training data was labeled with 438 images of droplets containing crystals and 339 images of empty droplets. The binary classification task was performed using the ResNet50 architecture with pre-trained weights and five-fold cross-validation. Apart from the training data, 46 images were set aside as test data to validate the model's performance. The test data contained 16 images of droplets without a crystal, all of which were predicted correctly. However, 4 of the 26 images of droplets with crystals were incorrectly predicted, resulting in an accuracy of 91.17% on the test data.

B.5.2. RESULTS

Once the model was trained using supervised learning, different combinations of NPLIN experiments recorded as videos were run through the algorithm one at a time to count the droplets with crystals automatically. At this point, the output quality of the classifier was measured using the F1-score metric based on a confusion matrix. In machine learning, the F1-score is defined as the harmonic mean of precision and recall. The confusion matrix numbers for all the experimental combinations, along with their F1-scores, are shown in Table SIII below. Although the accuracy of our model is very high (94.7 - 100%) between different experimental videos, there is a comparatively broad variation in the F1-scores obtained

(82.7 - 100%). The main reason for this variation is that our data is skewed, i.e., there are many empty droplets compared to droplets with crystals in every experimental video. Furthermore, the wide range of F1-scores might be explained by changes in light exposure and contaminants on the capillary throughout different experiments, which result in more false negatives during crystal detection and, consequently, a lower F1-score.

Table SIII.: The table contains the results obtained from deep learning algorithm for all the experimental combinations under 1.1 supersaturation. Output quality of the classifier was shown by confusion matrix numbers along with their F1-scores.

Super-saturation	Wavelength (nm)	Laser intensity (MW/cm2)	Number of Droplets	Droplets with crystal : Manual counting	Droplets with crystal : Automatic counting	TP	TN	FP	FN	Alpha	F1-score
1.1	blank	0	1631	32	32	32	1599	0	0	0.14	100
1.1	1064	10	1505	60	43	43	1444	1	17	0.15	82.69
1.1	1064	25	1483	79	73	73	1396	8	6	0.4	91.25
1.1	1064	50	1034	55	50	50	977	2	5	0.35	93.45
1.1	1064	100	1610	93	83	83	1517	0	10	0.3	94.31
1.1	532	10	1001*	51	-	-	-	-	-	-	-
1.1	532	25	1057	76	68	68	976	3	8	0.16	92.51
1.1	532	50	1979	138	138	138	1841	0	0	0.15	100
1.1	532	100	1229*	115	-	-	-	-	-	-	-
1.1	355	10	1478	53	53	53	1424	1	0	0.4	99.06
1.1	355	25	1571*	73	-	-	-	-	-	-	-
1.1	355	50	1046	109	99	99	928	10	10	0.07	90.82
1.1	355	70	1187	219	190	190	934	34	29	0.1	85.78

Fullform: TP = True Positives, TN = True Negatives, FP = False Positives, FN = False Negatives, Alpha : (frames in which crystal is seen/ frames in which droplet is seen), F1-score = (2 * Precision * recall)/(Precision + recall). The quality of three experimental videos with * sign was not adequate to accurately extract data for the automatic crystal count numbers in the confusion matrix table.

B

B.6. DLS RESULTS

In the main article, Dynamic Light Scattering (DLS) results were presented for unfiltered KCl solution and filtered KCl solutions using various pore size filters (0.2 μm, 0.45 μm, 7 μm). The DLS measurements were performed at 25°C using a Malvern Panalytical Zetasizer Pro apparatus, with a 633 nm laser light source and a scattering angle of 13°. In this section, we provide a repetition of these results along with additional data for the doped solution containing Fe_3O_4 nanoparticles. Notably, the DLS count rate for filtered samples with 0.22-micron and 0.45-micron filters was quite low (≤100 kcps), potentially indicating data inconsistencies. In contrast, the count rate was reliably higher (≥100 kcps) for the 7-micron filtered samples (118.3 kcps), as well as for unfiltered (127.5 kcps) and doped samples (159.2 kcps), suggesting more accurate measurements.

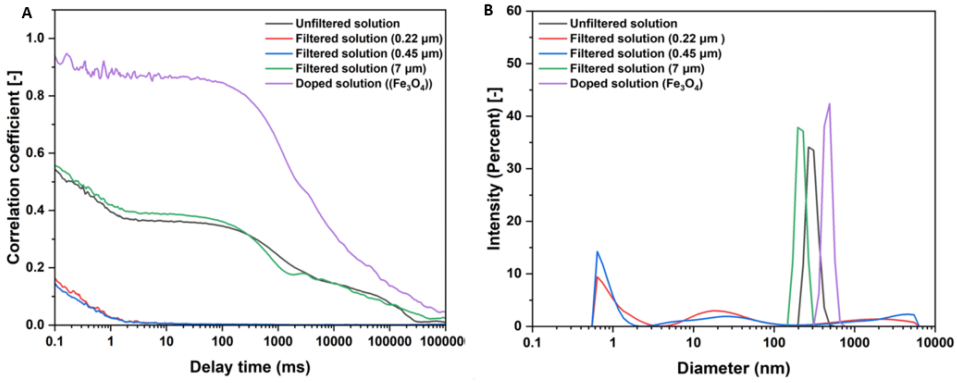

Figure SIV.: (A) Cross correlation functions obtained via DLS and (B) Particle size distribution determined by fitting DLS data for unfiltered KCl solution, KCl solution filtered with 0.22 μm, 0.45 μm, and 7 μm filters, as well as the solution doped with Fe_3O_4 nanoparticles.

C

APPENDIX C

c.1. PEGYLATION OF AUNPS

The 50 nm AuNPs were pelleted by centrifuging at 8000 min^{-1} for 30 minutes and redispersed in MilliQ water. To the 15 mL of 50 nm AuNP water dispersion, 63 µL of 100 mg mL^{-1} PEG5000-SH was added and vigorously stirred for 18 hours at room temperature. The expected PEG density was set to be 10 PEGs/nm^2. The PEG-coated AuNPs, following preparation, were washed three times with MilliQ water and subsequently redispersed in 15 mL of the same water.

c.2. COMPARATIVE ANALYSIS OF NANOPARTICLE ABSORPTION EFFICIENCIES AT 532 NM USING MIE THEORY

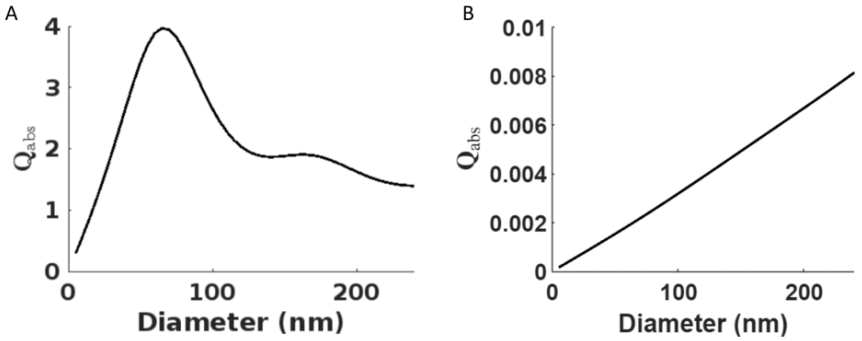

Figure SI.: (A) Absorption efficiency vs Diameter (nm) of gold nanoparticles at 532 nm using Mie theory. The value for the complex refractive index is 0.54386 + i2.2309, (B) Absorption efficiency vs Diameter (nm) of silica nanoparticles at 532 nm using Mie theory. The value for the complex refractive index is 1.4668 + i0.0019918

In this section, we present a comparative analysis of the absorption efficiencies of gold and silica nanoparticles at a wavelength of 532 nm, calculated using Mie Theory. The following figures depict how absorption efficiency varies with particle diameter, alongside the complex refractive indices specific to each nanoparticle type at this wavelength.

C

C.3. ELLIPTICAL BEAM RADIUS ACROSS THE VIAL

In this section, the variation of the elliptical radius $R_{\text{ellipse}}(x)$ is given as a function of position x along the vial.

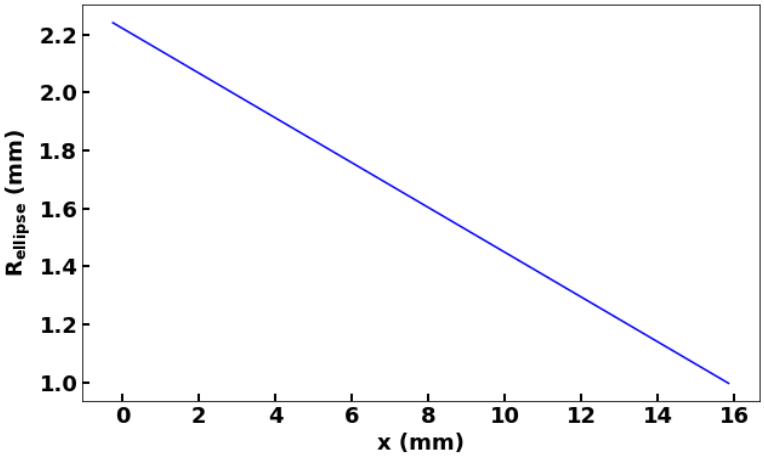

Figure SII.: The function $R_{\text{ellipse}}(x)$ showing how the radius of the ellipse varies with x along the diameter of the vial.

C.4. CONTROL EXPERIMENTS DATA ACROSS DIFFERENT CONCENTRATIONS OF AUNPS

Figure SIII illustrates the nucleation probabilities for supersaturated filtered urea solutions doped with 50 nm gold nanoparticles (AuNPs) across a range of concentrations, measured during control experiments. The nucleation probabilities observed in Figure SIII are comparable, as indicated by the overlapping error bars.

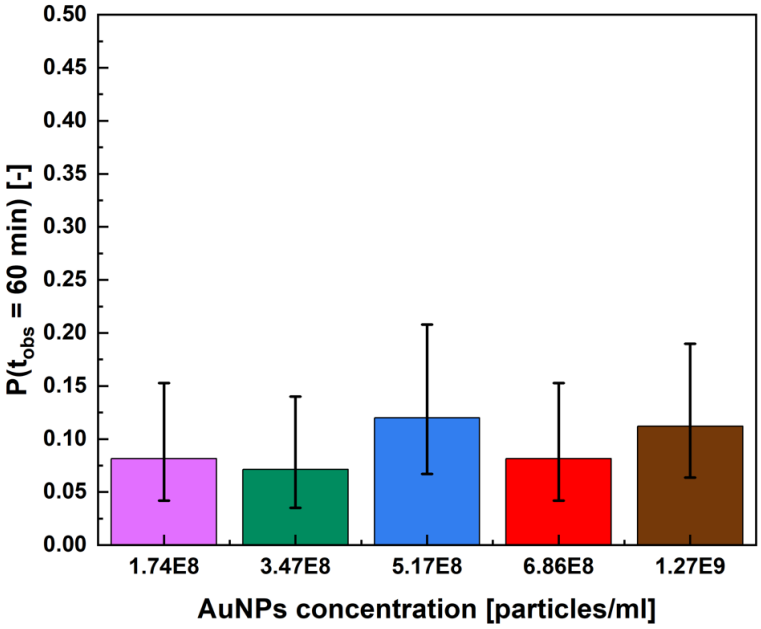

Figure SIII.: Nucleation probabilities of filtered urea solutions containing 50 nm AuNPs with different nanoparticle concentrations under S = 1.5 in control experiments. Error bars are computed using the Wilson's score method.

C.5. NUMBER OF NANOPARTICLES IN AN ELLIPTICAL FRUSTUM

To calculate the volume of an elliptical frustum, equation C.1 is used. The volume of the frustum is determined at the path length where the intensity is significantly attenuated due to nanoparticle absorption. With the known volume of this frustum and the nanoparticle concentration, the number of nanoparticles present within the frustum can be calculated. The results are presented in Table SI.

$$V = \pi L \frac{R_1^2 + R_1 R_2}{2} \tag{C.1}$$

where V is the volume of the elliptical frustum, L is the path length of the frustum from our calculations of Table 4.3, R_1 is the radius of incident laser beam, R_2 is the radius of the elliptical beam, calculated at the corresponding path lengths for each AuNPs concentration at a fixed laser peak intensity of 376 MW/cm^2 using the graph provided in section C.3.

In the Table SII, R_2 is the radius of the elliptical beam, calculated at the corresponding path lengths for each laser peak intensity at a fixed

Table SI.: Summary of AuNP Concentrations, Corresponding Path Lengths, and Number of Nanoparticles Present in an Elliptical Frustum at a fixed Laser Peak Intensity of 376 MW/cm^2

Concentration of AuNPs (particles/ml)	**Path length (l) (mm)**	**Radius of First Disk (mm)**	**Radius of Second Disk (mm)**	**Volume of elliptical fructum (mm^3)**	**Number of AuNPs**
1.74×10^8	0.115	2.25	2.231	1.82	3.16×10^5
3.47×10^8	0.058	2.25	2.236	0.91	3.19×10^5
5.17×10^8	0.039	2.25	2.237	0.61	3.19×10^5
6.86×10^8	0.030	2.25	2.238	0.47	3.26×10^5
1.27×10^9	0.016	2.25	2.239	0.25	3.22×10^5

AuNPs concentration of 6.86×10^8 particles/ml using the graph provided in section C.3.

Table SII.: Summary of laser peak intensities, Corresponding Path Lengths, and Number of Nanoparticles Present in an Elliptical Frustum at a fixed AuNPs concentration of 6.86×10^8 particles/ml

Laser peak intensity (MW/cm^2)	**Path length (l) (mm)**	**Radius of First Disk (mm)**	**Radius of Second Disk (mm)**	**Volume of elliptical fructum (mm^3)**	**Number of AuNPs**
10	0.021	2.25	2.2388	0.33	2.28×10^5
50	0.025	2.25	2.2385	0.39	2.72×10^5
100	0.026	2.25	2.2384	0.41	2.82×10^5
200	0.028	2.25	2.2383	0.44	3.04×10^5
376	0.030	2.25	2.2381	0.47	3.26×10^5

c.6. LASER INTENSITY & ENERGY ABSORPTION PROFILES

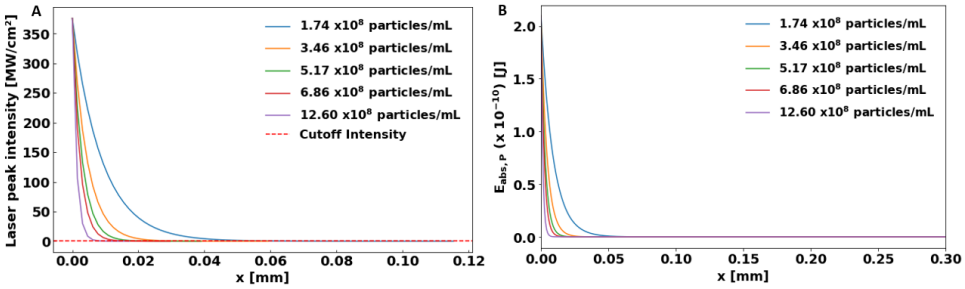

Figure SIV.: (A) Laser peak intensity profile along the diameter of the vial, highlighting the effects of geometrical focusing and nanoparticle absorption for a fixed AuNPs concentration (6.8×10^8 particles/ml). (B) Corresponding energy absorption per nanoparticle across the diameter of the vial at varying laser peak intensities for a fixed AuNPs concentration (6.8×10^8 particles/ml).

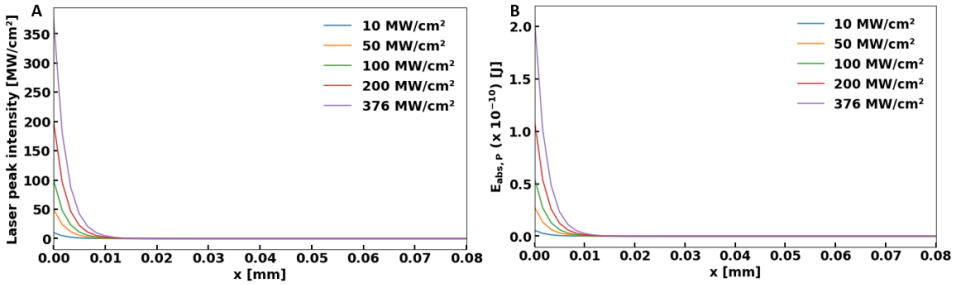

Figure SV.: (A) Laser peak intensity profile along the diameter of the vial, highlighting the effects of geometrical focusing and nanoparticle absorption for different AuNPs concentration at a fixed laser intensity (376 MW/cm^2), (B) Corresponding energy absorption per nanoparticle across the diameter of the vial for different AuNPs concentration at a fixed laser intensity (376 MW/cm^2).

c.7. CRITICAL LASER THRESHOLD OF SILICA NANOPARTICLES

The following equation calculates the theoretical laser intensity threshold at which the temperature of the nanoparticle surpasses the boiling point of the surrounding liquid. This temperature increase prompts the

formation of a vapor layer on the nanoparticle surface, leading to a rapid pressure rise and the subsequent creation of a cavitation bubble[6]:

$$(I_o)_{\text{theo}} = \frac{4\pi R_{\text{np}} c_l \rho_l \nu_l T_{\text{boil}}}{r_{\text{abs}}} \tag{C.2}$$

Here, $(I_o)_{\text{theo}}$ denotes the theoretical laser intensity threshold. $R_{\text{np}} = 25 \times 10^{-9}$ m represents the radius of the nanoparticle, $c_l = 2815.0$ J/(kg·K) is the specific heat of the urea solution, $\rho_l = 1166.0$ kg/m^3 is the solution's density, $T_{\text{boil}} = 647.0$ K is the boiling temperature, $r_{\text{abs}} = 2.94 \times 10^{-18}$ m^2 is the absorption cross section, $\tau_L = 7 \times 10^{-9}$ s is the pulse duration, and $\gamma_l = 1.83 \times 10^{-7}$ m^2/s is the thermal diffusivity of the urea solution.

The calculated theoretical laser intensity threshold of 4152.74 MW/cm^2 assumes that only one nanoparticle in the solution is irradiated by the laser[6, 7]. However, the laser intensity applied in our experiments was 376 MW/cm^2, substantially lower than this theoretical threshold. Therefore, under our experimental conditions, no bubble formation is expected when laser heats the silica nanoparticles doped in urea solutions, leading to much lower nucleation probabilities compared to gold-doped urea solutions.

BIBLIOGRAPHY

[1] A. J. Alexander and P. J. Camp. “Non-photochemical laser-induced nucleation”. In: *The Journal of chemical physics* 150.4 (2019), p. 040901. issn: 0021-9606. doi: 10.1063/1.5079328.

[2] A. J. Alexander and P. J. Camp. “Single Pulse, Single Crystal Laser-Induced Nucleation of Potassium Chloride”. In: *Crystal Growth & Design* 9.2 (2009), pp. 958–963. doi: https://doi.org/10.1021/cg8007415.

[3] M. R. Ward and A. J. Alexander. “Nonphotochemical laser-induced nucleation of potassium halides: Effects of wavelength and temperature”. In: *Crystal Growth and Design* 12.9 (2012), pp. 4554–4561. issn: 15287483. doi: 10.1021/cg300750c.

[4] [Online; accessed 03-05-2022]. url: https://refractiveindex.info/?shelf=glass$%5C&$book=SCHOTT-BK$%5C&$page=N-BK7.

[5] C. Tan and Y. Huang. “Dependence of refractive index on concentration and temperature in electrolyte solution, polar solution, nonpolar solution, and protein solution”. In: *Journal of Chemical & Engineering Data* 60.10 (2015), pp. 2827–2833. issn: 0021-9568.

[6] E.-A. Brujan. “Numerical investigation on the dynamics of cavitation nanobubbles”. In: *Microfluidics and Nanofluidics* 11.5 (May 2011), pp. 511–517. issn: 1613-4990. doi: 10.1007/s10404-011-0816-3.

[7] S. Egerev, S. Ermilov, O. Ovchinnikov, A. Fokin, D. Guzatov, V. Klimov, A. Kanavin, and A. Oraevsky. “Acoustic signals generated by laser-irradiated metal nanoparticles”. In: *Applied Optics* 48.7 (Nov. 2008), p. C38. issn: 1539-4522. doi: 10.1364/ao.48.000c38.

ACKNOWLEDGEMENTS

This 4.5-year PhD journey would not have been possible without the unwavering support, encouragement, and guidance of many incredible individuals.

First and foremost, I extend my deepest gratitude to my supervisor, Dr. Burak Eral, for believing in me and providing the opportunity to pursue my PhD within your group. Your passion for conducting high-quality science has not only helped me develop new skills essential for this project but also contributed significantly to my personal growth. The most valuable lesson I have learned from you is the importance of asking the right questions. The freedom you granted me to explore various directions in my research has allowed me to delve into multidisciplinary topics, greatly enhancing my abilities as an independent researcher. Your patience, positive attitude, and optimism were constant sources of confidence during the most challenging times.

I am also deeply grateful to my promotor, Prof. Dr. Ir. Johan Padding, for your expert advice and the stimulating brainstorming sessions that enriched numerous projects throughout my PhD. Your support has consistently added new dimensions to my research.

I owe much of my research success to the critical insights and valuable suggestions from Prof. Dr. Ir. Herman Kramer and Prof. Dr. Ir. Antoine van den Heijden. Your expertise and thoughtful guidance have been instrumental in navigating the complex pathways of my research.

Special thanks to Fred, who supported me at every step of my PhD. Your hands-on assistance and willingness to help made a significant difference in all my projects. From strategic guidance to experimental execution, your contributions have been pivotal. Additionally, your meticulous attention to detail in reviewing and refining my articles has greatly enhanced their quality during the publication process.

I am particularly grateful to my colleague, Nagaraj, who worked alongside me on the same project. Our partnership throughout this PhD journey has been both enjoyable and immensely productive. Thank you for the brainstorming sessions and for sharing both the struggles and successes of this journey.

Thanks to Daniel and Jenkins for your guidance in operating the laser and assisting with the initial set of experiments. Daniel, your expertise in optics and your support during the early stages of the project significantly accelerated our progress.

Thanks to Michel van den Brink and Jaap van Raamt for their continuous technical support across various projects. Additionally, my appre-

ciation goes to the staff members of the PE department: Leslie, Linda, Caroline, Eveline, and Rob, for your invaluable administrative support whenever needed.

I would like to extend my sincere appreciation to all the master's students who contributed to various phases of my research. Lotte, Vincent, Thomas, and Gutta, your work on the microfluidic NPLIN project was integral to its success. Lotte, your systematic planning, effective problem-solving, and success in making the sensors work helped us build the first prototype of our setup. Vincent, your meticulous approach to experiments and attention to detail were crucial in achieving the results that supported our publication. Thomas, your punctuality and persistence were commendable, and Gutta, despite your brief involvement, your eagerness to learn and conduct good experiments was evident, even as you transitioned from a simulation background. Mias, your commitment to the laser-exposed volume project, including commuting daily from Arnhem for experiments and critically evaluating your results, was truly commendable and led to a publication. Dimitri, your work on utilizing tattoo removal lasers for NPLIN studies demonstrated the potential for conducting research with significantly lower-cost equipment. Your independent thinking greatly contributed to the project's success. Lale, Riemer, and Tim, your continuation of my master's thesis work on microfluidic antisolvent crystallization was invaluable. Lale, your experimental efforts significantly advanced our exploration of microfluidic antisolvent crystallization. Riemer, your meticulous planning and perseverance provided new directions for this research. Tim, your proactive approach and independent thinking played a vital role in shaping this work and bringing it closer to publication. PingPing, your dedication and perseverance in conducting experiments for the laser-exposed nanoparticles project were crucial to our success. Your attention to detail significantly contributed to bringing us closer to publication. I also appreciate Pepijn for his assistance with the fitting procedures in the project.

Thanks to the committee members who took the time to evaluate my dissertation.

Thanks to my cricket team at DSV Concordia. Playing with you all for the past seven years has been a great source of joy and relaxation, and it has allowed me to build strong friendships both on and off the field. Thank you for the fun times and stress relief breaks that helped me maintain my sanity.

To all my colleagues, past and present, in the research group at the P&E department, I extend my gratitude. Thank you for your camaraderie and support.

My friends from the Rookies group in the Netherlands—Nandalal, Srushti, Praveen, Ashwin, Pranav, Akash, Priyanshi, and Narayani—have been with me from my master's studies through to my PhD and beyond. You have been more than just friends; you have been my family away from

home, offering constant support, encouragement, and laughter through the ups and downs of academic life.

To my parents and brother, who instilled in me the values of hard work and perseverance, and to my in-laws, who have provided great emotional support, I thank you. Your unconditional love and encouragement have been the pillars of my strength.

To my beloved wife, Harshitha, you have been my rock throughout this journey. Your love, patience, and unwavering support have kept me grounded and motivated. I am incredibly grateful for your sacrifices and for standing by me through the highs and lows of this PhD journey.

CURRICULUM VITæ

Vikram Bharadwaj Korede was born on 19th September 1994 in Hyderabad, India. He completed his B.Tech in Chemical Engineering with First Class honors from the National Institute of Technology in Tiruchirappalli, India, in 2016. During his undergraduate studies, Vikram developed a strong interest in process engineering, which motivated him to pursue an M.Sc. in Chemical Engineering at Delft University of Technology in the Netherlands.

In 2017, Vikram joined the Crystallization group within Process and Energy department at Delft University of Technology. There, under the guidance of Dr. Burak Eral, he conducted his master's research, focusing on the growth dynamics of aspirin crystals using microfluidic antisolvent crystallization. After obtaining his M.Sc. degree, he continued his PhD journey within the same group on the topic Taming Crystallization with Light. His research investigates the mechanism behind Non-Photochemical Laser Induced Nucleation (NPLIN), aiming to understand laser interaction with supersaturated solutions. By integrating his expertise in chemical engineering with advanced crystallization techniques, Vikram aims to make significant contributions to the field, enhancing the understanding and application of laser-induced crystallization processes.

LIST OF PUBLICATIONS

JOURNAL PUBLICATIONS INCLUDED IN THIS THESIS

1. Vikram Korede, Nagaraj Nagalingam, Frederico Marques Penha, Noah van der Linden, Johan T. Padding, Remco Hartkamp, and Huseyin Burak Eral, "A Review of Laser-Induced Crystallization from Solution", *Crystal Growth & Design*, 2023, 23(5), 3873-3916, DOI: 10.1021/acs.cgd.2c01526

2. Vikram Korede, Mias Veldhuis, Frederico Marques Penha, Nagaraj Nagalingam, PingPing Cui, Antoine E.D.M. Van der Heijden, Herman J.M. Kramer, and Hüseyin Burak Eral, "Effect of Laser-Exposed Volume and Irradiation Position on Nonphotochemical Laser-Induced Nucleation of Potassium Chloride Solutions", *Crystal Growth & Design*, 2023, 23(11), 8163-8172, DOI: 10.1021/acs.cgd.3c00865.

3. Vikram Korede, Frederico Marques Penha, Vincent de Munck, Lotte Stam, Thomas Dubbelman, Nagaraj Nagalingam, Maheswari Gutta, PingPing Cui, Daniel Irimia, Antoine E.D.M. van der Heijden, Herman J.M. Kramer, and Hüseyin Burak Eral, "Design and Validation of a Droplet-based Microfluidic System To Study Non-Photochemical Laser-Induced Nucleation of Potassium Chloride Solutions", *Crystal Growth & Design*, 2023, 23 (8), 6067-6080, DOI: 10.1021/acs.cgd.3c00591.

4. Pingping Cui, Vikram Korede, Pepijn van Tooren, Nagaraj Nagalingam, Runze Wang, Qiuxiang Yin, Antoine E.D.M. van der Heijden, Herman J.M. Kramer, and Hüseyin Burak Eral, "Influence of Nanoparticle Properties on Non-Photochemical Laser-Induced Nucleation", (Submitted).

JOURNAL PUBLICATIONS NOT INCLUDED IN THIS THESIS

1. Nagaraj Nagalingam, Aswin Raghunathan, Vikram Korede, Christian Poelma, Carlas S. Smith, Remco Hartkamp, Johan T. Padding, and Hüseyin Burak Eral, "Laser-Induced Cavitation for Controlling Crystallization from Solution", *Physical Review Letters*, 131, 124001, DOI: 10.1103/PhysRevLett.131.124001.

2. Nagaraj Nagalingam, Aswin Raghunathan, Vikram Korede, Edwin F.J. Overmars, Shih-Te Hung, Remco Hartkamp, Johan T. Padding,

Carlas S. Smith, Huseyin Burak Eral, "Low-cost fluorescence microscope with microfluidic device fabrication for optofluidic applications", *HardwareX*, ISSN: 2468-0672, Vol: 14, Page: e00415, Published: April 08, 2023, DOI: 10.1016/j.ohx.2023.e00415.

3. Nagaraj Nagalingam, Vikram Korede, Daniel Irimia, Jerry Westerweel, Remco Hartkamp, Johan T. Padding, Huseyin Burak Eral, "Unified Framework for Laser-induced Transient Bubble Dynamics within Microchannels," *Scientific Reports*, vol. 14, article no. 14291, 2024. DOI: 10.1038/s41598-024-68971-x.

4. Nagaraj Nagalingam, Adithya Vignesh, Vikram Korede, Herman J.M. Kramer, Antoine E.D.M. van der Heijden, Remco Hartkamp, Johan T. Padding, Carlas S. Smith, Huseyin Burak Eral, "Microjet assisted crystallization from solution via laser-induced bubble pairs in a microcapillary", (to be submitted)

5. Nagaraj Nagalingam, Jan Groenewold, Vikram Korede, Pingping Cui, Herman J.M. Kramer, Antoine E.D.M. van der Heijden, Johan T. Padding, Remco Hartkamp, Huseyin Burak Eral, "General Framework for Non-photochemical Laser-Induced Crystallization via Cavitation", (to be submitted)

CONFERENCE PROCEEDINGS & ORAL PRESENTATIONS

1. Vikram Korede, Frederico Marques Penha, Vincent de Munck, Lotte Stam, Thomas Dubbelman, Nagaraj Nagalingam, Maheswari Gutta, PingPing Cui, Daniel Irimia, Antoine E.D.M. van der Heijden, Herman J.M. Kramer, and Hüseyin Burak Eral, "Design and Validation of a Droplet-based Microfluidic System To Study Non-Photochemical Laser-Induced Nucleation of Potassium Chloride Solutions", Proceedings of the 21st annual meeting of the American Institute for Chemical Engineers, Boston, AIChE (2021).

2. Vikram Korede, Mias Veldhuis, Frederico Marques Penha, Nagaraj Nagalingam, PingPing Cui, Antoine E.D.M. Van der Heijden, Herman J.M. Kramer, and Hüseyin Burak Eral, "Effect of Laser-Exposed Volume and Irradiation Position on Nonphotochemical Laser-Induced Nucleation of Potassium Chloride Solutions", 7th European Conference on Crystal Growth, Paris, ECCG7 (2022).

3. Vikram Korede, Mias Veldhuis, Frederico Marques Penha, Nagaraj Nagalingam, PingPing Cui, Antoine E.D.M. Van der Heijden, Herman J.M. Kramer, and Hüseyin Burak Eral, "Effect of Laser-Exposed Volume and Irradiation Position on Nonphotochemical Laser-Induced Nucleation of Potassium Chloride Solutions", 50th Dutch Association of Crystal Growth, Amsterdam, DACG50 (2023).

4. Tim Scholts, Vikram Korede, Riemer van Nes, Lale Nur Yildiz, Sevgi Polat, Frederico Marques Penha, Johan T. Padding, and Hüseyin Burak Eral, "Growth Dynamics of Aspirin Crystals in Microfluidic Antisolvent Crystallization", 50th Dutch Association of Crystal Growth, Veldhoven, NWO Physics (2023).

5. Tim Scholts, Vikram Korede, Riemer van Nes, Lale Nur Yildiz, Sevgi Polat, Frederico Marques Penha, Johan T. Padding, and Hüseyin Burak Eral, "Growth Dynamics of Aspirin Crystals in Microfluidic Antisolvent Crystallization", Enschede, NPS18 (2023).

POSTER PRESENTATIONS

1. Vikram Korede, Frederico Marques Penha, Vincent de Munck, Lotte Stam, Thomas Dubbelman, Nagaraj Nagalingam, Maheswari Gutta, PingPing Cui, Daniel Irimia, Antoine E.D.M. van der Heijden, Herman J.M. Kramer, and Hüseyin Burak Eral, "Design and Validation of a Droplet-based Microfluidic System To Study Non-Photochemical Laser-Induced Nucleation of Potassium Chloride Solutions", International Symposium on Industrial Crystallization, Berlin, ISIC21 (2021).

2. Vikram Korede, Frederico Marques Penha, Vincent de Munck, Lotte Stam, Thomas Dubbelman, Nagaraj Nagalingam, Maheswari Gutta, PingPing Cui, Daniel Irimia, Antoine E.D.M. van der Heijden, Herman J.M. Kramer, and Hüseyin Burak Eral, "Design and Validation of a Droplet-based Microfluidic System To Study Non-Photochemical Laser-Induced Nucleation of Potassium Chloride Solutions", Delft, NPS17 (2022)

3. Vikram Korede, Mias Veldhuis, Frederico Marques Penha, Nagaraj Nagalingam, PingPing Cui, Antoine E.D.M. Van der Heijden, Herman J.M. Kramer, and Hüseyin Burak Eral, "Effect of Laser-Exposed Volume and Irradiation Position on Nonphotochemical Laser-Induced Nucleation of Potassium Chloride Solutions", International Symposium on Industrial Crystallization, Glasgow, ISIC22 (2023).

4. Tim Scholts, Vikram Korede, Riemer van Nes, Lale Nur Yildiz, Sevgi Polat, Frederico Marques Penha, Johan T. Padding, and Hüseyin Burak Eral, "Growth Dynamics of Aspirin Crystals in Microfluidic Antisolvent Crystallization", International Symposium on Industrial Crystallization, Glasgow, ISIC22 (2023).